Microscopic understanding of the Antisite disorder on magnetic and transport properties in Heusler alloys

A Thesis submitted in partial fulfillment for the Degree of

DOCTOR OF PHILOSOPHY

in the School of Physical and Applied Sciences
Goa University

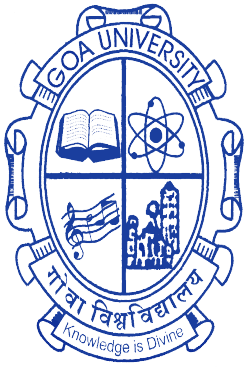

By

Samiksha V. Malik
School of Physical and Applied Sciences
Goa University
Goa

June 2023

DECLARATION

I, Samiksha V. Malik hereby declare that this thesis represents work which has been carried out by me and that it has not been submitted, either in part or full, to any other University or Institution for the award of any research degree.

Place: Taleigao Plateau.
Date : June, 2023 Samiksha V. Malik

CERTIFICATE

I hereby certify that the work was carried out under my supervision and may be placed for evaluation.

Prof. K. R. Priolkar
School of Physical and Applied Sciences

Acknowledgment

First of all, I would like to express my deep sense of gratitude toward my research guide Prof. K. R. Priolkar for all his teachings, unwavering support, and moral upliftment during the course of my Ph.D. work. His elevated perspectives, passion for research, and subtle understanding of the subject have inspired me time and again. I am truly blessed that I got the opportunity to work under his guidance.

I am very much thankful to Prof. A. K. Nigam (TIFR, Mumbai), Dr. V. Srihari (BARC, Mumbai), Dr. P. D. Babu (UGC-DAE Consortium for Scientific Research, Mumbai), Dr. Amitabh Das (BARC, Trombay), and Dr. E. T. Dias (Goa University) for their experimental cooperation during this research work.

For experimental assistance at XAFS beamlines, I sincerely thank Dr. Edmund Welter and Dr. Ruidy Nemausat at P65, PETRA III Synchrotron source, DESY - Hamburg. I am grateful to Dr. Gangadhar Das for his cooperation in conducting experiments at the Indian beamline, Photon factory, KEK.

I am very thankful to the Science and Engineering Research Board (SERB) for the financial assistance under project EMR/2017/001437. The financial support from the Department of Science and Technology, Govt. of India, for travel under DST-DESY, Indo-Japan collaborations is greatly appreciated.

I express my sincere gratitude to Goa University for allowing me to conduct my research work. The entire teaching staff of the School of Physical and Applied Sciences, especially the members of the DRC, Dr. Sudhir Cherukulappurath and Dr. Bholanath Pahari are thanked for their guidance and valuable advice. A warm thanks to all the non-teaching staff for their constant cooperation during the time of this research work.

I am beyond grateful to all the fellow research scholars from the School of Physical and Applied Sciences for the motivation, helpful suggestions, worthwhile time, and positive environment.

My heartfelt gratitude to my friends and family for their moral support and constant encouragement.

A special mention, I extend my heartfelt regards to my Uncle Late. Gurudas G. Malik.

Dedicated to
My lovely Parents and Sister

Contents

1 Introduction **1**

1.1 Heusler Structure and bonding characteristics 2

1.2 Antisite disorder and its implications 3

1.2.1 Antisite disorder 3

1.2.2 Types of antisite disorders 4

1.2.3 Driving factors behind disorders and defects 5

1.2.4 Effect of antisite disorder on Heusler alloys. 8

1.3 Magnetism in Heusler alloys 10

1.4 Martensitic transformation 11

1.4.1 Martensitic transformation temperature and e/a ratio. 13

1.5 Mn_2YZ systems 16

1.5.1 Crystal structure and magnetism of Mn_2YZ alloys. 18

1.6 Objectives: 19

2 Experimental Techniques **31**

2.1 Introduction 31

2.2 Sample preparation 32

2.3 Energy-Dispersive X-ray (EDX) spectroscopy 33

2.4 Structural studies 34

2.4.1 X-ray diffraction (XRD) 34

2.4.2 Neutron diffraction (ND) 36

2.4.3 X-ray Absorption Fine Structure (XAFS) spectroscopy 37

2.5 Magnetization measurements 43

2.5.1 Superconducting Quantum Interference Device (SQUID) magnetometer 43

2.5.2 Vibrating sample magnetometer (VSM) 44

2.6 Transport properties 45

2.6.1 Electrical resistivity 45

2.6.2 Hall resistivity 46

3 Role of antisite disorder in the martensitic transition of $Ni_{2-x}Mn_{1+x}Ga$. 51

3.1 Introduction 51

3.2 Results 55

3.3 Discussion 70

3.4 Conclusions 74

4 Antisite disorder and phase segregation in Mn_2NiSn. 79

4.1 Introduction 79

4.2 Results and Discussion 81

4.3 Conclusion 96

5 Ni induced ferromagnetism in Mn_3Ga. 101

5.1 Introduction 101

5.2 Results 103

5.3 Discussion 113

5.4 Conclusion 115

6 Effect of Ni substitution on the magnetic and electronic ground state of Mn_3Sn. 121

6.1 Introduction 121

6.2 Results 123

6.3 Discussion 142

6.4 Conclusions 146

7 Summary and Future Work 153

7.1 Summary 153

7.2 Future work 156

List of Tables

1.1 Consider reordering as General formula, space groups related to various types of atomic orders in Heusler alloys, and associated antisite disorder. (The notations as per ICSD (Inorganic Crystal Structure Database), SB (Strukturberichte), and Pearson database are given.)[17] 6

2.1 Various heat treatments given to the alloys under investigation. (a) RQ - rapid quenched (b) TA - temper annealed (c) HTA - high temperature (850°C) annealed (d) LTA - low temperature (400°C) annealed (e) * two halves of the same alloy ingots were subjected separately (i) rapid quenching (RQ) and (ii) temper annealing (TA). (f) # the alloy ingots were initially subjected to high-temperature annealing and subsequently to low-temperature annealing. 33

3.1 e/a ratio calculated from the nominal composition, EDX composition, lattice parameter, a estimated from Rietveld refinement of the XRD patterns (errors in the last digit are given in parenthesis), and the martensitic start temperature, T_M for $Ni_{2-x}Mn_{1+x}Ga$ series 58

3.2 Near neighbour bond distances (R) and the mean-square disorder in the bond length (σ^2) obtained by simultaneous fitting of 300 K Ni, Mn, and Ga K-edge EXAFS data for RQ, FC $Ni_{2-x}Mn_{1+x}Ga$ series. Figures in parentheses signify variability in the last digit. 64

3.3 Values of near neighbour bond distances (R) and the mean-square disorder in the bond length (σ^2) obtained from simultaneous by the fitting of 30 K Ni, Mn, and Ga K-edge EXAFS for RQ, FC $Ni_{2-x}Mn_{1+x}Ga$ alloys. Figures in parentheses signify variability in the last digit. 64

3.4 Phase fractions of constituent phases in $Ni_{1.25}Mn_{1.75}Ga$ and $NiMn_2Ga$ RQ and FC alloys. The shortfall in the sum of phase fractions is made up by MnO impurity phase. 66

4.1 Initial and EDX compositions, lattice parameters determined from Rietveld refinements of the XRD patterns, and T_C determined from the temperature-dependent magnetization measurements of the quenched $Ni_{2-x}Mn_{1+x}Sn$ alloys. 83

4.2 Values of bond distances (R) and mean square disorder in bond distances (σ^2) obtained by simultaneous fitting of Ni, Mn and Sn EXAFS in $Ni_{2-x}Mn_{1+x}Sn$ series of RQ alloys, recorded at 100 K. Figures in parentheses designate uncertainty in the ending digits. 86

4.3 Bond distances (R) and mean square disorder in the bond distance (σ^2) obtained by simultaneous fitting of Ni, Mn and Sn EXAFS recorded at 100 K in $Ni_{2+x}Mn_{1-x}Sn$ (x = 0.75, 1) TA alloys. Figures in parentheses designate uncertainty in the ending digits. 95

5.1 The estimated inter-planar distance 'd' and the lattice parameter 'a' for Mn_3Ga and $Ni_{0.25}Mn_{2.75}Ga$ alloys. 104

5.2 Estimated bond distances (R) and thermal mean square distortion in bond distances (σ^2) values deduced from the concurrent fitting of Mn and Ga K edge EXAFS for HTA Mn_3Ga and $Ni_{0.25}Mn_{2.75}Ga$ alloys recorded at 100 K. Numbers in parentheses delegate the uncertainty in the end digits of the tabulated values. 108

5.3 Obtained value of bond distances (R) and mean square disorder in bond distances (σ^2) for Ni edge EXAFS data fitting at 100 K. Figures in parentheses designate uncertainty in the ending digits. 110

6.1 Bond length (R) and mean square distortion in bond lengths (σ^2) obtained from Mn edge EXAFS fitting of $Mn_{3-x}Ni_xSn$ x = 0 and 0.25 alloys, recorded at 100 K and 300 K. Figures specified in the parenthesis denote the uncertainty in the ending digit. Here C.N. refers to the coordination number. . . 140

6.2 Bond length (R) and mean square distortion in bond lengths (σ^2) obtained from Ni edge EXAFS fitting of $Ni_{0.25}Mn_{2.75}Sn$ alloy, recorded at 100 K. Figures specified in the square brackets denote the uncertainty in the ending digit. 141

List of Figures

1.1 (a) $L2_1$ Heusler structure (b) Z sub-lattice (c) Rock salt sub-lattice (d) Zinc blende sub-lattice of Heusler alloys. 2

1.2 Structural transformation from ordered $L2_1$ Heusler structure to B2, DO_3, and A2 type structures respectively resulting from the intermixing of Y-Z, X-Y, and X-Y-Z atoms. 5

1.3 Schematic illustration of (a) growing martensitic phase within an austenitic parent phase, (b) transformation of crystal structure, accommodation of strain through (c) slipping, (d) twinning. 13

1.4 The correlation between the $L2_1$ cubic austenite and $L1_0$ tetragonal martensite structure. (a) austenite $L2_1$ structure. (b) The tetragonal martensite structure. (c) The top view of the tetragonal martensite structure. (d) and (e) The generated modulated structures for 5M and 7M phases respectively 14

1.5 (a), (b), and (c) represents the structural and the magnetic phase diagram for the Heusler alloys of the type Ni-Mn-Z with Z respectively as Sn, In, and Ga. The open circles and solid triangles correspond to the martensitic and magnetic transformation temperatures. Besides, solid small circles in (c) represent the premartensitic transformation temperatures. The phase diagram is divided into different regions using dotted lines corresponding to various crystal structures. The compositions of the alloy in terms of at.% is specified on the upper axis. T_C^A and T_C^M respectively represent the ferromagnetic magnetic ordering temperatures in austenitic and martensitic states. M_s represents the martensitic start temperature. For all the three-phase diagrams, with increasing e/a ratio the ground-state crystal structure advances from cubic to 10 M to 14 M and then to $L1_0$. 15

1.6 The composition dependence of martensitic transformation temperature (T_M) and magnetic ordering temperature (T_C) for $Mn_{25+x}Ni_{50-x}Ga_{25}$ alloys with $x = 0$, 5, 10, 12.5, 15, 20, 25. 16

1.7 The structural transformation via lattice distortion from an $L2_1$ to the hexagonal structure (a) and the tetragonal structure (c). 18

2.1 Pictures taken during the preparation of the alloy. (a) arc melting furnace, (b) arc melted alloy ingot (c) sliced ingot bead into smaller pieces (d) sample encapsulated quartz tube sealed under vacuum (e) sealed quartz tubes arranged inside the furnace. 32

2.2 Conceptual illustration of Bragg's diffraction. 35

2.3 (a)Schematic representation of an XAFS spectrum, exhibiting absorption of the x-rays both within the 50 eV of the edge energy (XANES) and from some hundred to greater than 1000 eV energy beyond the absorption edge (EXAFS).(b) X-ray absorption cross-section $\frac{\mu}{\rho}$ for various elements in the range from 1 to 100 keV. 38

2.4 (a) The photoelectric effect wherein the x-rays are absorbed and a core-shell electron is excited out from the atom. (b) The interaction between the photoelectron spherical waves traveling away from the absorber atom and the backscattered spherical waves at the absorber atom. 38

2.5 The schematic of the XAFS experimental set-up for transmission and fluorescence geometries. 40

2.6 (a) Schematic illustration of a DC SQUID sensor, (b) schematic representation of Superconducting Quantum Interference Device (SQUID) magnetometer. 44

2.7 Schematic illustration of the four probe setup used for the resistivity measurement. 45

2.8 (a) The representation of the four-wire configuration employed in Hall resistivity measurement. (b) The schematic illustration of the geometry of the Hall experiment. 46

3.1 (a–g) Plots of magnetization as a function of temperature measured in 100 Oe field during ZFC, FCC, and FCW cycles for the RQ and the FC alloys of composition $Ni_{2-x}Mn_{1+x}Ga$. (h) Variation of T_M as a function of x and e/a ratio in $Ni_{2-x}Mn_{1+x}Ga$. 55

3.2 SEM micrographs for $Ni_{2-x}Mn_{1+x}Ga$ with $x = 0$, 0.75 and 1.0 (RQ series) and $x = 0.75$ and 1.0 (FC series) 59

3.3 XRD patterns of RQ $Ni_{(2-x)}Mn_{(1+x)}Ga$ ($x = 0$, 0.25, 0.5, 0.75 and 1.0) and FC $x = 0.75$ and 1.0 samples recorded at room temperature. The black dots indicate the presence of impurity phases. 60

3.4 Le Bail refined laboratory x-ray diffraction patterns of $Ni_{1.25}Mn_{1.75}Ga$ (a) RQ and (c) FC and $NiMn_2Ga$ (b) RQ and (d) FC alloys. 61

3.5 FT magnitudes of k^3 weighted EXAFS measured at 300 K at the Ni, Mn, and Ga K edges in Ni_2MnGa, $Ni_{1.75}Mn_{1.25}Ga$ and $Ni_{1.5}Mn_{1.5}Ga$ RQ alloys. 62

3.6 The magnitude of Fourier transform of k^3 weighted Ni, Mn and Ga K edge EXAFS recorded at 300 K in RQ and FC alloy compositions, $Ni_{1.25}Mn_{1.75}Ga$ and RQ $NiMn_2Ga$. 63

3.7 k^2 weighted raw EXAFS data recorded at the Ni K edge in $Ni_{2-x}Mn_{1+x}Ga$ ($x = 0$, 0.25, 0.5, 0.75 and 1) RQ and FC alloys. 65

3.8 k^2 weighted raw EXAFS data recorded at the Mn K edge in $Ni_{2-x}Mn_{1+x}Ga$ ($x = 0$, 0.25, 0.5, 0.75 and 1) RQ and FC alloys. 66

3.9 k^2 weighted raw EXAFS data recorded at the Ga K edge in $Ni_{2-x}Mn_{1+x}Ga$ (x = 0, 0.25, 0.5, 0.75 and 1) RQ and FC alloys. 67

3.10 Synchrotron x-ray diffraction patterns of $Ni_{2-x}Mn_{1+x}Ga$, x = 0, 0.25 and 0.5 RQ alloys. 68

3.11 Synchrotron x-ray diffractograms of RQ and FC alloy compositions, $Ni_{1.25}Mn_{1.75}Ga$ and $NiMn_2Ga$. Structural phases identified from Rietveld analysis are indicated by numerals, 1 - $Fm3m$, 2 - $Pm3m$, 3- MnO, 4 - $I4/mmm$, and 5 - $P4/mmm$ 69

3.12 Variation of calculated and observed intensity ratios, $I_{(111)}/I_{(220)}$ and $I_{(200)}/I_{(220)}$ as a function of excess Mn concentration (x). 70

3.13 Two dimensional projections showing X_2YZ, ordered XX'YZ, disordered XX'YZ and the possible segregation of Mn_3Ga type defects due to antisite disorder in XX'YZ. 72

4.1 Rietveld refined room temperature XRD patterns for $Ni_{2-x}Mn_{1+x}Sn$ (x = 0, 0.25, 0.5, 0.75 and 1.0) RQ alloys. 82

4.2 a. Temperature-dependent magnetization curves recorded for Ni_2MnSn in H = 0.01 T during ZFC, FCC, and FCW cycles. b. Isothermal magnetization curves recorded for the $Ni_{2-x}Mn_{1+x}Sn$ (x = 0, 0.25, 0.5, 0.75 and 1.0) RQ series of alloys at T = 3 K in H = $\pm$7T. 84

4.3 Temperature dependent resistivity curves recorded for the $Ni_{2-x}Mn_{1+x}Sn$ RQ series of alloys. 85

4.4 Fourier transform magnitudes of the k^3 weighted EXAFS at the Ni, Mn, and Sn edges along with corresponding best fits in RQ $Ni_{2-x}Mn_{1+x}Sn$ alloys for $x = 0$ (a-c), $x = 0.75$ (d-f) and $x = 1.0$ (g-i) 86

4.5 A comparison of FT magnitudes of EXAFS data at (a) Ni,(b) Mn, and (c) Sn K edges in $Ni_{2-x}Mn_{1+x}Sn$ RQ alloys. 89

4.6 Rietveld refined XRD patterns for (a) $Ni_{1.25}Mn_{1.75}Sn$ and (b) $NiMn_2Sn$ TA alloys 91

4.7 (a) Magnetic isotherms at 3 K in ±7T, (b) Temperature dependent resistivity for $Ni_{1.25}Mn_{1.75}Sn$ and $NiMn_2Sn$ TA alloys. 92

4.8 A comparison of FT magnitude of the Ni, Mn, and Sn EXAFS in RQ and TA $Ni_{1.25}Mn_{1.75}Sn$ and $NiMn_2Sn$ alloys. 93

4.9 FT magnitude of k^3 weighted EXAFS at Ni, Mn, and Sn K edges and the corresponding best fits in $Ni_{2+x}Mn_{1-x}Sn$ ($x = 0.75$, 1) TA alloys. 94

5.1 (a) and (b) XRD patterns for HTA $Mn_{3-x}Ni_xGa$ $x = 0$ and $x = 0.25$ alloys respectively. 104

5.2 (a) Magnetization measurement as a function of temperature for $Mn_{3-x}Ni_xGa$ with $x = 0$ and 0.25 alloys in the applied field of 100 Oe. (b) and (c) Isothermal magnetization measurement for HTA $Mn_{3-x}Ni_xGa$ with $x = 0$ and $x = 0.25$ at T = 5 K in H = ±9T field respectively. 106

5.3 Best fits for Fourier transform magnitudes of k^3 weighted EXAFS at the Mn and Ga K edges in HTA $Mn_{3-x}Ni_xGa$ ($x = 0$ and 0.25). The plots are not corrected for phase shifts introduced by the absorber and the scatterer, and hence the peak appears at a lower R-value in the figure. 108

5.4 Comparison between Fourier transform magnitudes of k^3 weighted Mn and Ni EXAFS for HTA Mn_3Ga and $Ni_{0.25}Mn_{2.75}Ga$. 109

5.5 Best fits for the Fourier transformed magnitudes of k^3 weighted Ni K EXAFS for $Ni_{0.25}Mn_{2.75}Ga$. 110

5.6 XRD patterns for LTA (a) Mn_3Ga and (b) $Ni_{0.25}Mn_{2.75}Ga$. 111

5.7 (a) and (b) Isothermal magnetization for LTA $Mn_{3-x}Ni_xGa$ with $x = 0$ and $x = 0.25$ alloys respectively, at T = 5 K in H = ±7T field. (c) Temperature-dependent magnetization for LTA $Ni_{0.25}Mn_{2.75}Ga$ in H = 100 Oe applied field during ZFC, FCC, and FCW cycles. 112

5.8 (a) Zero field cooled and Field cooled hysteresis loop measured at 300 K in HTA $Ni_{0.25}Mn_{2.75}Ga$. Inset (b) and (c) show exchange bias and open hysteresis loop formed in HTA $Ni_{0.25}Mn_{2.75}Ga$ respectively. 114

6.1 Powder x-ray diffraction profiles for (a) Mn_3Sn ($x = 0$) and (b) $Ni_{0.25}Mn_{2.75}Sn$ ($x = 0.25$) at room temperature. Structural phases recognized from Rietveld refinement analysis are specified by numerals, 1 - Mn_3Sn, 2 - Mn_2Sn. 125

6.2 Magnetic property measurements for Mn_3Sn ($x = 0$) and $Ni_{0.25}Mn_{2.75}Sn$ ($x = 0.25$). (a) and (c) The magnetization measurement as a function of temperature at the applied field of 100 Oe in ZFC, FCC, and FCW modes. (b) and (d) Isothermal magnetization measurement at 300 K and 5 K. . . . 126

6.3 Transport and magneto-transport property measurements for Mn_3Sn ($x = 0$) and $Ni_{0.25}Mn_{2.75}Sn$ ($x = 0.25$). (a) and (c) Temperature-dependent resistivity measurement. (b) and (d) Temperature-dependent Hall resistivity measurement. 128

6.4 Isothermal magnetization and Hall resistivity measurements for Mn_3Sn at 350 K, 325 K, 300 K, 275 K, and 250 K. 130

6.5 Isothermal magnetization and Hall resistivity measurements for $Ni_{0.25}Mn_{2.75}Sn$ at 350 K, 325 K, 300 K, 275 K, and 250 K. 131

6.6 Neutron diffraction patterns recorded at 300 K, 290 K, 280 K, and 270 K for Mn_3Sn across T_t transition. 132

6.7 Magnetic structure of Mn_3Sn obtained from the Rietveld refinement of ND data at 300 K. 133

6.8 Refined neutron diffraction patterns at 220 K and 50 K using non-coplanar helical magnetic structural. 134

6.9 The thermal evolution of magnetic modulation wave vector and the magnetization as a function of temperature for Mn_3Sn. 135

6.10 Refined magnetic superstructure of $Ni_{0.25}Mn_{2.75}Sn$ with ten unit cells at 220 K. 136

6.11 The thermal evolution magnetic modulation wave vector and the magnetization as a function of temperature for $Ni_{0.25}Mn_{2.75}Sn$. 137

6.12 (a) Kagome lattice in xy plane. Here d_1 and d_2 denote the bond lengths of two neighboring triangles. (b) Unit cell of Mn_3Sn. 138

6.13 Best fit and k^3 weighted Fourier transform magnitude for the $\chi(k)$ spectra obtained at Mn K edge for Mn_3Sn and $Ni_{0.25}Mn_{2.75}Sn$. 139

6.14 Best fit and k^3 weighted Fourier transform magnitude for the $\chi(k)$ spectra obtained at Ni K edge for $Ni_{0.25}Mn_{2.75}Sn$. 140

6.15 (a) The powder x-ray diffraction pattern recorded for $Ni_{0.5}Mn_{2.5}Sn$ at room temperature. Structural phases recognized from Rietveld refinement analysis are specified by numerals, 1 - $L2_1$ Heusler, 2 - $D0_{19}$ Hexagonal, 3 - Sn, and 4 - MnO. (b) Temperature-dependent magnetization measurement for $Ni_{0.5}Mn_{2.5}Sn$. Inset shows the field-dependent isothermal magnetization measurement at 5 K. 141

6.16 Temperature dependent normalized resistance 'γ'. Inset shows the plot of $G_{measured}$ - $G_{plateau}$ as a function of 1/T with a linear fit shown by the red dotted line. 145

Chapter 1

Introduction

Heusler alloys are ternary intermetallic compounds with the general formula X_2YZ, where X and Y are commonly transition metals, whereas Z is a main group element. This class of materials was discovered by Friedrich Heusler, in the year 1903.[1] One of the first synthesized Heusler alloys was Cu_2MnAl. The discovery turned out as a total surprise because of its ferromagnetic properties despite consisting of only nonmagnetic elements due to an indirect type of exchange interaction between the Mn atoms. This exchange interaction is known as the Rudermann-Kittel-Kasuya-Yoshida (RKKY) interaction.[2]

To date, this class of materials has extended exceptionally to accommodate more than 2200 members showcasing a broad range of phenomena, like superconductivity (Pd_2YbPb[3]), spin density wave (Mn_3Si[4]), thermoelectricity (Fe_2VAl[5]), topological Weyl semimetals (Mn_3Sn[6]), metamagnetic transformation (NiMnSn[7]), high magnetic ordering temperature and moment (Co_2FeSi[8]), martensitic transformation (Ni_2MnGa[9]), substantial spin polarization (Co_2MnSi[10]), as well as sizeable magnetic anisotropy (Mn_3Ga[11]) with high prospective for spintronics, magnetocaloric, and energy applications. Besides, the extraordinary tunability of these materials allows for the designing of materials with

varied functionality.

1.1 Heusler Structure and bonding characteristics

Generally, the X_2YZ full-Heusler alloys with stoichiometric composition 2:1:1 crystallizes into a cubic $L2_1$ structure (Sp.Gr: $Fm\bar{3}m$).[12] The $L2_1$ unit cell consists of four interpenetrating fcc sub-lattices with four atoms as the basis, such that the X atoms are situated at $(\frac{1}{4},\frac{1}{4},\frac{1}{4})$ and $(\frac{3}{4},\frac{3}{4},\frac{3}{4})$ Wyckoff sites, and Y, Z atoms are respectively situated at $(\frac{1}{2},\frac{1}{2},\frac{1}{2})$ and (0,0,0) sites.

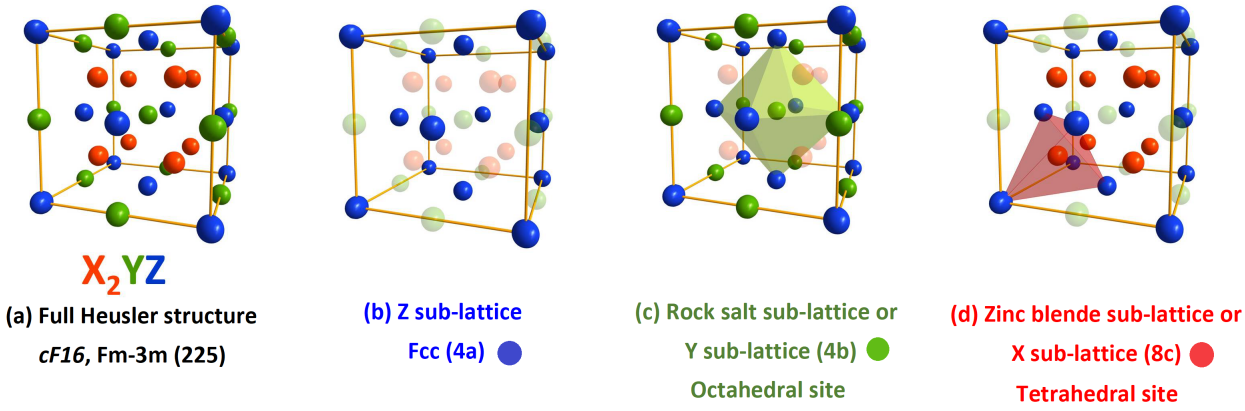

Figure 1.1: (a) $L2_1$ Heusler structure (b) Z sub-lattice (c) Rock salt sub-lattice (d) Zinc blende sub-lattice of Heusler alloys.

The structure of X_2YZ Heusler alloy is illustrated in Fig. 1.1 (a).[12] A rock salt-type lattice is formulated by the most and least electropositive (Y and Z) elements (see Fig. 1.1 (c)). Because of the ionic nature of the interaction, the Y and Z elements are octahedrally coordinated. Besides, all tetrahedral sites are filled by X atoms. The lattice constructed by a single X and the Z atoms formulates a zinc blende-type lattice (see Fig. 1.1 (d)).

1.2 Antisite disorder and its implications

1.2.1 Antisite disorder

Until now, we have only discussed the perfectly ordered Heusler structure, wherein every atom sits at its designated Wyckoff site. However, it is always possible, and in actuality often observed, that certain atoms interchange their Wyckoff sites. Such a structural defect is referred to as 'Antisite disorder'.[13,14] Most of the naturally existing materials, or the ones prepared in the laboratory, do exhibit some minor percentage of antisite disorder. Such a disorder is usually seen in ternary or more compounded oxides and alloys.

Generally, the disorders are entropy-driven. For instance, a particular type of disorder can turn out to be stable at higher temperatures. It is also probable that at room temperature, a disordered structure can remain more stable than the ordered one. The stability of various kinds of disorder gives rise to the distributed regimes in temperature.[15] To improve the atomic ordering for example in bulk or thin films, an annealing experiment has to be designed keeping in mind the particular ordering regime. Therefore, a well-developed annealing profile is essential in order to attain the maximum possible atomic ordering in the minimum period. The annealing time, as well as temperature, performs a more crucial role, especially in matters of thin films.[16] Hence, if one wants to obtain a largely ordered sample, it is necessary to recognize the temperature related to the respective order-disorder transitions for a particular material. Here, it should be noted that the above-discussed cases assume the presence of total order or disorder. However, in practicality, a small percentage of the lattice can be disordered, while the remaining

can be ordered. Sometimes, a mixture of many disorders too can occur.

1.2.2 Types of antisite disorders

Based on the atomic sites being exchanged, various kinds of antisite disorders can occur in Heusler alloys. One possibility is the exchange of Y and Z atoms. In an ordered $L2_1$ Heusler structure, if Y and Z atoms are arbitrarily intermixed on their 4b and 4a crystallographic sites, the B2-type disorder gets established.[14] When a complete intermixing of Y and Z sites occurs then the structure transforms from $L2_1$ to a B2 structure. In this structure the Y and Z crystallographic sites are identical and the composition simply becomes $X_2Y'_2$ or XY'.

The B2 structure also can be explained based on the CsCl-type lattice illustrated in Fig. 1.2. As a consequence of intermixing (Y and Z atoms), the symmetry of $L2_1$ structure is reduced, and the CsCl structure with an X atom at the center of a cube (1b) arbitrarily surrounded by Y and Z atoms (1a) with $Pm\bar{3}m$ space group is attained.

The next possibility is the mixing of X and Y atoms. If X and Y atoms are arbitrarily and equally distributed on 8c and 4b crystallographic sites of $L2_1$ structure, the DO_3-type disorder gets established. The resulting structure in the presence of DO_3 disorder is referred to as DO_3 structure with BiF_3 prototype and $Fm\bar{3}m$ space group. For DO_3 structure, the lattice constant remains the same as that of the full Heusler. The transformation from $L2_1$ to DO_3 structure is illustrated in Fig. 1.2.

It is also possible that all X, Y, and Z atoms are completely intermixed onto their crystallographic sites. Such intermixing results in A2-type disorder. In the presence

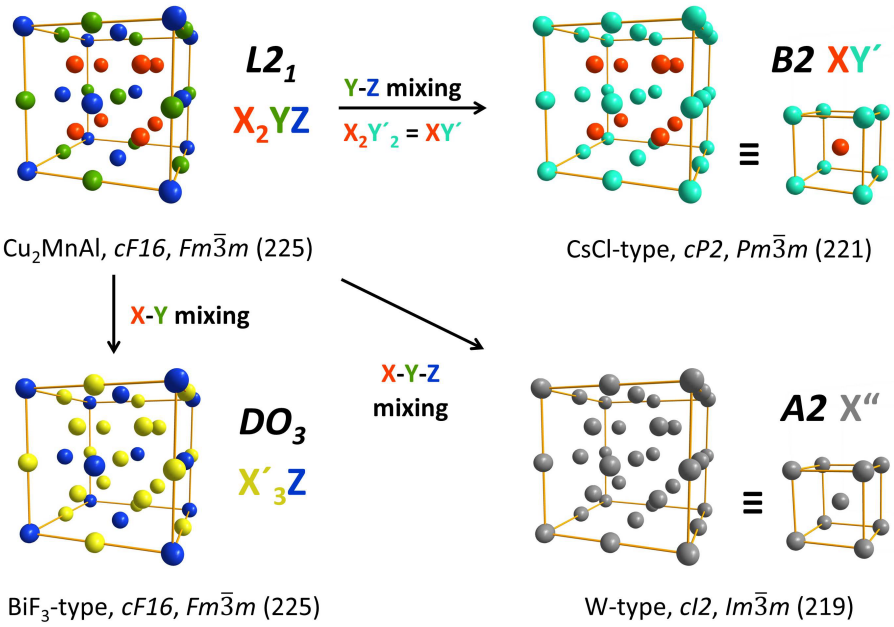

Figure 1.2: Structural transformation from ordered $L2_1$ Heusler structure to B2, DO_3, and A2 type structures respectively resulting from the intermixing of Y-Z, X-Y, and X-Y-Z atoms.

of this disorder, all the crystallographic sites become identical, leading to an A2-type structure with a W prototype and an $Im\bar{3}m$ space group shown in Fig. 1.2. Besides, similar to the case of the B2 structure, the effective cell parameter of the resulting A2 structure becomes half of the $L2_1$ structure. Apart from the above-mentioned antisite disorders, a few other kinds of disorders also have been reported. Table 1.1 puts forward the commonly observed antisite disorders in Heusler alloys.[1,17]

1.2.3 Driving factors behind disorders and defects

A material can possess different types of defects like point defects, stacking faults, dislocations, etc.[18] In a material, these defects are primarily set on by the entropy.[19] Also, an energy barrier is connected with the formation of a defect. In a solid, at any point in time and in any condition, there is a tiny percentage of particles which has elevated energy, that

Table 1.1: Consider reordering as General formula, space groups related to various types of atomic orders in Heusler alloys, and associated antisite disorder. (The notations as per ICSD (Inorganic Crystal Structure Database), SB (Strukturberichte), and Pearson database are given.)[17]

Antisite disorder	**General formula**	**ICSD Structure type**	**SB**	**Pearson**	**Space group**
X, X', Y, Z	$XX'YZ$	LiMgPdSn	Y	cF16	*F-43m (no. 216)*
$X = X$, Y, Z	X_2YZ	Cu_2MnAl	$L2_1$	cF16	*Fm-3m (no 225)*
X, $X' = Y$, Z	XX'_2Z	$CuHg_2Ti$	X	cF16	*F-43m (no 216)*
$X = X' = Y$, Z	X_3Z	BiF_3	DO_3	cF16	*Fm-3m (no 225)*
$X = X'$, $Y = Z$	X_2Y_2	CsCl	B2	cP2	*Pm-3m (no 221)*
$X = Y$, $X' = Z$	$X_2X'_2$	NaTl	B32a	cF16	*Fd-3m (no 227)*
$X = X' = Y = Z$	X_4	W	A2	c12	*Im-3m (no 229)*

is exhibited as thermal vibrations. This elevated energy of particles is perhaps enough for them to overcome the energy barrier for creating a defect. As a result, there is always an equilibrium percentage of defect present within a material at any particular temperature, preferably proceeding to zero at 0 K. Hence, it should be noted that at room temperature too, there is an equilibrium mass of the defects. However, at the same time (at room temperature), the proportion of defects is constant in a material due to the role played by the kinetics. Hence, the proportion of defects also relies on the material synthesis route.

Different intrinsic factors, such as valence, atomic radii, electronegativity, etc of the constituent atoms can lead to the formation of disorders and defects in materials. Certain atoms may choose a particular local environment or a specific atomic position depending upon their valency as well as electronegativity, resulting into a disorder. This type of situation is possible in Heusler alloys too. The robust site occupancy in these alloys results in a disorder, and hence their structures may need to be defined differently.[17,20]

For instance, such site preferences are observed in the alloys of the type $Mn_2Ni_{(1+x)}Z_{(1-x)}$, where the site preference of a transition metal gives rise to a structural disorder.[21] Other than electronegativity, the corresponding size of the constituent elements may also be a probable cause of the disorder. If the atomic radius of an element is fairly small in comparison with the rest of the elements involved, the energy needed to shift that particular element to the interstitial site can be satisfied by entropy alone. Moreover, similar vacancies and site disorders/defects can be more obvious based on the kind of bonding. Covalent, metallic, and ionic bonds have relatively dissimilar bond strengths depending on the type of element and can experience the creation of defects under favorable situations. Therefore, the characteristics of the elements constituting a material perform a crucial role in the likelihood of disorder and defects.

Besides the reality that significant defects within a material are created during the time of their preparation, it is also possible that additional defects can be caused at the time of further processing. In an idealized cooling, any sample must be cooled at an immeasurably slow rate to room temperature, that is unfeasible. The employed finite rate of cooling in real-world situations results in the formation of defects due to thermal shock as a consequence of expansion/contraction at the time of variation of the temperature. The greater the rate of quenching, the greater the possibility that the defect will be created in a material. Apart from this, additional processes like cutting, pulverization, and polishing of the sample during its preparation can also cause strains and defects via stresses. Also, the defects can be induced by irradiating the material with high-energy

neutrons, electrons, or ions during the time of synthesis of the sample.[22] Hence, it is important to take into consideration the likelihood of the generation of defects at the time of preparation, processing, and experimentation.

1.2.4 Effect of antisite disorder on Heusler alloys.

The experimental and theoretical studies on Heusler alloys have seen that the ordering of the atoms on their crystal lattices has a huge influence on their characteristic properties. Besides, an essential tool in the logical designing of the material of this class lies in accurately controlling the correlation between their atomic ordering and physical properties. Some of the examples citing the effect of antisite disorder on the structural, magnetic, and electronic properties of Heusler alloys are given below.

A study on $Pd_2MnIn_{1-x}Sn_x$ and $Pd_2MnIn_{1-y}Sb_y$ alloys reported the ramifications of B2-type disorder in them. The presence of this disorder was found to generate the antiferromagnetic interactions in these alloys as a result of the modifications in the sublattices. Although these modifications did not impact the Mn moment.[23] Further, the band structure calculations performed for PtMnSb, by involving the lattice defects observed its substantial effect on the spin polarization. This observation was also confirmed by the x-ray absorption measurements.[24] Generally, the transport measurements provide an indirect pathway for studying the structure and atomic ordering. It is well known that the behaviour of change of resistivity as a function of temperature is greatly affected by the disorder in the materials.[20] The study of anomalous Hall effect in the thin films of $Co_2FeSi_{0.6}Al_{0.4}$ and $Co_2FeGa_{0.5}Ge_{0.5}$ showed a distinct impact of the different types

of antisite disorder on the anomalous Hall signal.[25] Basically, this study has observed that, while the B2 disorder causes an enhancement in anomalous Hall signal, the DO_3 disorder affects its negativity. A theoretical calculation performed by incorporating a disorder in Fe_2VAl lattice has shown that incorporation of any kind of disorder enhances the spin moment of the alloy making it magnetically active.[26] Fe_2VAl has a valence electron count equal to 24 which makes its magnetization equal to zero as per the Slater-Pauling rule. However, experimentally the alloy did not show the zero net magnetic moment. This anomaly between the experimentally observed and calculated moment is resolved by realizing the presence of antisite disorder in the alloy. The antisite disorder is also known to induce the magnetic glassy phase in Heusler alloys. For instance, theoretical calculations predicted a non-magnetic state for Cu_2CrAl, however, the superparamagnetic conduct was noted. This observed behavior was assigned to the competitive interaction in between the direct antiferromagnetism and the indirect long-ranged ferromagnetism, emerging as a result of atomic disordering. Further, a similar magnetic conduct was seen for Fe_2VAl, Fe_2VGa and Fe_2TiSn Heusler alloys.[27,28] The antisite disorder is well-known to cause the metamagnetic and martensitic transformations in Heusler alloys.[29,30] The evolution of the magnetocaloric effect has been predicted in Mn_2NiX-type alloys as a result of disordering between Ni and one of the Mn sub-lattices.[31] Besides, the study on Ni-Co-Mn-In systems also has shown disordering to remarkably escalate the change in the peak magnetic entropy, which is required for magnetocaloric applications.[32] The zero field cooled exchange bias effect as a consequence of antisite disorder is observed in

$Mn_{2.4}Pt_{0.6}Ga$.[33] Usually, the disordering has been shown to have an adverse effect on the spin-dependent characteristics of half-metallic alloys. Their density of state gets affected as a consequence of the atomic rearrangement within a crystal structure. The disorders can either preserve the half-metallicity or it can terminate it completely while deforming the energy band bap of the minority density of states.[34] For example, in Co_2MnSi, putting the Co atom at Mn or Si site terminates half metallicity as a result of the creation of the minority spins states in the band gap.[35]

1.3 Magnetism in Heusler alloys

The family of Heusler alloys is well-known to exhibit diverse magnetic phenomena such as localized and itinerant magnetism, ferro- or ferrimagnetism, antiferromagnetism, half-metallicity, Pauli paramagnetism, heavy-fermionic behavior, helimagnetism, spin-glassy behavior, etc.[14,36,37] The crystal structure of these alloys has an immense impact on their magnetic properties. Most of these alloys order ferromagnetically and easily saturate in the presence of a weak magnetic field. In the magnetic Heusler alloys, typically the Y site is occupied by 3d transition metal like from V to Ni, whereas the X site is occupied by 3d, 4d, and 5d elements. The ferromagnetism in Mn-based Heusler alloys of the X_2MnZ-type arises from the indirect RKKY exchange interaction between localized magnetic moments of Mn atoms at a distance greater than 4 Å, mediated by conduction electrons.[38,39]

Extensive studies have been carried out on ordered quaternary Heulser alloys to understand the role of 3d elements as X and sp elements as Z atoms in the magnetism of

Heusler alloys.[40,41] The study has observed s and p electron concentrations to fundamentally contribute to the magnetism of these alloys. It has been found to affect the spin moments in addition to the magnetic order of the alloy.[42] The DFT calculations have shown that while going from a series with Ni as X element to a series with Co as X element, the RKKY exchange interaction amongst p and d elements deteriorates, and the d-d exchange interaction escalates. Few of the Heusler alloys order antiferromagnetically. Experimentally, the antiferromagnetic order is observed in $L2_1$ and B2 full and $C1_b$ half-Heusler alloys. In a B2-type structure, antiferromagnetism becomes favorable due to the smaller Mn-Mn interatomic distance.[36] Further, the scenario is completely different in half-Heusler alloys. Because of large Mn-Mn inter-atomic bond lengths in the $C1_b$ structure, the antiferromagnetic exchange interaction among Mn atoms is believed to take place via intermediate X or Z atoms. Finally, the ferrimagnetic ordering is a bit rare in the Heusler alloys in contrast to the ferro- or antiferromagnetic order. The alloys such as Mn_2VAl, Mn_2VGa, and CoMnSb are known to display ferrimagnetism. Mn_2VAl have gained a lot of experimental attention because in this alloy the Mn tends to sit at the X site which is different from the alloys where Mn sits at the Y site.[43]

1.4 Martensitic transformation

One of the interesting properties of the Heusler alloys is the shape memory. Shape memory results due to a solid-solid, first-order, shear-like displacive (diffusionless) structural transformation between a high-temperature austenite (cubic) phase and a low-temperature

(tetragonal, orthorhombic, or monoclinic) martensite phase.[44] However, due to the internal stresses, the structurally transforming high-temperature phase gets stabilized into an intermediate phase referred to as modulated phase. In martensitic phase transformation, both atomic shuffling, as well as lattice distortive strain, can be involved. This transformation takes place by nucleation plus the growth of the martensitic phase within the austenitic parent lattice as displayed in Fig. 1.3 (a) via lattice distortion (for instance, a cubic to tetragonal lattice distortion as displayed in Fig. 1.3 (b)). During this process, a huge strain is instigated over the entire phase boundary of the martensite. The further advancement of the nucleation and growth process needs the lowering of this strain energy, which is achieved by 'slip' and 'twinning' respectively displayed in Fig. 1.3 (c), (d) and is referred to as 'lattice invariant strain'.[45,46] The process by which the strain is minimized is known as 'strain accommodation'. The twin structures which are differently oriented are known as 'twin variants' and the junction between the twins is known as the 'twin boundary'.

Since the martensitic transformation is the first-order transformation, it never follows back the same path. Hence hysteresis arises during the time of cooling and heating. The distinguishable transformation temperatures while heating are austenitic start (A_s), austenitic finish (A_f) and while cooling are martensitic start (M_s), martensitic finish (M_f). Below M_f, the alloy is entirely composed of martensitic variants, and then after heating over A_f temperature, the austenite phase is completely reconstructed.

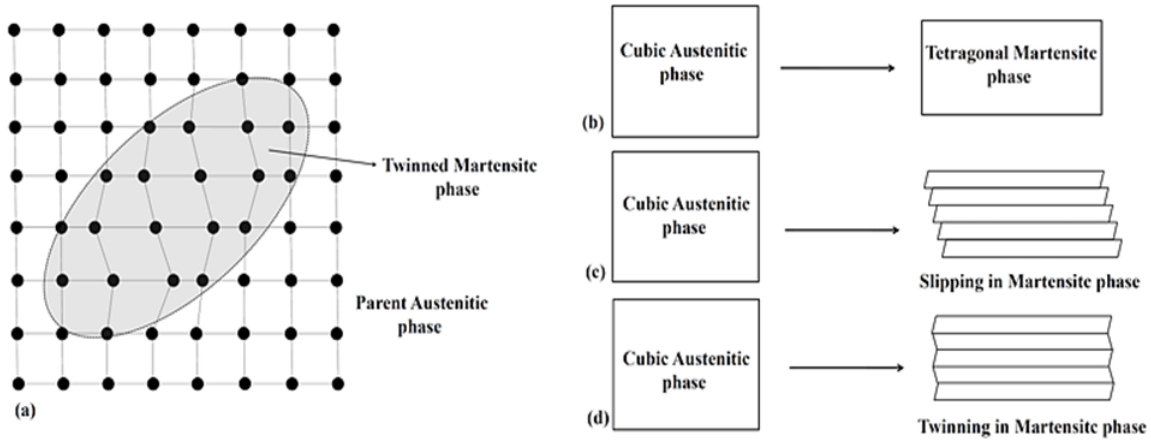

Figure 1.3: Schematic illustration of (a) growing martensitic phase within an austenitic parent phase, (b) transformation of crystal structure, accommodation of strain through (c) slipping, (d) twinning.

1.4.1 Martensitic transformation temperature and e/a ratio.

Among the stoichiometric Ni_2MnZ-type (where Z = Ga, Sn, Al, In, Sb) alloys, only Ni_2MnGa is known to undergo martensitic transformation at about 220 K with nearly insignificant change in the volume across the transformation.[47] However, the rest of the alloys undergo the same transformation in their off-stoichiometric form, which takes place via volume change, for instance, in the alloys of the type $Ni_2Mn_{(1+x)}Z_{(1-x)}$ with Z= Sn, In or Sb.[48] These alloys in the austenite state have an $L2_1$ crystal structure as shown in Fig. 1.4 (a). In the stoichiometric compositions, Ni, Mn, and Z respectively sit at 8c, 4a, and 4b Wyckoff position respectively.[9,47] When the alloy temperature is reduced, it experiences a martensitic transformation. The Ni-Mn-Z alloys distinctively get transformed into $L1_0$ (tetragonal) structure, which is the ground-state crystal structure of NiMn.[49] The correlation between the $L2_1$ austenite and tetragonal martensite structure is displayed in Fig. 1.4. Typically, for Heusler alloys, the seven-fold (7M or 14M) and five-

fold (5M or 10M) modulated structures are observed. Here, M stands for monoclinicity developed from the distortion related to the modulation.

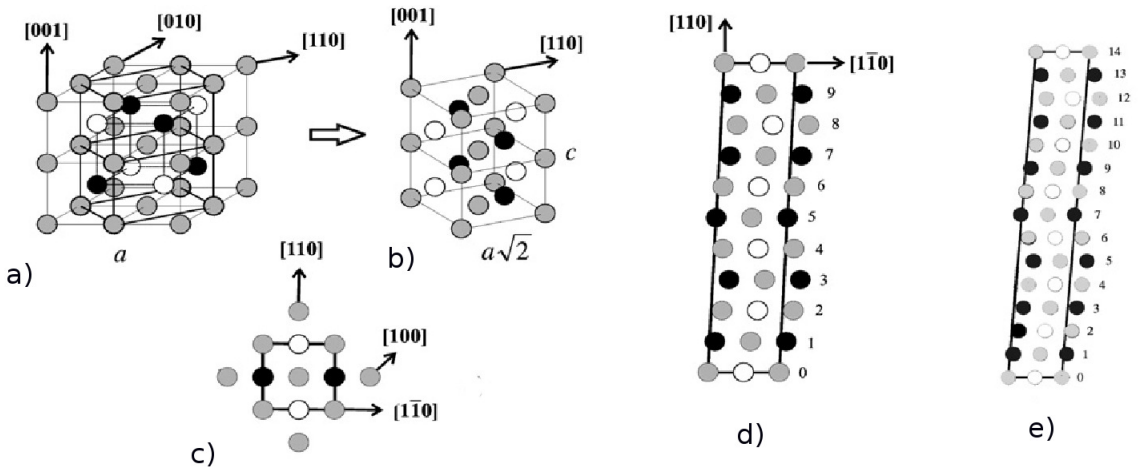

Figure 1.4: The correlation between the $L2_1$ cubic austenite and $L1_0$ tetragonal martensite structure. (a) austenite $L2_1$ structure. (b) The tetragonal martensite structure. (c) The top view of the tetragonal martensite structure. (d) and (e) The generated modulated structures for 5M and 7M phases respectively

.

In the case of Hume-Rothery alloys which are non-magnetic in nature, the martensitic transformation occurs at the time when the fermi surface extends to the Brillouin zone boundary. This finding suggested that even in Heusler alloys too, the variation in valence electron concentration and the modification of Brillouin zone boundary may be observed as the key impelling cause for the happening of martensitic transformation.[9] Thus, for the Heusler alloys, the martensitic transformation temperatures ('T_M') were arranged as the function of average valence electron concentration per atom (e/a) ratio,[50–52] wherein the 'T_M' was found to scale linearly with the 'e/a' ratio. This perspective was brought in by Chernenko et al. who estimated the e/a ratio for Ni_2MnGa by utilizing the outer shell electron concentration of all chemical components of the alloy.[53] Such a dependency was

found to be applicable for the huge number of alloys, proposing its good applicability,[53] for example, in $Ni_2Mn_{1+x}Z_{1-x}$ alloys where Z is Sn, In or Ga, shown in Fig. 1.5.[49,54–56]

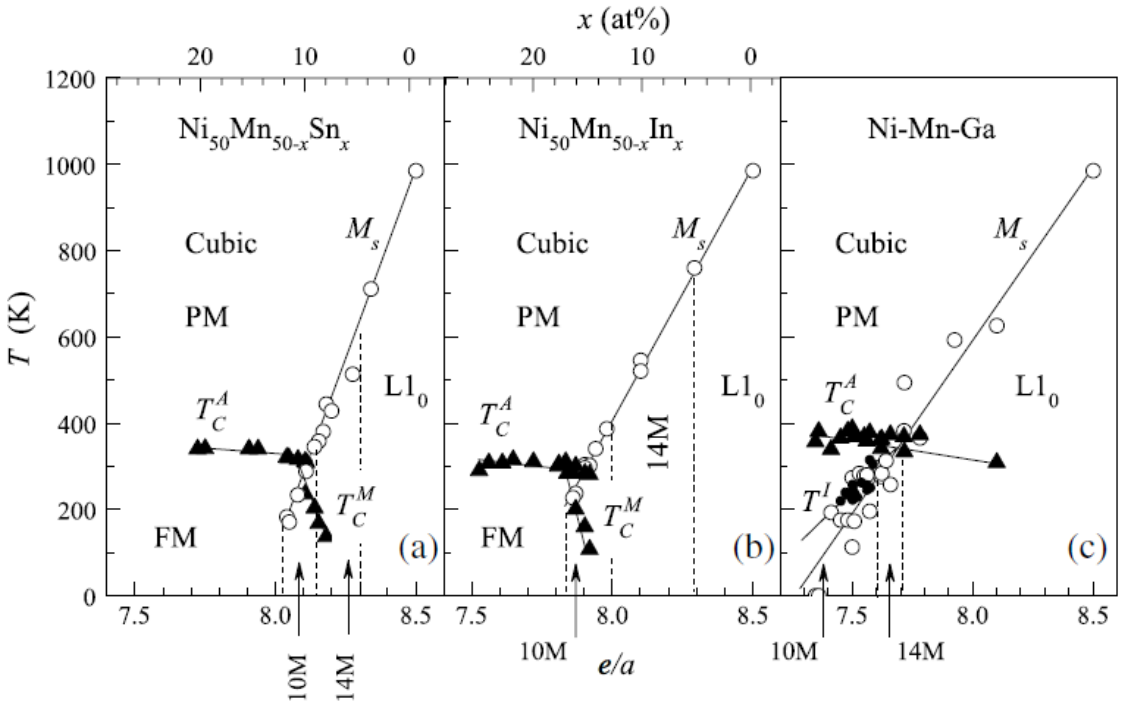

Figure 1.5: (a), (b), and (c) represents the structural and the magnetic phase diagram for the Heusler alloys of the type Ni-Mn-Z with Z respectively as Sn, In, and Ga. The open circles and solid triangles correspond to the martensitic and magnetic transformation temperatures. Besides, solid small circles in (c) represent the premartensitic transformation temperatures. The phase diagram is divided into different regions using dotted lines corresponding to various crystal structures. The compositions of the alloy in terms of at.% is specified on the upper axis. T_C^A and T_C^M respectively represent the ferromagnetic magnetic ordering temperatures in austenitic and martensitic states. M_s represents the martensitic start temperature. For all the three-phase diagrams, with increasing e/a ratio the ground-state crystal structure advances from cubic to 10 M to 14 M and then to $L1_0$.

However, one exception to this so-called 'e/a rule' is Mn_2NiGa which has an e/a ratio of 6.75 as compared to 7.5 of Ni_2MnGa, but undergoes the martensitic transformation at about $T_M \approx 270$ K.[57] Mn_2NiGa is achieved by replacing one of the Ni sub-lattices at X sites by Mn in $Ni_{2-x}Mn_{1+x}Ga$ with $0 \leq x \leq 1$, where the T_M first decreases with decreasing e/a ratio but beyond $x = 0.5$ increases despite a decline in the e/a ratio.[58,59]

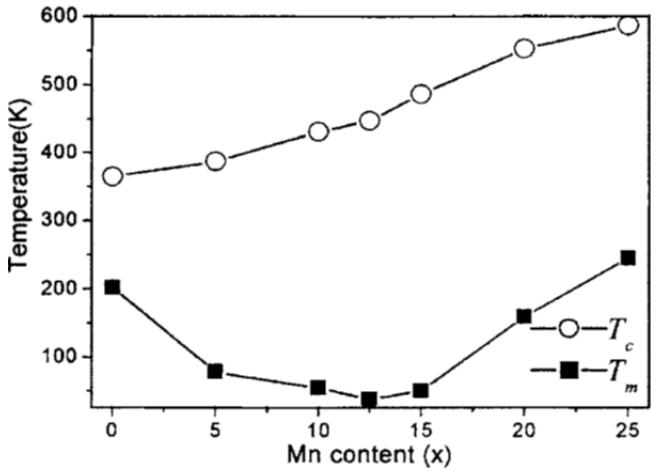

Figure 1.6: The composition dependence of martensitic transformation temperature (T_M) and magnetic ordering temperature (T_C) for $Mn_{25+x}Ni_{50-x}Ga_{25}$ alloys with x = 0, 5, 10, 12.5, 15, 20, 25.

So far, there is no complete understanding of this unexpected behavior.

1.5 Mn_2YZ systems

The Mn_2-based Heusler alloys, featured by antiparallel coupling of Mn moments that orders ferrimagnetically, have attracted much attention because of their properties such as small magnetic moment, large coercivity, large magnetocrystalline anisotropy, high magnetic ordering temperature, etc finding applications as a spintronic and hard magnetic material.[33,60–62] Alloys of the type Mn_2NiZ that have greater Mn content than Ni_2MnZ are considered advantageous in realizing superior magnetic, magnetotransport, magnetocaloric properties.[62,63] Mn_2NiGa is one of the well-known shape memory alloys that orders magnetically at T_C = 588 K and exhibits a magnetic field-induced strain (MFIS) of $\sim$ 4%. It was mainly synthesized with the intention to have better functionalities than Ni_2MnGa.[58] Further, Mn_2NiSn orders magnetically at T_C = 530 K and has gained

substantial attention due to its predicted volume-conserving martensitic transformation. However, a discrepancy exists related to its theoretically calculated and experimentally measured magnetic moment values. While its measured net spin moment at 5 K was 2.95 μ_B/f.u.,[64] the calculated moment widely differed from 0.7 μ_B/f.u. to 3.25 μ_B/f.u.[64,65] Furthermore, Mn_2PtIn exhibits the topological Hall effect.[66] A large exchange bias effect is observed in $Mn_{2.4}Pt_{0.6}Ga$.[33] Mn_2CoAl is a spin gapless semiconductor with T_C = 720 K.[67] One of the extensively studied alloys from this class of materials is Mn_3Ga.[14] A magnetic alloy with an anisotropic structure can give rise to giant magnetocrystalline anisotropies. Besides, based on the value of magnetocrystalline energy, the direction of the orientation of preferred magnetization can be adjusted from out-of-plane to in-plane. Mn_2RhSn is a novel tetragonal system that exhibits the noncollinear type of magnetism and has provided evidence for the existence of skyrmionic objects.[68] Even in an antiferromagnet, the combination of Berry curvature in k-space and the noncollinear magnetic spin structure has led to an anomalous Hall effect. This phenomenon for the first time was observed in antiferromagnetic hexagonal Mn_3Ge and Mn_3Sn.[69,70] These hexagonal compounds are observed in the phase diagram of the Mn-rich Heusler alloys at elevated temperatures. Within the hexagonal system, layers of Mn atoms showcase a kagome spin alignment leading to magnetic frustration. The prospect of modifying the Berry phase curvature illustrates the significance of understanding both the magnetic and electronic structures of these Heusler alloys.

1.5.1 Crystal structure and magnetism of Mn_2YZ alloys.

Mn_2YZ alloys are known to crystallize into an inverse Heusler (XX'YZ) or $L2_1B$ structure.[12,71] Further, the intermixing of Wyckoff positions is often observed in this class of materials, which leads to the various disordered crystal structural variants of the parent structure.[12] The additional crystal structures within the phase space of Mn_2YZ alloys are tetragonal and hexagonal structures respectively, attained by distorting the cubic parent phase along [001] and [111] directions illustrated in Fig. 1.7.

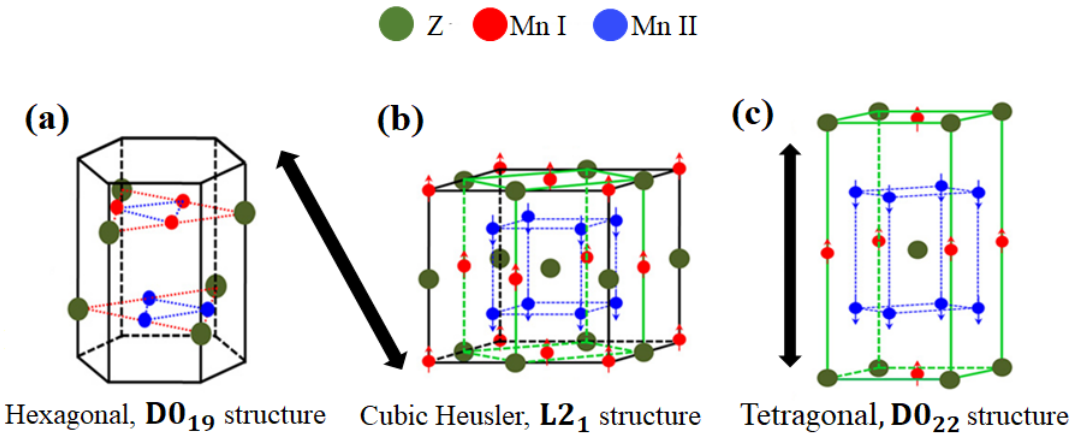

Figure 1.7: The structural transformation via lattice distortion from an $L2_1$ to the hexagonal structure (a) and the tetragonal structure (c).

The class of Mn_2YZ Heusler alloys is relatively novel in contrast to other classes like Ni_2YZ, Co_2YZ, and Fe_2YZ. One of the distinct features of Mn_2YZ alloys is that, generally they showcase magnetization which is less than 2 μ_B/f.u. However, in the alloys that constitute rare earth elements, the magnetization can even reach up to 4 μ_B that is in line with the Slater-Pauling rule wherein it is classified in two different curves. One curve with average valence electron (N_V) concentration less than 24 that possesses the $L2_1$-

type crystal structure and another curve with average valence electron (N_V) concentration greater than 24, that possessing X_a-type crystal structure.[72] The Mn-based Heusler alloys get crystallized into $L2_1$ and X_a type crystal structures depending upon the Y atom type whether it is an early transition metal '3d' element or the late transition element '4d' element respectively. Likewise, the alignment of the spin moments between parallel to anti-parallel happens based on the occupancy of Mn atoms on the various lattice positions.

For Mn_2YZ alloys, the formation energy estimated for both early and late transition elements sitting at the Y site anticipates that when Y takes up the elements from Ti to Cr and Zr to Mo, the $L2_1$-type structure becomes stable whereas when Y takes up the elements from Fe to Cu and Ru to Ag, the X_a-type structure is stable. The contrast between the sum energy of regular and inverse Heusler structures verified the site occupancy energy of the specified composition. From the estimation, it is clear that early transition elements sit at the 4b atomic site. The stability of the phase is dependent on the type of metal sitting at the Y site.

1.6 Objectives:

The main motivation for the present work is the plethora of interesting ground states exhibited by Mn_2XZ alloys. We have focused our attention on two families of alloys (a) $Ni_{2-x}Mn_{1+x}Ga$ and (b) $Ni_{2-x}Mn_{1+x}Sn$ with ($0 \leq x \leq 2$). In the first family, we study the evolution of martensitic and magnetic properties of the alloys with increasing Mn content. Typically, the martensitic transformation temperature of magnetic shape

memory alloys scales with its e/a ratio; however, in $Ni_{2-x}Mn_{1+x}Ga$, the T_M initially decreases and then increases with decreasing e/a ratio. Mn_2NiGa (e/a = 6.75) transforms at a higher temperature T_M = 270 K then Ni_2MnGa (e/a = 7.5, T_M = 220 K).[59,73]

The second family of alloys was chosen due to its relatively simpler (cubic) structure and absence of martensitic transition. This will allow us to understand the role of excess Mn in the magnetic ground state of these alloys. Literature reports a discrepancy related to the theoretically calculated and experimentally measured magnetic moment values of Mn_2NiSn which has been attributed to the presence of an antisite disorder. The present study will enable the examination of the structural stability of the Heusler structure in the presence of antisite disorder.

Increasing the Mn concentration beyond $x = 1$ in both the families gives rise to antiferromagnetic Mn_3Ga[74] and Mn_3Sn[6] alloys. The structural evolution from Mn_2NiZ to Mn_3Z (Z = Ga or Sn) is via a multiphasic region. There is a small region of doping concentration wherein the resulting alloys have the same structure as the two end members, Mn_3Ga and Mn_3Sn. As both Mn_3Ga and Mn_3Sn have been discussed in current literature, it will be interesting to study the effect of Ni doping on the physical properties of these alloys. Hence the present work is undertaken with the following objectives:

1. To understand the violation of the e/a rule in $Ni_{2-x}Mn_{1+x}Ga$ ($0 \leq x \leq 1$) and the role of antisite disorder by investigating the local and crystal structures of the alloys.

2. To explore the structural stability of $Ni_{2-x}Mn_{1+x}Sn$ ($0 \leq x \leq 1$) alloys and the role

of antisite disorder in their magnetic and transport properties.

3. To study the implications of substitution of Mn by Ni on the magnetic ground state of antiferromagnetic cubic Mn_3Ga.

4. To investigate the effect of Ni substitution on the magnetic and electronic ground state of Mn_3Sn.

The thesis consists of seven chapters, and a brief overview of each chapter is as follows:

Chapter 1 begins by introducing the Heusler alloy and its crystal structure, followed by a short literature review highlighting the applications. Further, a brief introduction to antisite disorder and its implications are presented. Next, the Martensitic transformation and the e/a ratio in Heusler alloys are discussed. Then, the magnetism in Heusler alloys is talked about. Further, a brief description of the structure and magnetism in Mn_2YZ alloys is given. Finally, the chapter specifies the objectives of the thesis.

Chapter 2 describes sample preparation techniques and various strategies employed during the synthesis of the proposed Heusler alloys. A brief description of different characterization techniques used during the present work is also given in this chapter.

Chapter 3 presents the structural (crystal and local) and magnetic properties of the series of $Ni_{2-x}Mn_{1+x}Ga$ with (x = 0, 0.25, 0.5, 0.75, and 1) alloys. This chapter mainly explains how the antisite disorder leads to the structural defects that play a key role in the resulting martensitic properties of these Mn-rich alloys.

Chapter 4 presents the structural (crystal and local), magnetic, and transport prop-

erties of the series of $Ni_{2-x}Mn_{1+x}Sn$ with (x = 0, 0.25, 0.5, 0.75, and 1) alloys. This chapter mainly explains the role of antisite disorder in the metastability of Mn_2NiSn, which eventually answers the existing discrepancy in the experimentally measured and theoretically calculated magnetic moments of Mn_2NiSn.

Chapter 5 discusses the results of the investigation carried out to understand the effect of local structural distortions on structural (crystal and local) and magnetic properties of $Mn_{3-x}Ni_xGa$ alloys with (x = 0 and 0.25) alloys.

Chapter 6 puts forward the investigation carried out to understand the effect of local structural distortions on structural (crystal, local, and magnetic), magnetic, transport, and magneto-transport properties of $Mn_{3-x}Ni_xSn$ alloys with (x = 0 and 0.25).

Chapter 7 presents the summary of the accomplished work and the future plan.

References

[1] T. Graf, S. S. P. Parkin, and C. Felser. *IEEE Transactions on Magnetics*, 47(2):367–373, 2010.

[2] F. Heusler, W. Starck, and E. Haupt. *Verhandlungen der Deutschen Physikalischen Gesellschaft*, 5:219–232, 1903.

[3] Y. Oner, O. Kamer, E. Alveroglu, M. Acet, and T. Krenke. *Journal of Alloys and Compounds*, 429(1-2):64–71, 2007.

[4] C. Pfleiderer, J. Boeuf, and H. V. Löhneysen. *Physical Review B*, 65(17):172404, 2002.

[5] Y. Nishino, M. Kato, S. Asano, K. Soda, M. Hayasaki, and U. Mizutani. *Physical Review Letters*, 79(0):1909–1912, 1997.

[6] S. Nakatsuji, N. Kiyohara, and T. Higo. *Nature*, 527(7577):212–215, 2015.

[7] Q. Tao, Z. D. Han, J. J. Wang, B. Qian, P. Zhang, X. F. Jiang, D. H. Wang, and Y. W. Du. *AIP Advances*, 2(4):042181, 2012.

[8] C. G. F. Blum, C. A. Jenkins, J. Barth, C. Felser, S. Wurmehl, G. Friemel, C. Hess, G. Behr, B. Buchner, A. Reller, S. Riegg, S. G. Ebbinghaus, T. Ellis, P. J. Jacobs, J. T. Kohlhepp, and H. J. M. Swagten. *Applied Physics Letters*, 95(16):161903, 2009.

[9] P. J. Webster, K. R. A. Ziebeck, S. L. Town, and M. S. Peak. *Philosophical Magazine B*, 49(3):295–310, 1984.

[10] W. H. Wang, M. Przybylski, W. Kuch, L. I. Chelaru, J. Wang, Y. F. Lu, J. Barthel, H. L. Meyerheim, and J. Kirschner. *Physical Review B*, 71(14):144416, 2005.

[11] R. M. Gutiérrez-Pérez, D. I. Zubiate-Pérez, R. L. Antón, M. E. Fuentes-Montero, J. T. Holguín-Momaca, O. O. Solís-Canto, A. Alvídrez-Lechuga, J. A. Gonzalez, and S. F. Olive-Méndez. *Surfaces and Interfaces*, 35:102427, 2022.

[12] T. Graf, C. Felser, and S. S. P. Parkin. *Progress in Solid State Chemistry*, 39(1):1–50, 2011.

[13] G. E. Bacon and J. S. Plant. *Journal of Physics F: Metal Physics*, 1(4):524, 1971.

[14] C. Felser and A. Hirohata. *Heusler Alloys*. Springer, 2015.

[15] J. Sołtys. *Physica Status Solidi (A)*, 66(2):485–491, 1981.

[16] C. Gusenbauer, T. Ashraf, J. Stangl, G. Hesser, T. Plach, A. Meingast, G. Kothleitner, and R. Koch. *Physical Review B*, 83(3):035319, 2011.

[17] T. Graf, F. Casper, J. Winterlik, B. Balke, G. H. Fecher, and C. Felser. *Zeitschrift für Anorganische und Allgemeine Chemie*, 635(6-7):976–981, 2009.

[18] A. Kelly and K. M. Knowles. *Chichester, UK*, 2012.

[19] R. E. Smallman and R. J. Bishop. *Process, Applications 6th ed., Reed Educational and Professional Publishing Ltd*, 1999.

[20] D. N. Lobo, S. Dwivedi, C. A. DaSilva, N. O. Moreno, K. R. Priolkar, and A. K. Nigam. *Journal of Applied Physics*, 114(17):173910, 2013.

[21] J. Barth, B. Balke, G. H. Fecher, H. Stryhanyuk, A. Gloskovskii, S. Naghavi, and C. Felser. *Journal of Physics D: Applied Physics*, 42(18):185401, 2009.

[22] J. Mayer, L. A. Giannuzzi, T. Kamino, and J. Michael. *MRS Bulletin*, 32(5):400–407, 2007.

[23] P. J. Webster and M. R. I. Ramadan. *Journal of Magnetism and Magnetic Materials*, 20(3):271–276, 1980.

[24] H. Ebert and G. Schütz. *Journal of Applied Physics*, 69(8):4627–4629, 1991.

[25] E. V. Vidal, H. Schneider, and G. Jakob. *Physical Review B*, 83(17):174410, 2011.

[26] C. Venkatesh, V. Srinivas, V. V. Rao, S. K. Srivastava, and P. S. Babu. *Journal of Alloys and Compounds*, 577:417–425, 2013.

[27] A. Ślebarski, A. Wrona, T. Zawada, A. Jezierski, A. Zygmunt, K. Szot, S. Chiuzbaian, and M. Neumann. *Physical Review B*, 65(14):144430, 2002.

[28] D. J. Singh and I. I. Mazin. *Physical Review B*, 57(22):14352, 1998.

[29] D. N. Lobo, K. R. Priolkar, P. A. Bhobe, D. Krishnamurthy, and S. Emura. *Applied Physics Letters*, 96(23):232508, 2010.

[30] K. R. Priolkar, D. N. Lobo, P. A. Bhobe, S. Emura, and A. K. Nigam. *Europhysics Letters*, 94(3):38006, 2011.

[31] S. Paul, A. Kundu, B. Sanyal, and S. Ghosh. *Journal of Applied Physics*, 116(13):133903, 2014.

[32] S. Singh, I. Glavatskyy, and C. Biswas. *Journal of Alloys and Compounds*, 601:108–111, 2014.

[33] A. K. Nayak, M. Nicklas, S. Chadov, C. Shekhar, Y. Skourski, J. Winterlik, and C. Felser. *Physical Review Letters*, 110(12):127204, 2013.

[34] J. C. Slonczewski. *Journal of Magnetism and Magnetic Materials*, 159(1-2):L1–L7, 1996.

[35] B. Hülsen, M. Scheffler, and P. Kratzer. *Physical Review B*, 79(9):094407, 2009.

[36] H. P. J. Wijn. *Magnetic Properties of Metals: d-Elements, Alloys and Compounds*. 1991.

[37] J. Tobola, J. Pierre, S. Kaprzyk, R. V. Skolozdra, and M. A. Kouacou. *Journal of Physics: Condensed Matter*, 10(5):1013, 1998.

[38] J. Kübler. *Physica B+ C*, 127(1-3):257–263, 1984.

[39] S. E. Kulkova, S. V. Eremeev, and S. S. Kulkov. *Solid State Communications*, 130(12):793–797, 2004.

[40] D. C. Gupta and I. H. Bhat. *Materials Science and Engineering: B*, 193:70–75, 2015.

[41] D. C. Gupta and I. H. Bhat. *Journal of Magnetism and Magnetic Materials*, 374:209–213, 2015.

[42] J. Pons, V. A. Chernenko, R. Santamarta, and E. Cesari. *Acta Materialia*, 48(12):3027–3038, 2000.

[43] R. Weht and W. E. Pickett. *Physical Review B*, 60(18):13006, 1999.

[44] H. K. D. H. Bhadeshia. *Geometry of crystals*, volume 8. Institute of Materials London, 2001.

[45] K. Otsuka. *Shape Memory Materials*, pages 27–48, 1998.

[46] F. Therrien and V. Stevanović. *Physical Review Letters*, 125(12):125502, 2020.

[47] P. J. Webster. *Contemporary Physics*, 10(6):559–577, 1969.

[48] T. Krenke, E. Duman, M. Acet, E. F. Wassermann, X. Moya, L. Mañosa, A. Planes, E. Suard, and B. Ouladdiaf. *Physical Review B*, 75(10):104414, 2007.

[49] A. Planes, L. Mañosa, and M. Acet. *Journal of Physics: Condensed Matter*, 21(23):233201, 2009.

[50] A. Sozinov, A. A. Likhachev, and K. Ullakko. *IEEE Transactions on Magnetics*, 38(5):2814–2816, 2002.

[51] X. Jin, M. Marioni, D. Bono, S. M. Allen, R. C. O'handley, and T. Y. Hsu. *Journal of Applied Physics*, 91(10):8222–8224, 2002.

[52] I. Dikshtein, V. Koledov, V. Shavrov, A. Tulaikova, A. Cherechukin, V. Buchelnikov, V. Khovailo, M. Matsumoto, T. Takagi, and J. Tani. *IEEE Transactions on Magnetics*, 35(5):3811–3813, 1999.

[53] V. A. Chernenko. *Scripta Materialia*, 40(5):523–527, 1999.

[54] Y. Sutou, Y. Imano, N. Koeda, T. Omori, R. Kainuma, K. Ishida, and K. Oikawa. *Applied Physics Letters*, 85(19):4358–4360, 2004.

[55] A. Kimura, M. Ye, M. Taniguchi, E. Ikenaga, J. M. Barandiaran, and V. A. Chernenko. *Applied Physics Letters*, 103(7):072403, 2013.

[56] T. Krenke, E. Duman, M. Acet, E. F. Wassermann, X. Moya, L. Mañosa, and A. Planes. *Nature Materials*, 4(6):450–454, 2005.

[57] S. Singh, M. Maniraj, S. W. D'Souza, R. Ranjan, and S. R. Barman. *Applied Physics Letters*, 96(8):081904, 2010.

[58] G. D. Liu, J. L. Chen, Z. H. Liu, X. F. Dai, G. H. Wu, B. Zhang, and X. X. Zhang. *Applied Physics Letters*, 87(26):262504, 2005.

[59] P. J. Brown, T. Kanomata, K. Neumann, K. U. Neumann, B. Ouladdiaf, A. Sheikh, and K. R. A. Ziebeck. *Journal of Physics: Condensed Matter*, 22(50):506001, 2010.

[60] L. Feng, L. Ma, E. K. Liu, G. H. Wu, W. H. Wang, and W. X. Zhang. *Applied Physics Letters*, 100(15):152401, 2012.

[61] H. Luo, P. Jia, G. Liu, F. Meng, H. Liu, E. Liu, W. Wang, and G. Wu. *Solid State Communications*, 170:44–47, 2013.

[62] V. Alijani, J. Winterlik, G. H. Fecher, and C. Felser. *Applied Physics Letters*, 99(22):222510, 2011.

[63] K. Ullakko, J. K. Huang, C. Kantner, R. C. O'handley, and V. V. Kokorin. *Applied Physics Letters*, 69(13):1966–1968, 1996.

[64] H. Luo, G. Liu, Z. Feng, Y. Li, L. Ma, G. Wu, X. Zhu, C. Jiang, and H. Xu. *Journal of Magnetism and Magnetic Materials*, 321(24):4063–4066, 2009.

[65] S. Paul, A. Kundu, B. Sanyal, and S. Ghosh. *Journal of Applied Physics*, 116(13):133903, 2014.

[66] B. Giri, A. I. Mallick, C. Singh, P. V. P. Madduri, F. Damay, A. Alam, and A. K. Nayak. *Physical Review B*, 102(1):014449, 2020.

[67] S. Ouardi, G. H. Fecher, C. Felser, and J. Kübler. *Physical Review Letters*, 110(10):100401, 2013.

[68] O. Meshcheriakova, S. Chadov, A. K. Nayak, U. K. Rößler, J. Kübler, G. André, A. A. Tsirlin, J. Kiss, S. Hausdorf, A. Kalache, et al. *Physical Review Letters*, 113(8):087203, 2014.

[69] A. K. Nayak, J. E. Fischer, Y. Sun, B. Yan, J. Karel, A. C. Komarek, C. Shekhar, N. Kumar, W. Schnelle, J. Kübler, et al. *Science Advances*, 2(4):e1501870, 2016.

[70] M. Ikhlas, T. Tomita, T. Koretsune, M. T. Suzuki, D. Nishio-Hamane, R. Arita, Y. Otani, and S. Nakatsuji. *Nature Physics*, 13(11):1085–1090, 2017.

[71] S. Wurmehl, H. C. Kandpal, G. H. Fecher, and C. Felser. *Journal of Physics: Condensed Matter*, 18(27):6171, 2006.

[72] L. Wollmann, S. Chadov, J. Kübler, and C. Felser. *Physical Review B*, 90(21):214420, 2014.

[73] G. D. Liu, J. L. Chen, Z. H. Liu, X. F. Dai, G. H. Wu, B. Zhang, and X. X. Zhang. *Applied Physics Letters*, 87(26):262504, 2005.

[74] B. Balke, G. H. Fecher, J. Winterlik, and C Felser. *Applied Physics Letters*, 90(15):152504, 2007.

Chapter 2

Experimental Techniques

2.1 Introduction

This chapter first describes the different steps involved in the preparation of alloys under investigation. Subsequently, it gives a short description of different experimental methodologies employed for characterizing the alloys along with the respective data analysis techniques. The chemical composition of the synthesized alloys was determined using Energy-Dispersive X-ray (EDX) spectroscopy. While the crystal structure of the alloys was established via X-ray diffraction (XRD), the local structure around the constituent atoms was probed by X-ray Absorption Fine Structure (XAFS) spectroscopy. Neutron diffraction (ND) was employed to determine the magnetic structures. Further, the bulk magnetic studies were carried out using a Superconducting Quantum Interference Device (SQUID) magnetometer and a Vibrating Sample Magnetometer (VSM), and the transport properties like resistivity and Hall resistivity were measured using a conventional four-probe setup on a Close cycle refrigerator (CCR) and a Physical Properties Measurement System (PPMS) respectively.

2.2 Sample preparation

The polycrystalline alloy samples were synthesized using an arc melting furnace at the School of Physical and Applied Sciences, Goa University. Appropriate quantities of high purity ($> 99.9\%$) constituent elements were melted in a water-cooled copper hearth in a pure argon environment to avoid the contamination of melt from the atmospheric oxygen. The ingot was remelted two more times by flipping the ingot to achieve greater homogeneity. The obtained ingot was then cut into appropriate pieces for EDX, magnetic, transport, and magneto-transport property measurements, and the rest was finely powdered for the measurements such as XRD, ND, and EXAFS. All these pieces and powder (wrapped in tantalum foil) were sealed in a quartz tube under a vacuum of $\approx 10^{-6}$ mbar and subjected to the appropriate heat treatment. Fig. 2.1 illustrates the various pictures taken during the preparation of the alloys.

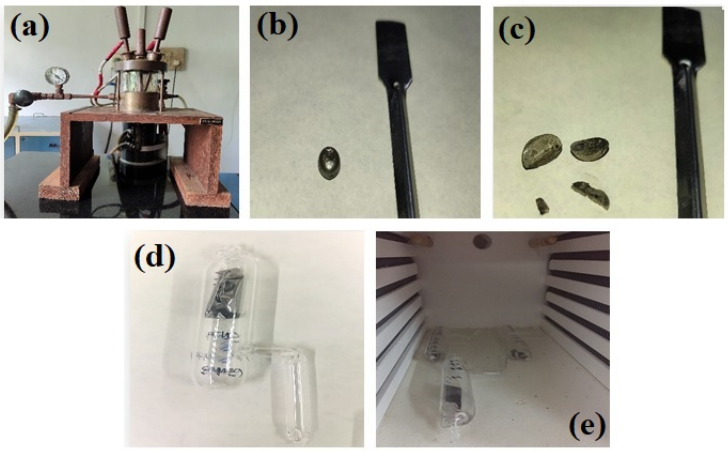

Figure 2.1: Pictures taken during the preparation of the alloy. (a) arc melting furnace, (b) arc melted alloy ingot (c) sliced ingot bead into smaller pieces (d) sample encapsulated quartz tube sealed under vacuum (e) sealed quartz tubes arranged inside the furnace.

The different types of heat treatments for the respective alloy under investigation are tabulated in Table 2.1.

Table 2.1: Various heat treatments given to the alloys under investigation. (a) RQ - rapid quenched (b) TA - temper annealed (c) HTA - high temperature (850°C) annealed (d) LTA - low temperature (400°C) annealed (e) * two halves of the same alloy ingots were subjected separately (i) rapid quenching (RQ) and (ii) temper annealing (TA). (f) # the alloy ingots were initially subjected to high-temperature annealing and subsequently to low-temperature annealing.

Series	x concentration	Code used for the type of heat treatment	Primary annealing condition			Secondary annealing condition		
			Annealing temperature in °C	Annealing time in hours	Post annealing treatment	Annealing temperature in °C	Annealing time in hours	Post annealing treatment
$Ni_{2-x}Mn_{1+x}Ga$	0, 0.25, 0.5, 0.75, 1	RQ	800	72	Rapid quenched in ice cold water			
	0.75, 1	FC	800	72	Furnace cooled			
$Ni_{2-x}Mn_{1+x}Sn$	0, 0.25, 0.5, 0.75*, 1*	RQ	800	72	Rapid quenched in ice cold water			
	0.75*, 1*	TA	800	72	⟶	427	28	Furnace cooled
$Mn_{3-x}Ni_xGa$	0#, 0.25#	HTA	850	72	Rapid quenched in ice cold water			
		LTA	⟶			400	168	Furnace cooled
$Mn_{3-x}Ni_xSn$	0, 0.25, 0.5	RQ	800	72	Rapid quenched in ice cold water			

2.3 Energy-Dispersive X-ray (EDX) spectroscopy

The quantitative elemental compositions of the synthesized alloys were determined at SPAS, Goa University, using Carl-Ziess Scanning Electron Microscope. The fundamental working principle behind EDX spectroscopy is as follows. A beam of electrons excites electrons from the inner atomic shells leaving behind the holes which are filled up by the electrons from the outer shells. The transition of the electron from the higher energy levels to the lower energy levels results in the release of energy in the form of radiation which are characteristic of atoms (elements).[1,2] The position and intensity of characteristic

emission lines help in the identification of the type and quantity of a particular element in the compound.

2.4 Structural studies

2.4.1 X-ray diffraction (XRD)

The x-ray diffraction measurements were performed using Cu-Kα radiation ($\lambda = 1.5418$ Å) at room temperature by employing the Rigaku and the Panalytical x-ray diffractometers respectively at Goa University and TIFR Mumbai. The finely powdered samples were scanned over the 2θ range from 20° to 100° at with a speed of 2°/min and a step size of 0.02°. Some of the diffraction patterns were also recorded using synchrotron radiation with $\lambda = 0.6344$ Å at BL-11 beamline, INDUS-2 synchrotron source, Indore.

X-ray diffraction (XRD) spectroscopy is one of the extensively used techniques in the field of condensed matter physics for qualitative and quantitative phase analysis of crystalline materials. Fundamentally, a crystalline solid is composed of a well-ordered array of atoms separated by a distance 'd'. The x-rays which have a wavelength of the same order as 'd', get reflected from such atomic planes. The reflected x-rays interfere constructively if the path length difference between the two reflected rays ($n\lambda = 2d\sin\theta$) is equal to nλ.[3,4] Fig. 2.2 gives the conceptual illustration of Bragg's diffraction.

X-ray diffraction data analysis

The phase formation and the purity check of the alloys were carried out by Rietveld refinement using the Fullprof suite.[5] Here an x-ray diffraction pattern is generated based on

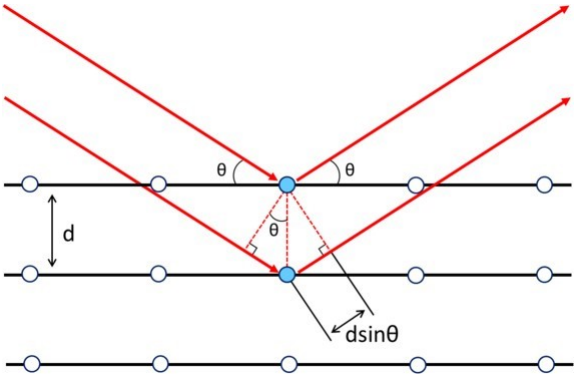

Figure 2.2: Conceptual illustration of Bragg's diffraction.

the suitable structural model and then refined iteratively to fit the experimental diffraction pattern by employing a least-square method formulated on the basis of the minimization of the residual R.[6,7] This residual R is given as a difference between the theoretically generated and experimentally obtained diffraction patterns and stated as

$$R = \sum_i w_i |y_{ip} - y_{ia}|^2$$

Here w_i is a appropriate weight given by

$$(w_i)^{-1} = \sigma_i^2 = \sigma_{in}^2 + \sigma_{im}^2$$

where the terms σ_{in} and σ_{im} individually constitute the standard deviation related to the intensity of a peak and the background (y_{ib}). y_{ia} constitute the summation of contributions from nearby Bragg's peaks. y_{ip} constitute the observed intensity in a i^{th} step. Additionally, the term y_{ia} can be estimated as

$$y_{ia} = S \sum_k M_k L_k |F_k|^2 G(\Delta\theta_{ik}) + y_{ib}$$

where S, M_k, L_k, G and F_k respectively denotes the scale factor, multiplicity aspect, Lorentz polarisation coefficient for k^{th} reflection, reflection profile function, and structure

factor. $\Delta\theta_{ik} = 2\theta_i - 2\theta_k$, $2\theta_k$ and y_{ib} displays the location of the estimated Bragg peak and the intensity of the background. The term $|F_k|$ relies on the location of every atom j inside every Miller plane,

$$F_{hkl} = \sum_j N_j f_j e^{2\pi i(hx_j + ky_j + lz_j)} e^{-B\frac{sin^2(\theta)}{\lambda^2}}$$

Here, N_j is the site occupancy, f_j is the atomic factor, and B is the factor dependent on atomic vibrations due to the temperature and x_j, y_j, z_j denote the fractional coordinates of the atom in the unit cell. The best fit is characterized by the following reliability factors:

$$R_p = \frac{\Sigma|y_{ip} - y_{ia}|}{\Sigma y_{ip}}$$

$$R_{wp} = \left[\frac{\Sigma w_i(y_{ip} - y_{ia})^2}{\Sigma w_i y_{ip}^2}\right]^{1/2}$$

$$R_{Bragg} = \frac{\Sigma|I_{ko} - I_{kc}|}{\Sigma I_{ko}}$$

$$R_{exp} = \left[\frac{(N-P)}{\Sigma w_i y_{ip}^2}\right]^{1/2}$$

$$\chi^2 = \frac{\Sigma w_i(y_{ip} - y_{ia})^2}{(N-P)}$$

Where R_p is a profile factor that is minimized at the time of data fitting, R_{wp} is a weighted profile factor, R_{Bragg} is Bragg's factor that tries to alter the R for a particular phase, R_{exp} is expected weighted profile factor that calculates the best R-value for the set of data and reduces χ^2 is the Goodness of the fit indicator.[8]

2.4.2 Neutron diffraction (ND)

The neutron diffraction patterns given in this thesis were recorded on the PD-2 diffractometer using a wavelength of ∼1.2443 Å at Dhruva rector, BARC, Mumbai. This study

was mainly carried out to understand the changes happening in the magnetic structure of the alloys as a function of temperature. The obtained neutron diffraction patterns were analyzed using Fullprof suite and Jana 2020 software.

2.4.3 X-ray Absorption Fine Structure (XAFS) spectroscopy

The XAFS measurements presented in this thesis were recorded both in transmission as well as fluorescence modes. These spectra were recorded at Mn (6539 eV), Ni (8333 eV), Ga (10367 eV), and Sn (29200 eV) K-edges using P65 beamline at PETRA III synchrotron, Hamburg, Germany.

The primary focus in an XAFS experiment is to measure the x-ray absorption coefficient 'μ' as a function of energy at and near the binding energy of an absorber atom. This physical quantity of μ is referred to as x-ray absorption probability given by Beers law, $I = I_0 e^{-\mu t}$. Here, I_0 and I are the intensity of the incident, and the transmitted x-ray photon beam, and t is the thickness of the sample. Generally, the x-ray absorption coefficient is known to vary smoothly as a function of incident energy E, given by $\mu \approx \frac{\rho Z^4}{AE^3}$. Here, Z is the atomic number, ρ is the density of the sample, and A is the atomic mass. The robust dependency of μ on both E and Z is the basic property of x-ray radiation. Fig. 2.3 (b) depicts the dependence of energy on $\frac{\mu}{\rho}$ ratio for O, Fe, Cd, and Pb. Besides, this plot shows the presence of sharp discontinuities referred to as 'absorption edges' due to the excitation of a core electron to the continuum.

Fig. 2.4 illustrates the theory behind the x-ray absorption process. Beyond the x-ray absorption edge, the incident x-ray photon energy is exploited to excite the core level

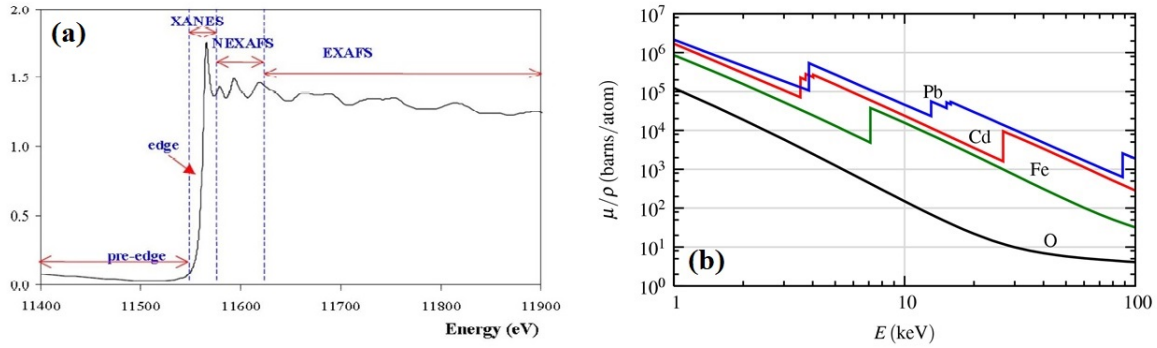

Figure 2.3: (a)Schematic representation of an XAFS spectrum, exhibiting absorption of the x-rays both within the 50 eV of the edge energy (XANES) and from some hundred to greater than 1000 eV energy beyond the absorption edge (EXAFS).(b) X-ray absorption cross-section $\frac{\mu}{\rho}$ for various elements in the range from 1 to 100 keV.

electron to the continuum, and any surplus energy is transferred to the photoelectron in the form of kinetic energy(see Fig. 2.4 (a)).

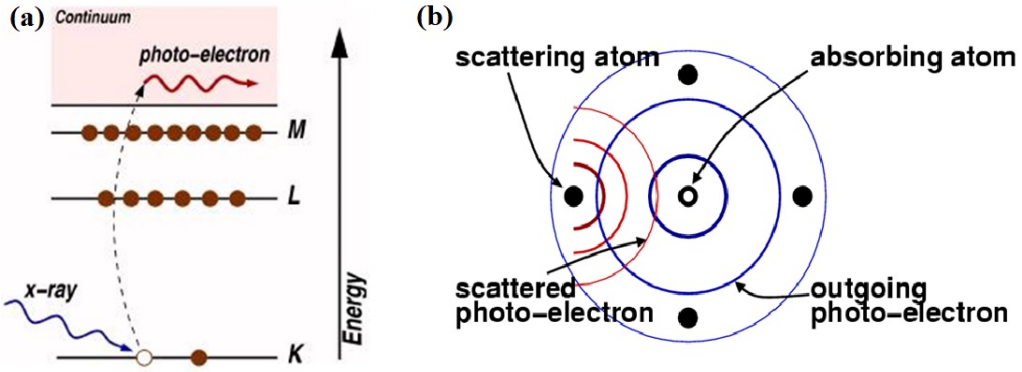

Figure 2.4: (a) The photoelectric effect wherein the x-rays are absorbed and a core-shell electron is excited out from the atom. (b) The interaction between the photoelectron spherical waves traveling away from the absorber atom and the backscattered spherical waves at the absorber atom.

The generated photoelectron can be represented in the form of a spherical wave traveling away from the absorber atom (see Fig. 2.4 (b)). These outgoing photoelectron waves get backscattered from the surrounding atoms in the solid or condensed matter. The relative phase difference between the outgoing photoelectron wave and the backscattered

spherical wave at the absorber atom influences the absorption coefficient giving rise to modulations in its value, which is called XAFS.

XAFS spectrum is classified into two parts: X-ray Absorption Near Edge Structure (XANES) spectra and Extended X-ray Absorption Fine Structure (EXAFS) spectra. Although both these sections have a common physical origin, the above classification makes the evaluation of the XAFS spectra simpler. Here, while the XANES is used for studying the coordination chemistry and the formal oxidation state of an absorber atom, the EXAFS is employed for finding the coordination number, bond distances, and neighboring environment of an absorber atom.[9] These sections of the XAFS spectra are clearly depicted in Fig. 2.3 (a).

The EAXFS spectrum is defined using an equation $\chi(E)$. This equation is written in terms of the summation of the contribution from each scattering path of photoelectron, as stated below.[10,11]

$$\chi(k) = \sum_i \chi_i(k)$$

Each photoelectron scattering path takes the form:

$$\chi_i(k) = \frac{(N_i S_0^2) F_{eff_i}(k)}{kR_i^2} \sin\left[2kR_i + \varphi_i(k)\right] e^{-2\sigma_i^2 k^2} e^{\frac{-2R_i}{\lambda(k)}}$$

where, $R_i = R_{0i} + \Delta R_i$ and $k^2 = \frac{2m_e(E - E_0 + \Delta E_0)}{\hbar}$

Here, the terms $F_{eff_i}(k)$, $\varphi_i(k)$, and $\lambda(k)$ respectively denotes the photoelectron effective scattering amplitude, photoelectron phase shift, and the photoelectron mean free path. R_i is the photoelectron half-path length, R_{0i} is the theoretically calculated half-path

length based on the predetermined structural model, and ΔR_i is the difference between the experimentally measured and the theoretically calculated photoelectron half path length. N_i gives the number of scattering atoms of i^{th} type. S_0^2 is the amplitude reduced factor. The term $e^{-2\sigma_i^2 k^2}$ describe the disorder in the atomic position. Further, the term $e^{\frac{-2R_i}{\lambda(k)}}$ is a damping factor, which accounts for the certainty that, over a short distance the photoelectron wave can only be scattered elastically.

Experimental Setup

The XAFS experiment can be performed both in the transmission and the fluorescence mode. Fig. 2.5 illustrates the schematic of the XAFS experimental set-up both for transmission and fluorescence geometries.

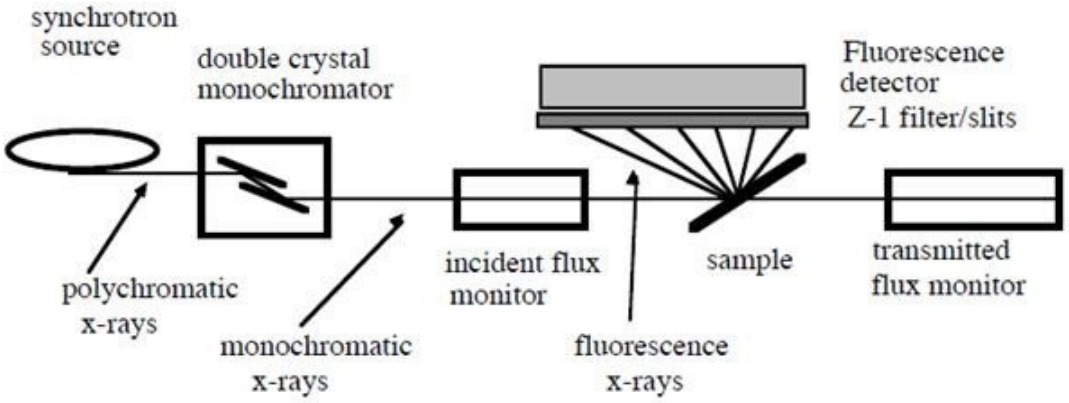

Figure 2.5: The schematic of the XAFS experimental set-up for transmission and fluorescence geometries.

The main components of the EXAFS experimental setup are the monochromator, slits, and ion chambers. The monochromator is utilized to choose the x-ray energy of interest. A monochromator is made up of a pair of silicon crystals arranged parallel to one another. Particularly, only those wavelengths of x-ray photons that satisfy Bragg's

condition ($n\lambda = 2d\sin\theta$) at a chosen angle 'θ' get reflected from the surface of the first crystal. The second crystal acts like a mirror, which is used to put the beam back on its original path. However, in addition to the primary energy, the monochromator crystals sometimes can allow the harmonics of higher order to pass through the experimental beam. This is fixed by detuning the crystals with respect to each other. The higher order harmonics rejection can also be achieved by employing the x-ray mirrors made of metals having higher atomic numbers like Rh or Pt. The gas ionization chambers are used to record the intensities of the incident and the transmitted x-ray fluxes. Primarily, the ion chambers comprise parallel plate capacitors. Across these plates, a high voltage is maintained, and the space between the plates is filled up with gas. When a beam of x-rays travels across the chamber, it ionizes the gas and produces electrons that are swept by the applied potential producing a current that is proportional to the intensity of x-rays. The choice of the gas or the mixture of gases that fills the chambers is dependent on the edge energy.

XAFS data reduction, modeling, and analysis

The recorded XAFS data were analyzed using Demeter suite software which is comprised of ATHENA and ARTEMIS.[12,13] Here, the data reduction was carried out using the ATHENA software. The reduction starts by converting the measured intensities to the x-ray absorption coefficient function $\mu(E)$, followed by subtracting a pre-edge background from $\mu(E)$. The absorption edge energy E_0 is subsequently recognized as the maxima of the derivative of $\mu(E)$. Additionally, the post-edge background function is subtracted and

$\mu_0(E)$ is estimated. $\chi(k)$ is then extracted using the formula

$$\chi_i(k) = \frac{(N_i S_0^2) F_{eff_i}(k)}{kR_i^2} \sin\left[2kR_i + \varphi_i(k)\right] e^{-2\sigma_i^2 k^2} e^{\frac{-2R_i}{\lambda(k)}}$$

While modeling the EXAFS data, one should have an idea about the structural model that will be employed for fitting the $\chi(k)$ data. One needs to estimate the number of parameters that can be varied, which should be less than the number of degrees of freedom available from the fitting ranges in k-space and R-space given by

$$N \approx \frac{2\Delta k \Delta R}{\pi}$$

Here ΔR and Δk respectively are the R-space and k-space ranges used for fitting. Typically, the chosen ranges are R = [1.0, 3.0] Å and k = [3.0, 12.0] Å^{-1}. In this case, $N \approx$ becomes 11.5. Thus, for the given range of 'R' and 'k', there can be about 11 parameters that can be determined from the EXAFS data fitting. Generally, each coordination corresponds to three fitting parameters, i.e., N, R, and σ^2. The total number of fitting parameters can be controlled by constraining the parameters such as N, R, and σ^2 for different paths while fitting a single edge or even while fitting multiple edges recorded at different temperatures or for elements. Besides, fitting together more than one EXAFS edge to a common structural model can be advantageous in ascertaining the local structural disorder around the absorber atom in a system. The EXAFS data modeling was done using ARTEMIS. The theoretical standards for each scattering path were calculated using FEFF6.0.[12–14]

2.5 Magnetization measurements

The magnetization measurements were performed using the SQUID and the VSM magnetometer, respectively, at University Laboratory for Materials Characterization, Goa University, TIFR, Mumbai, and UGC-DAE Mumbai centre. The magnetization as a function of temperature was recorded in ZFC, FCC, and FCW modes in an applied field of 100 Oe in the temperature range from 2 K to 390 K. During this measurement, the sample was cooled from 300 K down to the lowest temperature (3 K) in zero fields, after which the field was applied and the magnetization was measured during warming (ZFC) and subsequent cooling (FCC) and warming (FCW) cycles. In addition, the magnetization as a function of an applied magnetic field was measured at several predetermined temperatures in the applied field of ± 9 T/± 7 T. The details about the SQUID and VSM magnetometers and their respective working principle are given below.

2.5.1 Superconducting Quantum Interference Device (SQUID) magnetometer

Fundamentally, the SQUID sensor is a flux to voltage transducer.[15] It is highly sensitive and provides a broad operational bandwidth, nearly from DC to a few GHz. A DC SQUID sensor comprises two superconducting half rings connected by a thin insulating layer, creating two Josephson junction, which is in parallel, as shown in Fig. 2.6 (a). The working of DC SQUID sensor depends on the phenomena of Josephson Effect[16] and flux quantization.[17]

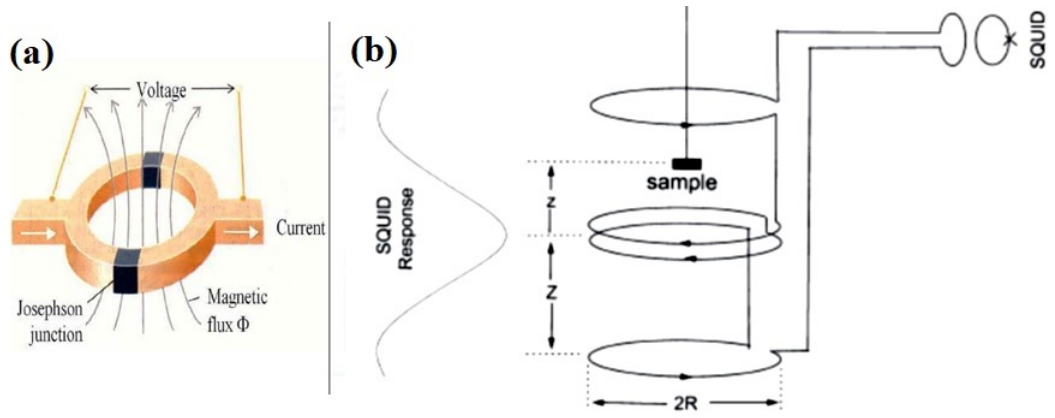

Figure 2.6: (a) Schematic illustration of a DC SQUID sensor, (b) schematic representation of Superconducting Quantum Interference Device (SQUID) magnetometer.

2.5.2 Vibrating sample magnetometer (VSM)

The working of the Vibrating Sample Magnetometer is based on the Faraday′s Law, which says that when the magnetic flux associated with the electric circuit is varied, an e.m.f is produced in the circuit. To measure the magnetization of the sample using VSM, it is mounted on the sample holder which is placed in an externally applied magnetic field. Eventually, the sample slowly gets magnetized as a result of the orientation of its magnetic moments. This magnetized sample generates a magnetic field of its own referred to as the stray field. Next, the sample is subjected to vibrations by moving up and down. As a result of these vibrations, its stray field begins to vary accordingly as a function of time. Because of this varying magnetic stray field, the voltage gets induced in the pick-up coils of the magnetometer linked with the stray field. The voltage generated in the linked pick-up coil changes in proportion to the magnetization of the sample.

2.6 Transport properties

2.6.1 Electrical resistivity

The resistivity measurements were performed at the School of Physical and Applied Science, Goa University, using the experimental setup consisting of a four-probe arrangement on a close cycle refrigerator wired to a Keithley 6221 DC, and AC current source, Keithley 2182A nanovoltmeter, and Lakeshore 325 temperature controller. This setup can measure the resistance of the sample in the temperature range from 15 K to 450 K. The setup is automatically controlled using Labview. The four-probe arrangement employed is shown in Fig. 2.7. Typically, this arrangement consists of four probes aligned in a straight line, wherein the constant current I is flown through the outer two probes, and the corresponding voltage drop V is measured across the inner two probes.[18] In our setup, the four-probe arrangement is fixated on the cold head of CCR using G-varnish. The sample whose resistivity has to be measured is cut in the form of a thin rectangular piece and mounted on top of four probes arrangement. The contact between the probes and the sample is made using silver paint.

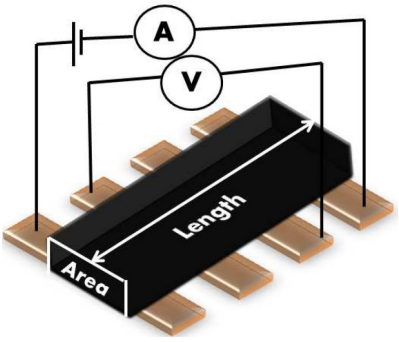

Figure 2.7: Schematic illustration of the four probe setup used for the resistivity measurement.

The resistivity of the sample is calculated using the expression $\rho = R\frac{A}{l}$, where ρ refers to resistivity, R refers to resistance, A refers to sample cross-sectional area, and l refers to the length of the sample.

2.6.2 Hall resistivity

Hall Theory

The Hall measurements as a function of temperature and the applied magnetic field presented in this thesis were carried out at TIFR, Mumbai, using the four-wire configuration as shown in Fig. 2.8 (a). The phenomenon of the Hall effect states that when a conductor carrying a current is laid down in a magnetic field perpendicular to the direction of current flow, the electric field gets generated along the direction that is perpendicular to both, the direction of the flow of the current and the applied magnetic field.

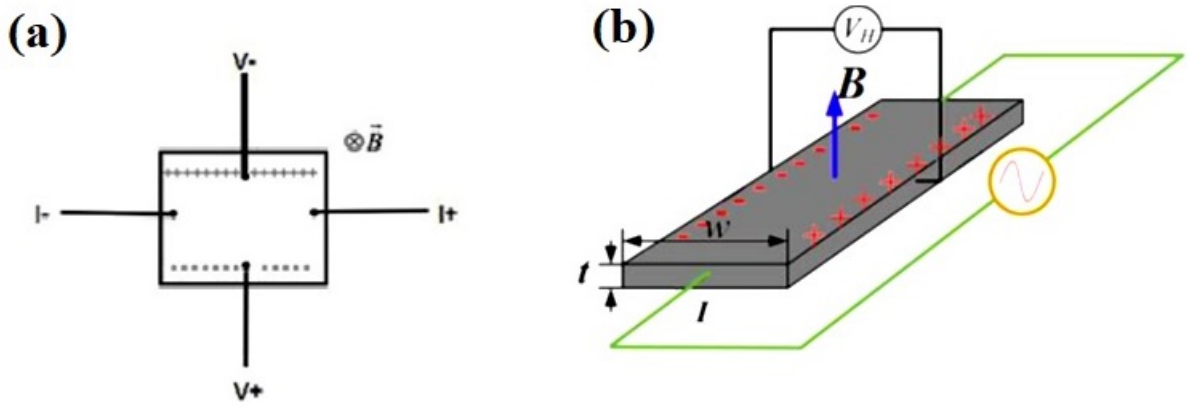

Figure 2.8: (a) The representation of the four-wire configuration employed in Hall resistivity measurement. (b) The schematic illustration of the geometry of the Hall experiment.

Here, the generated field is referred to as the Hall field. Fig. 2.8 (b) conceptualize the phenomenon of the Hall effect. The Hall coefficient (R_H) is given by $R_H = \frac{E_y}{j_x B_z}$ where E_y

is the transverse electric field, j_x is the current density, B is the applied magnetic field. The R_H in terms of n and q can be written as $R_H = -\frac{1}{nq}$, where n is the carrier charge concentration, and q is the charge.

References

[1] J. I. Goldstein. *Scanning Electron Microscopy and X-ray Microanalysis: Third Edition.* 2003.

[2] G. F. Harrington and J. Santiso. *Journal of Electroceramics*, 47(4):141–163, 2021.

[3] B. D. Cullity. *Elements of X-ray Diffraction.* Addison Wesley Publishing Co. USA, 1956.

[4] A. J. Dekker. *Inc. New York*, 1957.

[5] J. Rodríguez-Carvajal and T. Roisnel. *Physica B*, 192:55–69, 1993.

[6] H. M. Rietveld. *Acta Crystallographica*, 22(1):151–152, 1967.

[7] H. M. Rietveld. *Journal of Applied Crystallography*, 2(2):65–71, 1969.

[8] R. A. Young and P. Paufler. *Crystal Research and Technology*, 30(4):494–494, 1995.

[9] G. G. Li, F. Bridges, and C. H. Booth. *Physical Review B*, 52(9):6332, 1995.

[10] E. A. Stern. *Contemporary Physics*, 19(4):289–310, 1978.

[11] E. A. Stern and S. M. Heald. *Review of Scientific Instruments*, 50(12):1579–1582, 1979.

[12] B. Ravel and M. Newville. *Journal of Synchrotron Radiation*, 12(4):537–541, 2005.

[13] B. Ravel. *Journal of Synchrotron Radiation*, 8(2):314–316, 2001.

[14] J. J. Ankudinov A. Albers R. C. Zabinsky, S. I. Rehr and M. J. Eller. *Physical Review B*, 52(4):2995, 1995.

[15] C. Granata and A. Vettoliere. *Physics Reports*, 614:1–69, 2016.

[16] B. D. Josephson. *Advances in Physics*, 14:419, 1962.

[17] E. Del Giudice, C. Smith, and G. Vitiello. *Physica Scripta*, 40:786–791, 1989.

[18] L. J. Van der Pauw. *Philips Research Reports*, 16:187–195, 1961.

Chapter 3

Role of antisite disorder in the martensitic transition of $Ni_{2-x}Mn_{1+x}Ga$.

3.1 Introduction

Mn_2NiGa has attracted attention due to its high ferrimagnetic ordering temperature, T_C = 588 K, and a martensitic transformation at $T_M \approx 270$ K. It presents a large ($\sim 4\%$) magnetic field induced strain (MFIS) caused by a rearrangement of martensitic twins in the presence of the magnetic field[1] and a large inverse magnetocaloric effect.[2] Further, a spin-valve like magnetoresistance is noted at room temperature due to the formation of ferromagnetic nanoclusters in bulk lattice as a result of site occupancy disorder.[3] Antisite disorder in stoichiometric and off-stoichiometric Mn_2NiGa is also believed to be responsible for positive exchange bias which is critical for building nanodevices based on shape memory alloys.[4]

Mn_2NiGa is reported to crystallize in the so-called $L2_1B$ or the inverse Heusler structure (XX'YZ)in the austenitic phase. Here, the Y (0,0,0) and Z ($\frac{1}{2}$, $\frac{1}{2}$, $\frac{1}{2}$) sites are occupied by Mn and Ga respectively and the X ($\frac{1}{4}$, $\frac{1}{4}$, $\frac{1}{4}$) and X' ($\frac{3}{4}$, $\frac{3}{4}$, $\frac{3}{4}$) occupied by Ni and Mn

atoms with equal probability.[5] However, ab initio calculations have not been able to satisfactorily calculate the properties of Mn_2NiGa using this structure and have used alternate Hg_2CuTi structure.[6,7] The main reason for this failure of theoretical calculations is the presence of antisite disorder in these Mn-rich alloy compositions. In fact, first principle calculations incorporating antisite disorder have indicated significantly large magnetic moments in the high-temperature phase of Mn_2NiGa.[8]

Ni_2MnGa, on the other hand, has well ordered $L2_1$ face centred cubic austenitic structure and a ferromagnetic ordering temperature ~ 370 K.[9] It transforms from the austenitic state to an incommensurate 5M modulated orthorhombic structure at $T_M \approx 220$ K.[10] The transformation temperature, crystal structure, as well as properties of the Ni-Mn-Ga alloys, are sensitively dependent on the average valence electron per atom (e/a) ratio.[11] The martensitic structure changes to commensurate 5M for $Ni_{1.95}Mn_{1.19}Ga_{0.86}$ to incommensurate 7M in $Ni_{2.15}Mn_{0.85}Ga$.[12,13] Electronic structure calculations and extended x-ray absorption fine structure (EXAFS) studies highlight the importance of Ni $3d$ and Ga $4p$ hybrid states at the Fermi level in the martensitic state.[14,15] The hybridization strengthens with the increasing e/a ratio and leads to a proportionate increase in the martensitic transformation temperature from 220 K in Ni_2MnGa to well above the room temperature and even past its T_C.

The e/a ratio for the stoichiometric Ni_2MnGa alloy is 7.5 and can be increased by substituting Ni in place of Mn or Ga or both or by favorably altering the ratio of Mn to Ga. A strong correlation is observed between T_M and the e/a ratio and gives an

impression of the e/a ratio being the sole controlling factor of martensitic transformation temperature in Ni-Mn-Ga alloys.[11] However, some prominent exceptions to this so-called e/a rule exist and are related to the inverse Heusler alloy, Mn_2NiGa.[1,16] Though the e/a ratio of Mn_2NiGa is less than that of Ni_2MnGa, it undergoes a martensitic transformation at a temperature ($T_M = 270$ K) higher than that of Ni_2MnGa.

The martensitic structure of Mn_2NiGa is also controversial. While the first report indicated the martensitic structure to be non-modulated tetragonal,[17] the subsequent neutron diffraction studies reported the martensitic structure as seven-fold modulated orthorhombic.[5] Modulated structures realize due to the periodic displacement of atoms from the crystallographic positions in a tetragonal lattice. These modulated structures help in lowering hysteresis losses and actuation fields leading to a better functionality of the Heusler alloy. Therefore, the observation of modulated structure in Mn_2NiGa increases its applicability considering its high magnetic ordering temperature and high martensitic transformation temperature. Theoretical calculations have also concurred with the experimental observations of modulated structures in the martensitic state.[18] Powder x-ray diffraction studies on Mn_2NiGa established a relation between the martensitic structure and the residual stress.[19] With increasing stress, the martensitic structure was shown to change from 7M monoclinic to tetragonal. These studies also showed the existence of the martensitic phase at room temperature which was above the transformation temperature of the alloy. The presence of the additional phase was also confirmed from neutron diffraction studies and it was shown to be present at all temperatures in the austenitic

state.[5] Microstructure studies also reported the presence of additional structural phases. In addition, a minor fraction of the martensitic phase was seen well above the transition temperature in both, the stoichiometric and off-stoichiometric Mn_2NiGa. These additional precipitates were identified as Mn-rich phases and were reported to disappear after annealing at 1123 K for 24 h.[20]

The existence of modulated phases well above the martensitic transition temperature of Mn_2NiGa is quite interesting and needs to be understood. Recently, it has been shown that a similar alloy, Mn_2NiSn, phase separates upon temper annealing into Ni_2MnSn type Heusler and Mn_3Sn type $D0_{19}$ phases.[21] Similar phase segregation has been reported in several other Mn-rich Heusler alloys of the type $Ni_{50}Mn_{50-y}Z_y$ (Z = Ga, Sn, In, Sb)[22] EXAFS investigations on as-prepared and temper annealed $Ni_{50}Mn_{50-y}In_y$ alloys revealed existence of local phase separation of Heulser and $L1_0$ phases in all off-stoichiometric as-prepared compositions.[23] Such local phase separation is caused due to the stress caused by size difference between Mn and the substituted In atoms in $Ni_{50}Mn_{50-y}In_y$. Therefore, the presence of the modulated phases in Mn_2NiGa could also be stress-related. A question then arises if the stress-affected structural correlations in Mn_2NiGa are responsible for the appearance of martensitic transformation at a higher temperature as compared to Ni_2MnGa by violating the so-called e/a rule. To seek answers to this question, we report studies on $Ni_{2-x}Mn_{1+x}Ga$ with $0 \leq x \leq 1$. The $L2_1$ structure (X_2YZ) of Ni_2MnGa consists of 8 Ni atoms occupying the X sites, 4 Mn atoms at the Y sites, and 4 Ga atoms at the Z sites. The values of $x = 0$, 0.25, 0.5, 0.75, and 1 are so chosen to represent an

incremental replacement of one Ni atom at a time and realize in Mn_2NiGa ($x = 1$). We also investigate the effect of different annealing treatments, rapid quenching (RQ) versus furnace cooling (FC), on the martensitic properties of these Mn-rich alloys.

3.2 Results

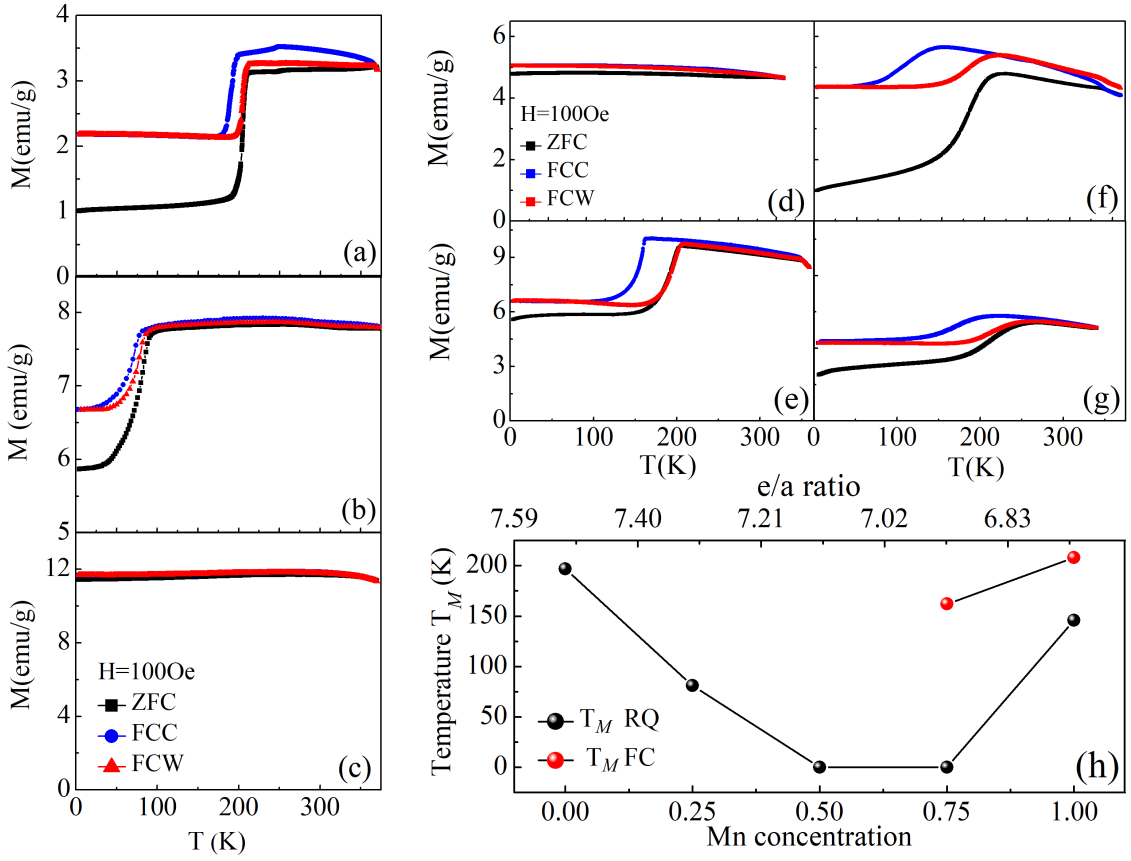

Figure 3.1: (a–g) Plots of magnetization as a function of temperature measured in 100 Oe field during ZFC, FCC, and FCW cycles for the RQ and the FC alloys of composition $Ni_{2-x}Mn_{1+x}Ga$. (h) Variation of T_M as a function of x and e/a ratio in $Ni_{2-x}Mn_{1+x}Ga$.

In $Ni_{2-x}Mn_{1+x}Ga$, as the ratio of Ni to Mn changes from 2:1 ($x = 0$) to 1:2 ($x = 1$), the e/a ratio decreases linearly from 7.5 to 6.75. Ordinarily, this decrease in the e/a ratio should have resulted in a decrease in T_M. However, after the initial decrease of T_M

from about 200 K for Ni_2MnGa to about 30 K in alloy with $x = 0.5$, T_M again rises to 270 K in $NiMn_2Ga$.[1] To ascertain this behaviour of T_M in the present set of alloys, magnetization as a function of temperature, M(T) was recorded during the ZFC, FCC, and FCW cycles in a field of 100 Oe. During this measurement, samples were cooled from 300 K down to the lowest temperature (3 K) in zero field, after which the field was applied and magnetization was measured during warming (ZFC) and subsequent cooling (FCC) and warming (FCW) cycles. The M(T) curves for RQ and FC $Ni_{2-x}Mn_{1+x}Ga$ (x = 0, 0.25, 0.5, 0.75 and 1) alloys, in the temperature interval 3 K $\leq$ T $\leq$ 325 K, are presented in Fig. 3.1 (a – g). In the case of Ni_2MnGa ($x = 0$), magnetization recorded during the warming cycles (ZFC and FCW) displays a sharp decrease at 197 K and is termed as the martensitic start temperature $M_s = T_M$ (see Fig. 3.1 (a)). The hysteresis in the transformation temperature during the warming and cooling (FCC) magnetization cycles confirms the first-order nature of the transition. Isothermal magnetization (not shown) recorded at 300 K confirms the ferromagnetic nature of the alloy which is in confirmation that the T_C of Ni_2MnGa is about 370 K. A similar behaviour is noted in the alloy with $x = 0.25$ with T_M at 81 K and T_C above 300 K (Fig. 3.1 (b)). The RQ alloys with x= 0.5 and 0.75 display ferromagnetic nature and nearly invariant magnetization in the temperature interval of 3 K – 325 K (Fig. 3.1 (c) and (d)) implying the absence of martensitic transformation in these alloys. Martensitic transition reappears with further increase in x to 1 with $T_M = 162$ K (Fig. 3.1 (f)). There is also a difference in the ZFC and FCC/FCW magnetization below martensitic transition temperature. This difference

in the magnetization values could be ascribed to antisite disorder which can result in Mn–Mn antiferromagnetic interactions[19,24] Though the transformation temperatures reported here are quite different from those observed earlier,[1] the variation of T_M as a function of increasing Mn concentration is similar to that observed earlier.[1] The difference in temperatures could be due to different annealing heat treatments given to the alloys. Further, furnace cooling the alloys after annealing results in the appearance of martensitic transformation in the alloy with $x = 0.75$ (Fig. 3.1 (e)) and an increase in T_M to 209 K in $x = 1$ (Fig. 3.1(g)). Furnace cooling of $x = 0.5$ did not result in any change in the observed characteristic of the RQ alloy. The values of T_M along with the elemental compositions obtained from EDX and the lattice constants of the cubic Heusler phase of the alloys are listed in Table 3.1. Fig. 3.1 (h) displays a variation of T_M as a function of the excess Mn concentration, x, and the e/a ratio. The variation is qualitatively similar to the one obtained earlier.[1] In particular, it displays an increase in T_M as the e/a ratio decreases from 6.9 to 6.75 (x increases from 0.75 to 1) in both RQ and FC alloys. Besides, Fig. 3.2 displays microstructures of five alloy compositions of the series $Ni_{2-x}Mn_{1+x}Ga$ with $x = 0$, 0.75 and 1.0 (RQ) and $x = 0.75$ and 1.0 (FC).

Fig. 3.3 shows the XRD patterns for RQ $Ni_{2-x}Mn_{1+x}Ga$ ($x = 0$, 0.25, 0.5, 0.75 and 1.0) and FC $x = 0.75$ and 1.0 alloys that were recorded at room temperature. All the diffraction peaks can be indexed to face-centred cubic $L2_1$ crystal structure with no detectable impurities. Weak impurity phases, in addition to the cubic Heusler phase, are visible in the diffraction patterns of both RQ and FC alloys with $x = 0.75$ and 1. The

Table 3.1: e/a ratio calculated from the nominal composition, EDX composition, lattice parameter, a estimated from Rietveld refinement of the XRD patterns (errors in the last digit are given in parenthesis), and the martensitic start temperature, T_M for $Ni_{2-x}Mn_{1+x}Ga$ series

Alloy	e/a ratio	EDX composition	a Å	T_M (K)
Ni_2MnGa RQ	7.5	$Ni_{2.03}Mn_{1.01}Ga_{0.97}$	5.8240(3)	197
$Ni_{1.75}Mn_{1.25}Ga$ RQ	7.31	$Ni_{1.8}Mn_{1.24}Ga_{0.96}$	5.8456(4)	81
$Ni_{1.5}Mn_{1.5}Ga$ RQ	7.13	$Ni_{1.49}Mn_{1.53}Ga_{0.98}$	5.8624(2)	NM
$Ni_{1.25}Mn_{1.75}Ga$ RQ	6.94	$Ni_{1.24}Mn_{1.8}Ga_{0.96}$	5.8818(3)	NM
$Ni_{1.25}Mn_{1.75}Ga$ FC		$Ni_{1.24}Mn_{1.79}Ga_{0.98}$	5.8824(5)	162
$NiMn_2Ga$ RQ	6.75	$Ni_{1.05}Mn_{1.90}Ga_{1.05}$	5.9052(4)	146
$NiMn_2Ga$ FC		$Ni_{0.88}Mn_{2.14}Ga_{0.98}$	5.9022(5)	208

intensities of the impurity peaks appear to grow with increasing x and with the changes in heat treatment. Such impurity phases have been observed earlier and have been linked to the presence of residual stress in the alloys.[19] Le Bail refinement of the diffraction patterns, presented in Fig. 3.4, helped in confirming the major structural phase to be $L2_1$ cubic and the impurity peaks seen in $x = 0.75$ and 1 alloys to belong to a 7M monoclinic phase in agreement with literature reports.[19] The cell constants of the cubic $L2_1$ cell were calculated (see Table 3.1) and also found to be in close agreement with literature values.[1,12,15]

Could the presence of impurity phases have any role to play in the behaviour of T_M as a function of the e/a ratio? To further investigate this aspect, EXAFS was recorded at 300 K and 30 K at the Ni, Mn, and Ga K edges to study the changes in the local structure of these constituent atoms in their austenitic and martensitic phases. EXAFS data in the k range of 3 Å^{-1} to 14 Å^{-1} and R range of 1 Å to 3 Å, at all the three edges were fitted together with a common structural model used earlier in Ref.[15] Fitting

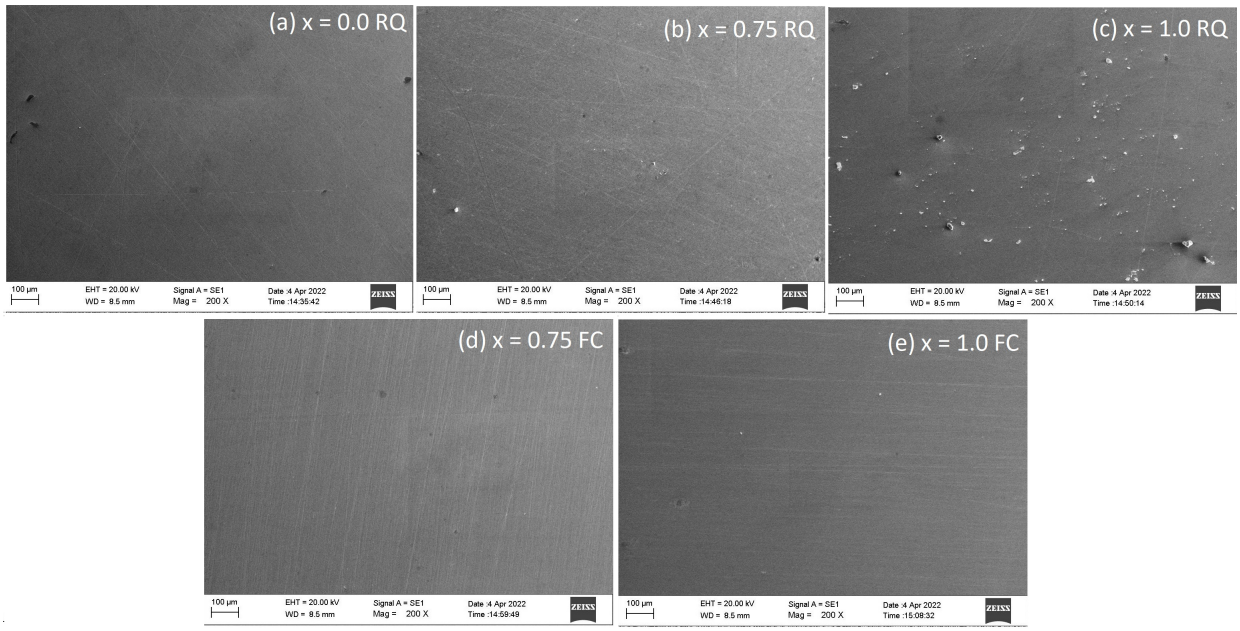

Figure 3.2: SEM micrographs for $Ni_{2-x}Mn_{1+x}Ga$ with $x = 0$, 0.75 and 1.0 (RQ series) and $x = 0.75$ and 1.0 (FC series)

EXAFS data at all three edges together not only reduces the number of free parameters but also increases the reliability in obtained values of bond distances. The fit consists of four correlations, the nearest neighbor Ni–Mn and Ni–Ga, and the next nearest neighbor Ni–Ni and Mn–Ga. A fit procedure designed to include the structural constraints yielded good fits to all three data sets in Ni_2MnGa ($x = 0$). Figs. 3.5 and 3.6 display Fourier Transform magnitude of the k^3 weighted $\chi(k)$ spectra recorded at the Ni, Mn, and Ga edges respectively for all the $Ni_{2-x}Mn_{1+x}Ga$ RQ and FC alloys.

The increase in the value of x implies progressive occupation of the Ni sites by Mn. This results in three new correlations, Mn_X–Mn, Mn_X–Ga, and Mn_X–Ni (Mn_X corresponds to Mn occupying the X sublattice of X_2YZ Heusler structure). In $Ni_{1.75}Mn_{1.25}Ga$ ($x = 0.25$) however, the data at all three edges could be fitted without including any of the

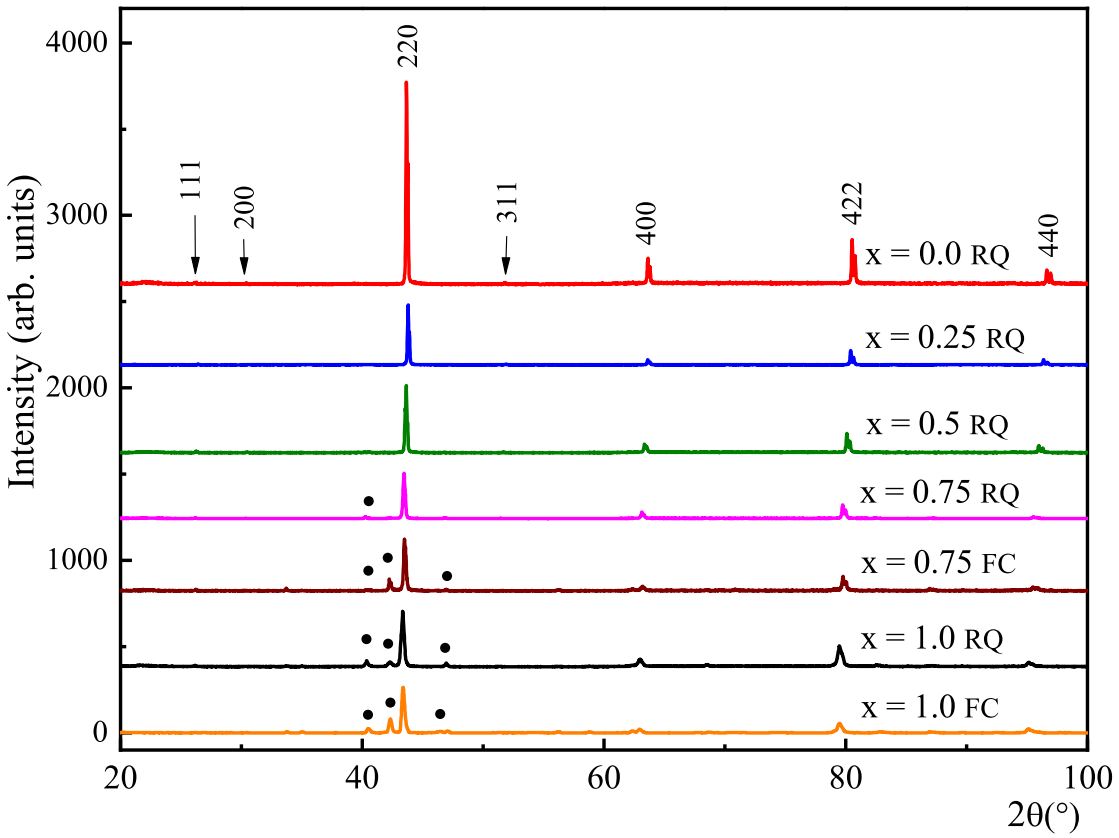

Figure 3.3: XRD patterns of RQ $Ni_{(2-x)}Mn_{(1+x)}Ga$ (x = 0, 0.25, 0.5, 0.75 and 1.0) and FC x = 0.75 and 1.0 samples recorded at room temperature. The black dots indicate the presence of impurity phases.

three new correlations. Since the electronic density differences between Mn (Z = 25), Ni (Z = 28), and Ga (Z = 31) are within $\Delta Z = \pm 5$, it would be difficult to distinguish between them as scatterers at the same distance. But to get a good fit, the structural constraints imposed by the $L2_1$ structure had to be relaxed. This is evident from the values of bond distances listed in Table 3.2 where Ni–Mn and Ni–Ga distances are not equal. This difference in nearest neighbour distances could be due to structural strain caused by the Mn atom occupying Ni (X) sites.

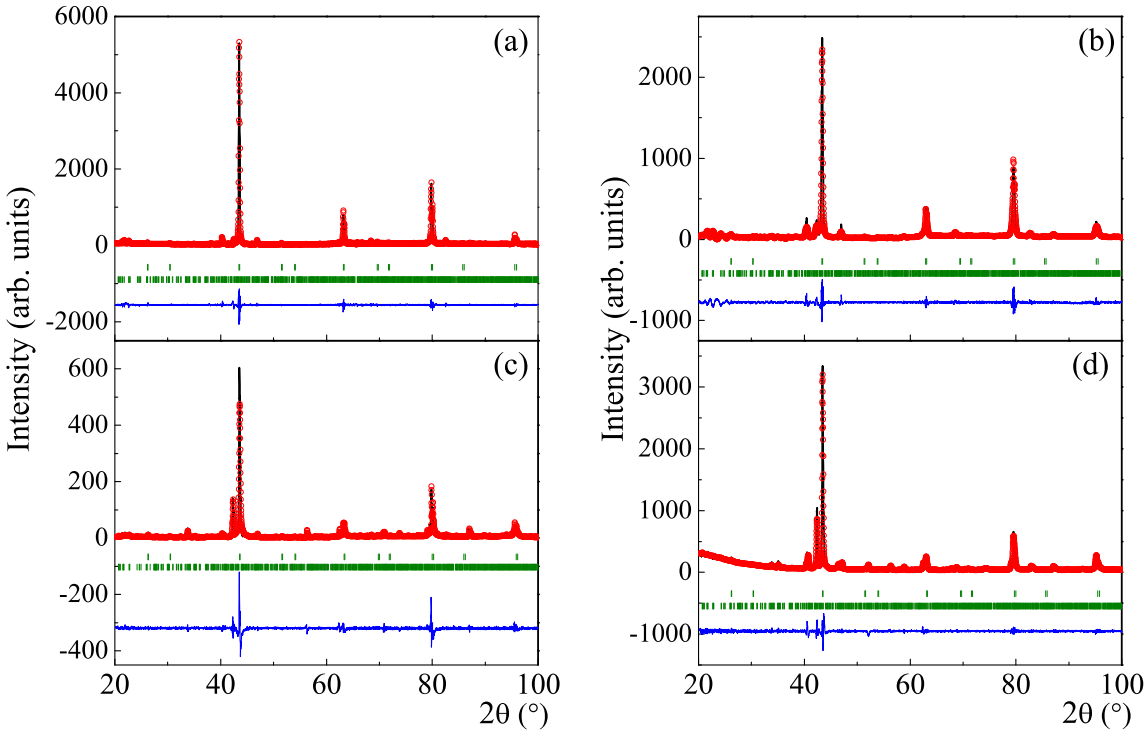

Figure 3.4: Le Bail refined laboratory x-ray diffraction patterns of $Ni_{1.25}Mn_{1.75}Ga$ (a) RQ and (c) FC and $NiMn_2Ga$ (b) RQ and (d) FC alloys.

With a further increase in x, the effect of Mn substitution became even more evident. In x= 0.5 the Mn and Ga EXAFS data could not be fitted with the above structural model even though its crystal structure is cubic. The Mn_X–Mn correlation had to be included in the fitting procedure but its bond distance was found to be $\sim$ 2.76 Å which is larger than the expected value of about 2.52 Å. For higher values of x= 0.75 and 1, both Mn_X–Mn and Mn_X–Ga correlations had to be included in the fitting procedure to obtain good fits. The bond distances of both these correlations (see Table 3.2) were larger than their expected values pointing to the segregation of structural defects rich in Mn. Further

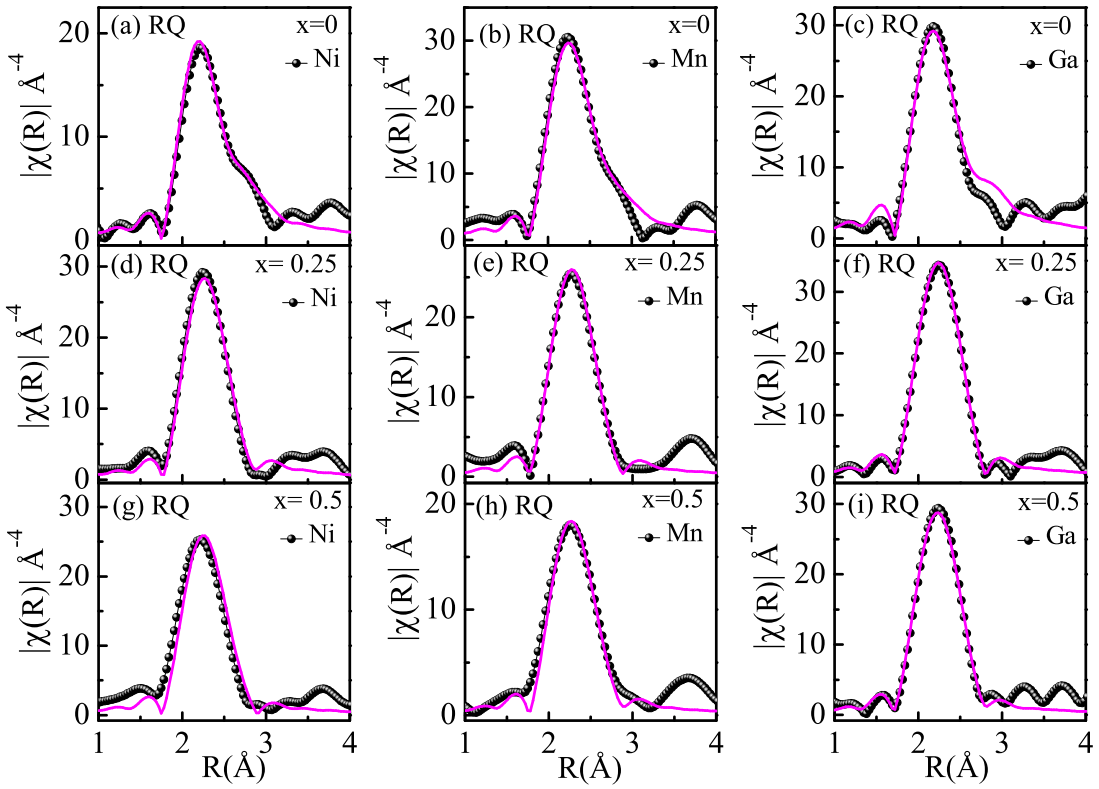

Figure 3.5: FT magnitudes of k^3 weighted EXAFS measured at 300 K at the Ni, Mn, and Ga K edges in Ni_2MnGa, $Ni_{1.75}Mn_{1.25}Ga$ and $Ni_{1.5}Mn_{1.5}Ga$ RQ alloys.

support for the segregation of structural defects comes from a consistent decrease in the amplitude of Ni, Mn, and Ga EXAFS oscillations (see Fig. 3.7, 3.8, 3.9), with an increase in x. Such a decrease in EXAFS amplitude could be ascribed to an out of phase addition of contributions to the EXAFS signal from the defect phase and the Heusler phase. The presence of a defect phase rich in Mn is also supported by the observation of Mn-rich precipitates in the polycrystalline alloys of $Mn_{2+x}NiGa_{1-x}$.[20] The defects, however, do not seem to be responsible for the absence of martensitic transition in $x = 0.5$ and 0.75

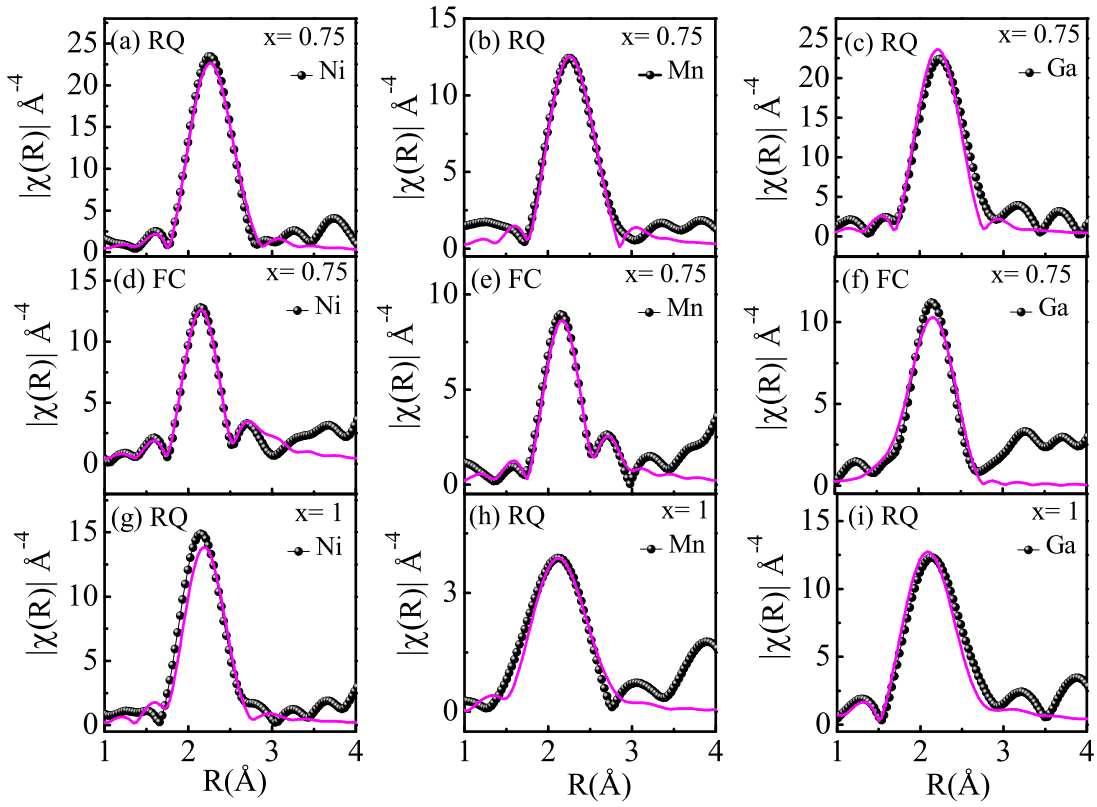

Figure 3.6: The magnitude of Fourier transform of k^3 weighted Ni, Mn and Ga K edge EXAFS recorded at 300 K in RQ and FC alloy compositions, $Ni_{1.25}Mn_{1.75}Ga$ and RQ $NiMn_2Ga$.

as they are also present in the martensitic alloys, $x = 1$ (RQ) and $x = 0.75$ (FC).

The previous structural studies reporting impurity phases in Mn_2NiGa alloys have suggested them to be modulated 5M or 7M phases arising most probably due to residual stress.[5,19] However, such modulated structures do not account for the nearest neighbour distances of about 2.7 to 2.8 Å.[12] The other Mn-rich defect phase possible is Mn_3Ga. Both the tetragonal and cubic phases of Mn_3Ga consist of nearest neighbour Mn–Mn and Mn–Ga bonds at 2.7 and 2.8 Å. To explore the possibility of the existence of Mn_3Ga

Table 3.2: Near neighbour bond distances (R) and the mean-square disorder in the bond length (σ^2) obtained by simultaneous fitting of 300 K Ni, Mn, and Ga K-edge EXAFS data for RQ, FC $Ni_{2-x}Mn_{1+x}Ga$ series. Figures in parentheses signify variability in the last digit.

Alloy	Ni-Mn		Ni-Ga		Ga-Mn		Ni-Ni		Mn-Ga		Mn-Mn	
	R (Å)	σ^2 (Å^2)	R (Å)	σ^2 (Å^2)	R (Å)	σ^2 (Å^2)	R (Å)	σ^2 (Å^2)	R (Å)	σ^2 (Å^2)	R (Å)	σ^2 (Å^2)
Ni_2MnGa RQ	2.510(1)	0.010(1)	2.5104(1)	0.003(1)	2.899(1)	0.012(2)	2.899(1)	0.013(2)				
$Ni_{1.75}Mn_{1.25}Ga$ RQ	2.520(10)	0.009(1)	2.539(11)	0.009(1)	2.924(13)	0.016(3)	2.892(26)	0.018(5)				
$Ni_{1.5}Mn_{1.5}Ga$ RQ	2.525(3)	0.0104(4)	2.546(8)	0.008(1)	2.912(8)	0.017(2)	2.923(70)	0.023(12)			2.765(60)	0.009(9)
$Ni_{1.25}Mn_{1.75}Ga$ RQ	2.507(11)	0.009(2)	2.545(16)	0.009(1)	2.967(44)	0.012(9)	2.902(18)	0.017(3)	2.770(134)	0.013(16)	2.829(22)	0.004(6)
$Ni_{1.25}Mn_{1.75}Ga$ FC	2.505(7)	0.011(1)	2.544(12)	0.013(2)	2.950(25)	0.018(4)	2.895(21)	0.019(3)	2.716(27)	0.012(5)	2.732(50)	0.011(9)
$NiMn_2Ga$ RQ	2.512(16)	0.010(2)	2.529(36)	0.012(2)	2.950(30)	0.015(5)	2.897(29)	0.020(5)	2.707(38)	0.012(10)	2.871(37)	0.004(37)

Table 3.3: Values of near neighbour bond distances (R) and the mean-square disorder in the bond length (σ^2) obtained from simultaneous by the fitting of 30 K Ni, Mn, and Ga K-edge EXAFS for RQ, FC $Ni_{2-x}Mn_{1+x}Ga$ alloys. Figures in parentheses signify variability in the last digit.

Alloy	Ni-Mn		Ni-Ga		Ga-Mn		Ni-Ni		Mn-Ga		Mn-Mn	
	R (Å)	σ^2 (Å^2)	R (Å)	σ^2 (Å^2)	R (Å)	σ^2 (Å^2)	R (Å)	σ^2 (Å^2)	R (Å)	σ^2 (Å^2)	R (Å)	σ^2 (Å^2)
Ni_2MnGa RQ	2.525(6)	0.005(1)	2.507(3)	0.004(1)	2.806(9)	0.002(1)	2.794(12)	0.003(1)				
					3.035(23)	0.002(2)	3.036(29)	0.004(3)				
$Ni_{1.75}Mn_{1.25}Ga$ RQ	2.516(7)	0.004(1)	2.531(9)	0.004(1)	2.868(14)	0.004(3)	2.856(14)	0.003(2)				
					3.015(19)	0.003(4)	3.020(30)	0.003(2)				
$Ni_{1.5}Mn_{1.5}Ga$ RQ	2.513(4)	0.004(1)	2.550(6)	0.004(1)	2.920(12)	0.001(2)	2.892(29)	0.012(4)			2.795(36)	0.0028(4)
$Ni_{1.25}Mn_{1.75}Ga$ RQ	2.514(11)	0.005(1)	2.551(16)	0.006(1)	2.930(30)	0.013(5)	2.910(18)	0.013(3)	2.828(265)	0.029(50)	2.831(22)	0.003(4)
$Ni_{1.25}Mn_{1.75}Ga$ FC	2.526(13)	0.006(2)	2.580(12)	0.006(1)	2.780(7)	0.018(53)	2.780(7)	0.005(1)	2.670(36)	0.006(9)	2.787(24)	0.001(4)
					3.005(16)	0.025(56)	3.005(16)	0.006(1)				
$NiMn_2Ga$ RQ	2.512(16)	0.006(1)	2.529(36)	0013(1)	2.950(30)	0.013(5)	2.897(29)	0.029(21)	2.707(38)	0.008(4)	2.871(37)	0.028(11)

phases as defect phases, refinement of synchrotron x-ray diffraction patterns of all the $Ni_{2-x}Mn_{1+x}Ga$ (both RQ and FC alloys) was carried out. The diffraction patterns were recorded using x-rays of energy $\sim$ 19.5 KeV which is well above the absorption edge energies of the constituent elements. The refined patterns along with the difference spectra and the constituent phase markers are presented in Figs. 3.10 and 3.11. As deciphered from the lab XRD pattern, the crystal structures of the alloys with $x = 0$, 0.25, and 0.5 at

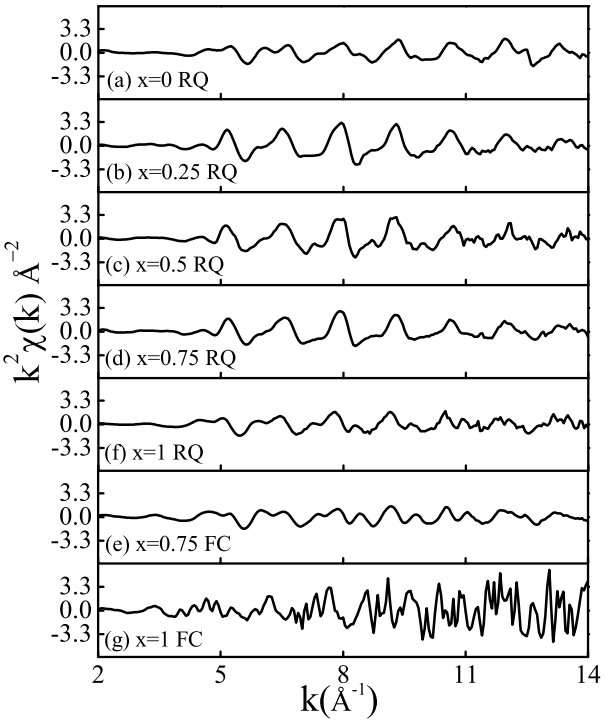

Figure 3.7: k^2 weighted raw EXAFS data recorded at the Ni K edge in $Ni_{2-x}Mn_{1+x}Ga$ (x = 0, 0.25, 0.5, 0.75 and 1) RQ and FC alloys.

room temperature are cubic $L2_1$ type with no other impurity phases (Fig. 3.10). Inclusion of cubic ($Fm\bar{3}m$) and tetragonal ($I4/mmm$) structures of Mn_3Ga along with the cubic Heusler structure reproduces the diffraction patterns of RQ and FC $Ni_{2-x}Mn_{1+x}Ga$ alloys with $x = 0.75$ and 1.0 quite well (Fig. 3.11). This indicates that the longer Mn–Ga and Mn–Mn nearest neighbour distances obtained from EXAFS analysis indeed arise from a Mn_3Ga type defect phase. The phase fractions of the constituent phases in $Ni_{1.25}Mn_{1.75}Ga$ and $NiMn_2Ga$ are tabulated in Table 3.4.

Mn_3Ga type phase in Mn-rich $Ni_{2-x}Mn_{1+x}Ga$ alloys can segregate via an antisite disorder between Mn and Ga (Y and Z) sites. To confirm the presence of such a disorder

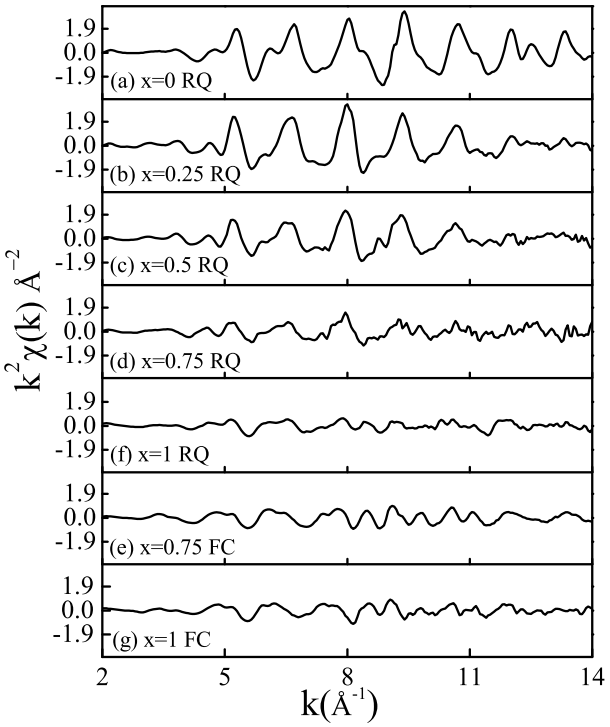

Figure 3.8: k^2 weighted raw EXAFS data recorded at the Mn K edge in $Ni_{2-x}Mn_{1+x}Ga$ (x = 0, 0.25, 0.5, 0.75 and 1) RQ and FC alloys.

Table 3.4: Phase fractions of constituent phases in $Ni_{1.25}Mn_{1.75}Ga$ and $NiMn_2Ga$ RQ and FC alloys. The shortfall in the sum of phase fractions is made up by MnO impurity phase.

Alloy	Phase Fractions			
	$L2_1$	$L1_2$	$D0_{22}$	$L1_0$
	$Fm\bar{3}m$	$Pm\bar{3}m$	$I4/mmm$	$P4/mmm$
$Ni_{1.25}Mn_{1.75}Ga$ RQ	80.47	11.23	8.30	–
$Ni_{1.25}Mn_{1.75}Ga$ FC	79.99	3.72	9.80	–
$NiMn_2Ga$ RQ	79.92	8.19	7.01	–
$NiMn_2Ga$ FC	70.17	3.79	13.94	5.54

we analyse the intensity variations of (111) and (200) superlattice reflections with that of the principal (220) reflection with an increase in the value of x. The intensity ratios, $I_{(111)}/I_{(220)}$ and $I_{(200)}/I_{(220)}$ provide information regarding the antisite disorder in the alloy. The $I_{(200)}/I_{(220)}$ provides information exclusively on occupancy disorder between X and

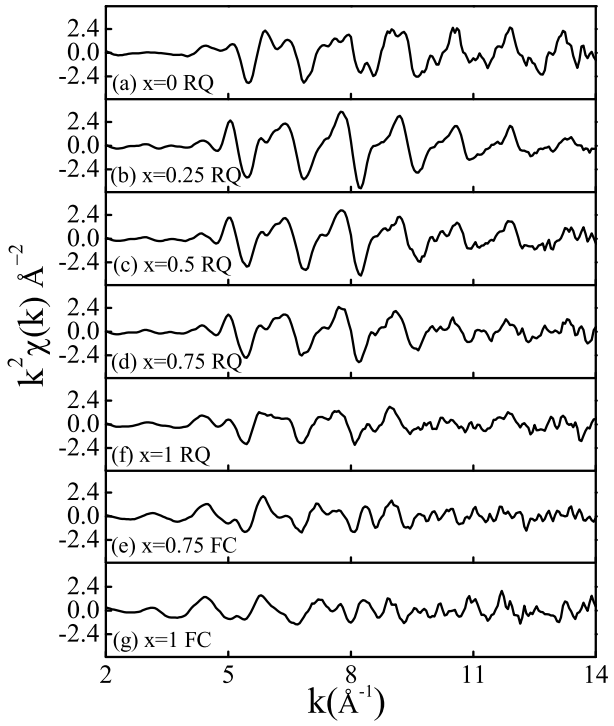

Figure 3.9: k^2 weighted raw EXAFS data recorded at the Ga K edge in $Ni_{2-x}Mn_{1+x}Ga$ (x = 0, 0.25, 0.5, 0.75 and 1) RQ and FC alloys.

Y/Z sublattices of the X_2YZ Heusler alloy. On the other hand, $I_{(111)}/I_{(220)}$ is affected by the disorder between Y and Z sublattices as well as the disorder between X and Y/Z sublattices.[25]

Fig. 3.12 displays the two observed ratios, $I_{(111)}/I_{(220)}$ and $I_{(200)}/I_{(220)}$ in panels (a) and (b) respectively along with the calculated ratios for both RQ and FC alloys. The calculated ratio represents the intensity ratio for an ordered $L2_1$ lattice of the type $Ni_{2-x}Mn_xMnGa$ where x = 0, 0.25, 0.5, 0.75, and 1.0. It can be seen that both calculated and observed $I_{(200)}/I_{(220)}$ ratios increase with the value of x. This is expected due to the increasing replacement of Ni by Mn atoms. Both the calculated and the observed ratios

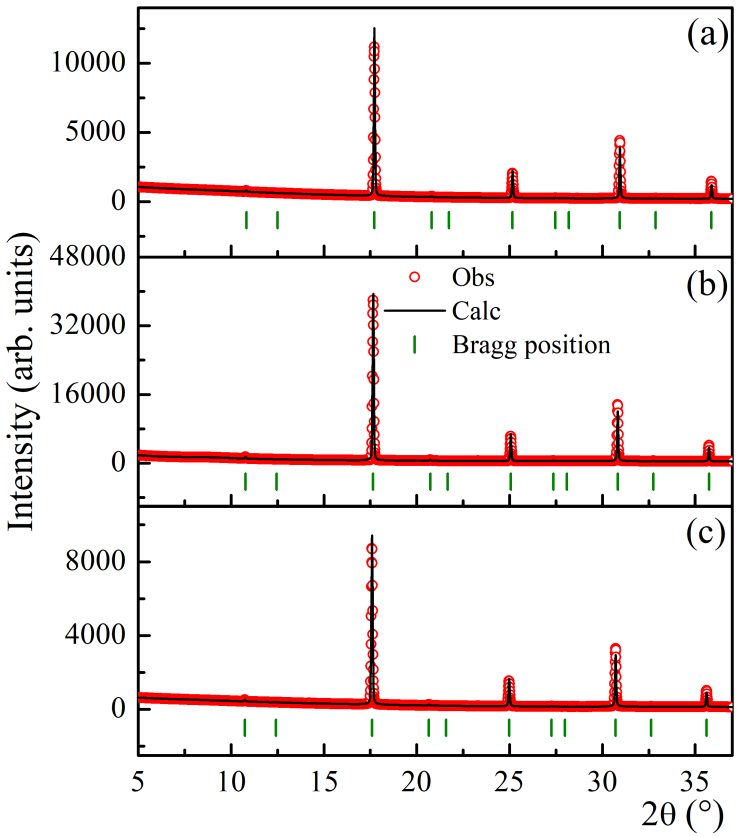

Figure 3.10: Synchrotron x-ray diffraction patterns of $Ni_{2-x}Mn_{1+x}Ga$, $x = 0$, 0.25 and 0.5 RQ alloys.

scale together in all RQ alloys up to $x = 0.75$. A decrease is seen in the observed ratio as compared to the calculated value for $x = 1.0$. The ratio of observed intensities further decreases with respect to the calculated values for the two FC alloys. Such a behavior hints at lower site disorder due to furnace cooling rather than quenching them from high temperature.

The $I_{(111)}/I_{(220)}$ ratio is expected to show minimum variation as a function of x as there is no disorder expected between Y and Z sublattices due to the substitution of Mn

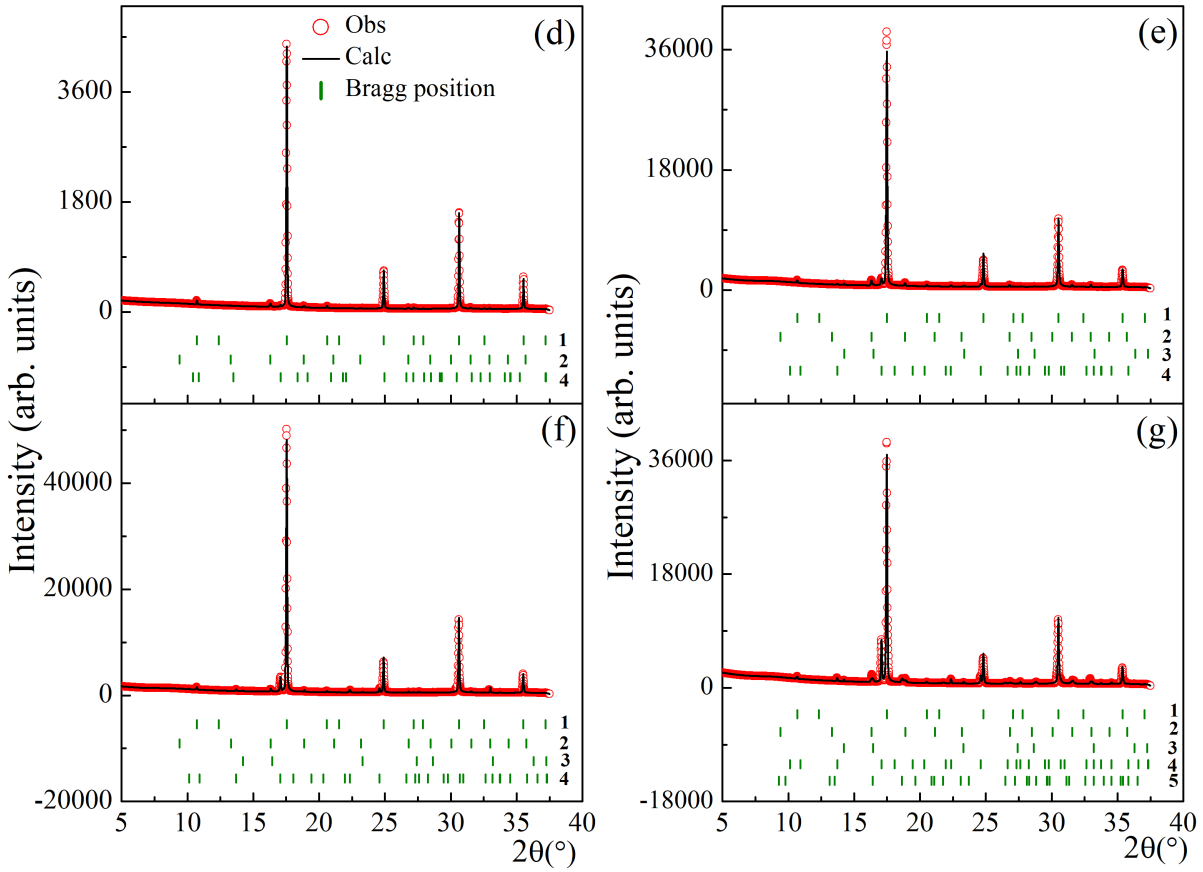

Figure 3.11: Synchrotron x-ray diffractograms of RQ and FC alloy compositions, $Ni_{1.25}Mn_{1.75}Ga$ and $NiMn_2Ga$. Structural phases identified from Rietveld analysis are indicated by numerals, 1 - $Fm3m$, 2 - $Pm3m$, 3- MnO, 4 - $I4/mmm$, and 5 - $P4/mmm$

for Ni at the X sites. The same is also reflected in the variation of the calculated ratio in Fig. 3.12 (a). Surprisingly the observed ratios display large deviations from the calculated values for alloys with $x \geq 0.5$. In the case of RQ alloys, the $I_{(111)}/I_{(220)}$ ratio increases steadily with x and reaches a maximum around $x = 0.75$ and then decreases sharply with further increase in the value of x. In the case of the two FC alloys, the intensity ratios are further affected and are much lower than their RQ counterparts.

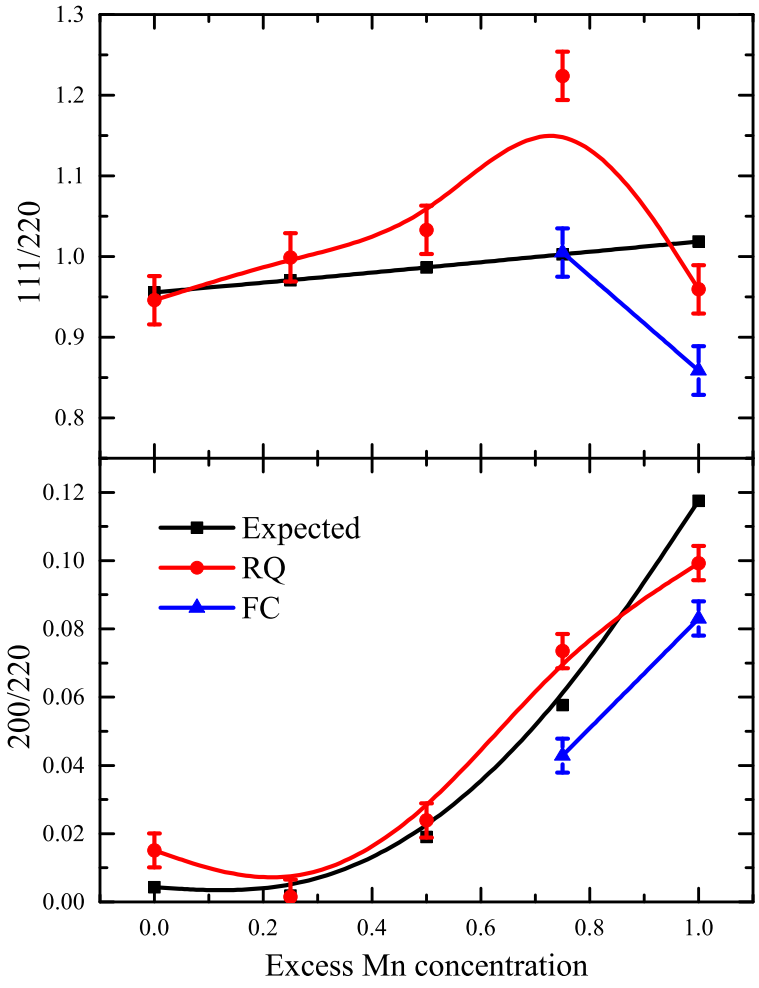

Figure 3.12: Variation of calculated and observed intensity ratios, $I_{(111)}/I_{(220)}$ and $I_{(200)}/I_{(220)}$ as a function of excess Mn concentration (x).

3.3 Discussion

Despite a reduction of the e/a ratio upon substituting Ni by Mn in Ni_2MnGa, the martensitic transition temperature increases after the initial decrease. This has been an unsolved puzzle challenging the so called e/a rule. In Ni-Mn-Ga Heulser alloys, irrespective of the alloy stoichiometry, the martensitic transformation temperature scales with the e/a ratio.[11] The only few exceptions are Mn_2NiGa and its derivatives. The main objective of

this work is to understand this violation of the e/a rule.

Structurally, Mn_2NiGa has always shown the presence of minor impurity phases and has been assigned to stress-induced modulated martensitic phases.[5,19] Its martensitic transition temperature is also sensitive to the thermal heat treatment given to the alloys.[20] Here too, the furnace-cooled alloys display higher T_M as compared to their quenched counterparts. Local structural studies of the Ni, Mn, and Ga, however, showed the presence of long Mn–Mn and Mn–Ga bond distances which could not be assigned to near-neighbour distances in $L2_1$ Heusler structure or the modulated martensitic structures reported for Ni-Mn-Ga alloys. These distances were found to close the Mn–Mn and Mn–Ga distances in Mn_3Ga cubic and tetragonal phases and the same was further confirmed from the refinement of synchrotron x-ray diffraction patterns.

Segregation of Mn_3Ga phases in the Mn_2NiGa Heusler structure is possible if there is an antisite disorder between the Y and Z sublattices of the X_2YZ Heusler structure. This possibility is schematically explained in Fig. 3.13. The $L2_1$ structure of the X_2YZ Heusler alloy is an ordered combination of two B2 lattices XY and XZ (Fig. 3.13 (a)) crystallizing in a face-centred cubic lattice. Replacing X with X' can lead to several possible scenarios of higher-order or antisite disorder. An ordering of X and X' atoms and giving rise to a Hg_2CuTi type structure with $F\bar{4}3m$ space group (Fig. 3.13 (b)). Without this X X' order, the structure remains $L2_1$ (Fig. 3.13 (c)) and also supports partial disorder between the constituent sub-lattices as shown in Fig. 3.13 (d). A disorder between Y and Z sublattices in the absence of order between X and X' atoms can lead to the segregation of Mn_3Ga

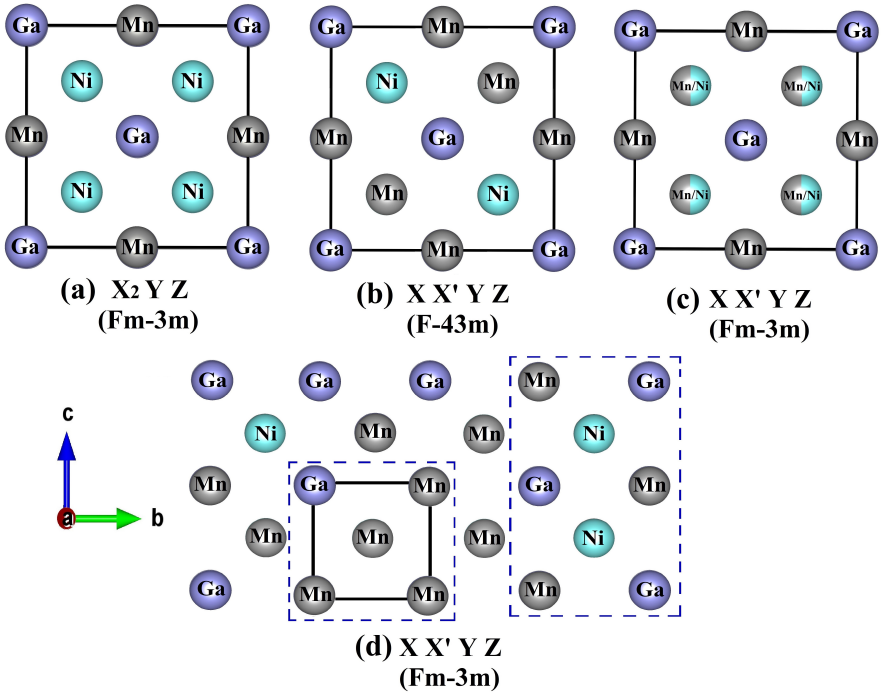

Figure 3.13: Two dimensional projections showing X_2YZ, ordered XX'YZ, disordered XX'YZ and the possible segregation of Mn_3Ga type defects due to antisite disorder in XX'YZ.

type defect phase and a Heulser phase. Mn_3Ga possesses either a cubic or tetragonal structure with nearest neighbour distances larger (2.7 Å to 2.8 Å) than those in the cubic Heusler alloy ($\sim$ 2.52 Å). This explains the observation of larger Mn–Ga and Mn–Mn bond distances from Mn and Ga EXAFS studies. It may be noted that these longer bond distances are especially seen in $Ni_{2-x}Mn_{1+x}Ga$ alloys with $x = 0.75$ and 1.0.

In the present $Ni_{2-x}Mn_{1+x}Ga$ alloys, the variation of intensity ratios of superlattice to principal reflections, especially I_{111}/I_{220} support the existence of antisite disorder between all three sublattices of the Heusler structure. The agreement between the observed and calculated I_{200}/I_{220} ratio indicates the substitution of Mn for Ni. Except for the quenched $NiMn_2Ga$ and the two FC alloy compositions ($x = 0.75$ and 1), there is a near-perfect

agreement between the calculated and the observed I_{200}/I_{220} ratio. Interestingly, in these alloys, the martensitic transition temperature scales with the e/a ratio. The martensitic transition is present in the RQ $NiMn_2Ga$, and the FC $Ni_{1.25}Mn_{1.75}Ga$ and $NiMn_2Ga$ alloys, and in all these three compositions significant deviation between the observed and calculated values of I_{200}/I_{220} is observed. The lower values of the observed intensity ratio indicate the formation of the Heusler phase richer in Ni as compared to the expected composition. This hypothesis also supports the segregation of Mn_3Ga type impurity phases. Formation of the Ni-rich Heusler phase and the Y – Z sublattice disorder needed for segregation of Mn_3Ga type phases is further supported by the higher observed I_{111}/I_{220} ratio as compared to the calculated values. A higher I_{111}/I_{220} ratio is possible in the case of occupancy disorder between Z(Ga) and Y(Mn) sublattices. It may also be noted that the ratio starts deviating from x= 0.5, the composition in which longer Mn–Mn bonds were first observed from the EXAFS analysis. Thus the considerably different observed intensity ratios of I_{111}/I_{220} and I_{200}/I_{220} indicate the formation of the Heusler phase richer in Ni than the expected composition and therefore higher e/a ratio. The scaling of T_M with e/a ratio in Ni-Mn-Ga Heusler alloys is well known. Therefore, the segregation of Ni-rich Heusler phases and Mn_3Ga type phases due to antisite disorder in $Ni_{2-x}Mn_{1+x}Ga$ alloys appears to be the primary reason for the increase in martensitic transition temperature of these alloys.

3.4 Conclusions

The increase of the martensitic transition temperature in $Ni_{2-x}Mn_{1+x}Ga$ alloys despite a decrease in the e/a ratio can be ascribed to a site occupancy disorder in the Heusler alloy that results in segregation of Mn_3Ga type defect phase and an Heusler phase that is rich in Ni. Substitution of Mn for Ni results in Mn–Mn nearest neighbor interactions which perpetrate Mn_3Ga type defects. These defects segregate in impurity phases with increasing substitution of Ni by Mn. The Ni-rich Heusler phases have a comparatively higher e/a ratio and appear to be the main cause of higher T_M in Mn_2NiGa as compared to Ni_2MnGa.

References

[1] G. D. Liu, J. L. Chen, Z. H. Liu, X. F. Dai, G. H. Wu, B. Zhang, and X. X. Zhang. *Applied Physics Letters*, 87(26):262504, 2005.

[2] S. Singh, S. Esakki Muthu, A. Senyshyn, P. Rajput, E. Suard, S. Arumugam, and S. R. Barman. *Applied Physics Letters*, 104(5):051905, 2014.

[3] S. Singh, R. Rawat, S. E. Muthu, S. W. D'Souza, E. Suard, A. Senyshyn, S. Banik, P. Rajput, S. Bhardwaj, A. M. Awasthi, et al. *Physical Review Letters*, 109(24):246601, 2012.

[4] D. M. Schaefer, A. J. A. de Oliveira, P.C. de Camargo, J. Varalda, W. H. Schreiner, and D.H. Mosca. *Intermetallics*, 91:22–30, 2017.

[5] P. J. Brown, T. Kanomata, K. Neumann, K. U. Neumann, B. Ouladdiaf, A. Sheikh, and K. R. A. Ziebeck. *Journal of Physics: Condensed Matter*, 22(50):506001, 2010.

[6] S. Paul, B. Sanyal, and S. Ghosh. *Journal of Physics: Condensed Matter*, 27(3):035401, 2014.

[7] J. Bai, J. Wang, S. Shi, X. Liang, Y. Yang, H. Yan, X. Zhao, L. Zuo, Y. Zhang, and C. Esling. *Modern Physics Letters B*, 35(10):2150231, 2021.

[8] S. W. D'Souza, T. Roy, S. Roy Barman, and A. Chakrabarti. *Journal of Physics: Condensed Matter*, 26(50):506001, 2014.

[9] K. Ullakko, J. K. Huang, C. Kantner, R. C. O'Handley, and V. V. Kokorin. *Applied Physics Letters*, 69(13):1966–1968, 1996.

[10] L. Righi, F. Albertini, G. Calestani, L. Pareti, A. Paoluzi, C. Ritter, P. A. Algarabel, L. Morellon, and M. Ricardo Ibarra. *Journal of Solid State Chemistry*, 179(11):3525–3533, 2006.

[11] J. Pons, V. A. Chernenko, R. Santamarta, and E. Cesari. *Acta Materialia*, pages 3027–3038.

[12] L. Righi, F. Albertini, E. Villa, A. Paoluzi, G. Calestani, V. Chernenko, S. Besseghini, C. Ritter, and F. Passaretti. *Acta Materialia*, 56:4529–4535, 2008.

[13] L. Righi, F. Albertini, L. Pareti, A. Paoluzi, and G. Calestani. *Acta Materialia*, 55(15):5237–5245, 2007.

[14] S. R. Barman, S. Banik, and A. Chakrabarti. *Physical Review B*, 72(18):184410, 2005.

[15] P. A. Bhobe, K. R. Priolkar, and P. R. Sarode. *Physical Review B*, 74(8):224425, 2006.

[16] H. Luo, F. Meng, Z. Feng, Y. Li, W. Zhu, G. Wu, X. Zhu, C. Jiang, and H. Xu. *Journal of Applied Physics*, 107(1):013905, 2010.

[17] G. D. Liu, X. F. Dai, S. Y. Yu, Z. Y. Zhu, J. L. Chen, G. H. Wu, H. Zhu, and J. Q. Xiao. *Physical Review B*, 74(5):054435, 2006.

[18] A. Kundu, M. E. Gruner, M. Siewert, A. Hucht, P. Entel, and S. Ghosh. *Physical Review B*, 96(13):064107, 2017.

[19] S. Singh, M. Maniraj, S. W. D'Souza, R. Ranjan, and S. R. Barman. *Applied Physics Letters*, 96(8):081904, 2010.

[20] J. Zhang, W. Cai, Z. Y. Gao, and J. H. Sui. *Scripta Materialia*, 58(9):798–801, 2008.

[21] S. V. Malik, E. T. Dias, A. K. Nigam, and K. R. Priolkar. *Journal of Physics D: Applied Physics*, 55(16):165002, 2022.

[22] A. Cakir, M. Acet, and M. Farle. *Scientific Reports*, 6:28931, 2016.

[23] R. Nevgi, E. T. Dias, and K. R. Priolkar. *Physical Review B*, 104(10):054101, 2021.

[24] A Çakır, M. Acet, L. Righi, F. Albertini, and M. Farle. *AIP Advances*, 5(9):097222, 2015.

[25] Y. Takamura, R. Nakane, and S. Sugahara. *Journal of Applied Physics*, 105:07B109, 2009.

Chapter 4

Antisite disorder and phase segregation in Mn_2NiSn.

4.1 Introduction

Inverse Heusler alloys of the type Mn_2XZ crystallizing in cubic or tetragonal structures have the Mn atoms occupy both the octahedral (0,0,0) or (0.5, 0.5, 0.5) and the tetrahedral sites (0.25, 0.25, 0.25) or (0.75, 0.75, 0.75) with antiparallel spins of different magnitudes resulting in a ferrimagnetic order.[1–4] These inverse Heusler alloys display a high Curie temperature (T_C) and outstanding functionalities due to a strong interplay between the crystal structure and magnetic properties. Mn_2NiGa exhibits a shape memory effect with a magnetic field induced strain up to 4%, a martensitic transformation temperature, T_M = 270 K, and a T_C = 588 K raising a high prospect for achieving a magnetic shape memory alloy with improved properties.[5] Density functional theory (DFT) calculations indicate similar possibilities in Mn_2NiAl.[6] Mn_2VAl behaves like a half-metallic ferromagnet, with the Mn moments associated with the two different crystallographic sites coupled parallel to one another.[7] Mn_2CoAl is reported as a spin gapless semiconductor with a very high magnetic ordering temperature of 720 K and also exhibits an anomalous

Hall effect.[8] Topological Hall effect has been reported in Mn_2PtIn and Mn_2PtSn inverse Heusler alloys.[9,10] Further, a large exchange-bias effect, even under zero-field cooled conditions is displayed by Mn_2PtSn, Mn_2PtGa[9–11]and Mn_2RhSn alloys.[12] Such tetragonally distorted doped inverse Heusler alloys also display novel noncollinear spin textures or antiskyrmions.[13,14] A high degree of spin polarization is reported in bulk as well as thin-film forms of Mn_2CoGa.[15] Mn_2FeGa behaves like an exchange spring, raising hopes of applications in magnetic storage technology.[16]

Mn_2NiSn is one such inverse Heusler alloy that orders magnetically at $T_C = 530$ K[17] and has gained attention due to the predicted volume-conserving martensitic transformation in the magnetically ordered state leading to the observation of the shape memory effect.[18] Several first principle calculations and experimental studies found Mn_2NiSn stabilizing into an ordered inverse Heusler structure (Sp.Gr: $F\bar{4}3m$).[17–21] However, a discrepancy exists related to the experimentally measured and the calculated magnetic moment values. Interestingly, the magnetic moment values calculated by DFT differ wildly from about 0.7 μ_B/f.u. to 3.25 μ_B/f.u.[17,22] while the measured net magnetic moment at 5 K for Mn_2NiSn is ~ 2.95 μ_B/f.u.[17] In Heusler alloys, the magnetic order is generally determined by the nearest neighbor exchange coupling and the above wide variation in the calculated and the experimental values of magnetic moment point to a lack of understanding of the magnetic exchange interactions in Mn_2NiSn. Electronic structure calculations have suggested two possible scenarios. One considers near-quenching of the Mn moments on the tetrahedral sites and thereby giving a magnetic moment value of 3.25 μ_B/f.u. which is

fairly close to the observed value.[17] The second approach argues for antisite disorder on the tetrahedral sites leading to the diminishing of the antiferromagnetic interactions and thus escalating the net Mn moment.[22,23]

The present work seeks to understand the structural interactions responsible for the observed magnetic properties of Mn_2NiSn. Starting with Ni_2MnSn, the Ni atoms at the tetrahedral sites are systematically replaced by Mn to realise $Ni_{2-x}Mn_{1+x}Sn$ (x = 0, 0.25, 0.5, 0.75 and 1.0) alloys. As the $L2_1$ unit cell of Ni_2MnSn consists of 8 Ni, 4 Mn, and 4 Sn atoms, the chosen values of x on average represent an incremental replacement of one Ni atom in each $L2_1$ unit cell. The alloys have been characterized for their crystal structure, magnetic and transport properties. Using extended x-ray absorption fine structure (EXAFS) at the Mn, Ni, and Sn K-edges the near neighbour bond distances between the constituent atoms have been determined and have been used to understand the structural and magnetic ground state in the alloys. Further, temper annealing treatment has been used to elucidate the nature of structural interactions in these alloys.

4.2 Results and Discussion

Rietveld analysed room temperature XRD patterns presented in Fig. 4.1 confirm the cubic $L2_1$ (Space group: $Fm\bar{3}m$) Heusler structure for the RQ series of alloys. The refined values of the lattice constant, a, are listed in Table. 4.1, display a monotonic increase with the increase in Mn concentration. Further, the values of a obtained for the two end members, $x = 0$ (Ni_2MnSn) and $x = 1$ ($NiMn_2Sn$) are in good agreement with

those reported in the literature.[17,24]

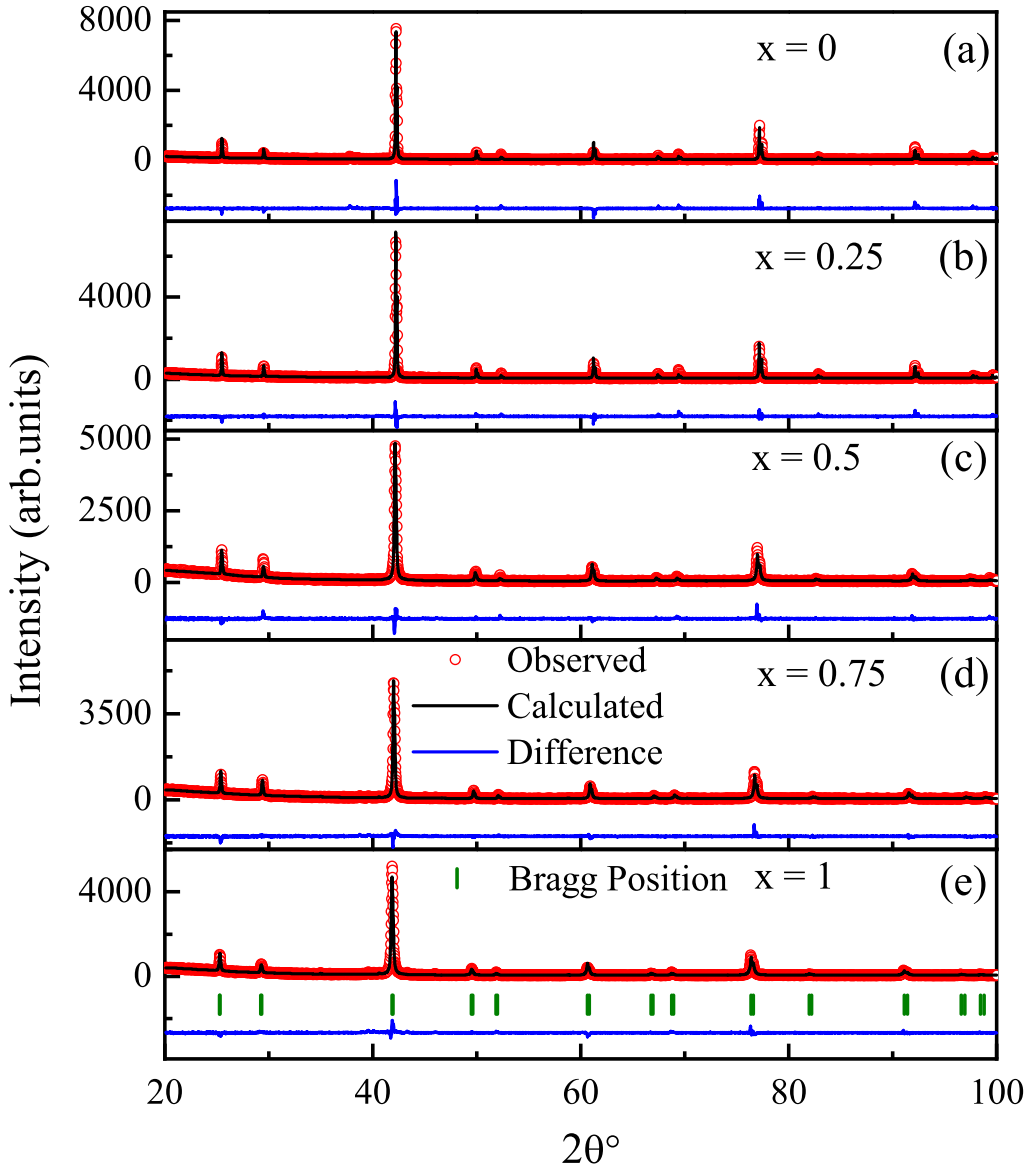

Figure 4.1: Rietveld refined room temperature XRD patterns for $Ni_{2-x}Mn_{1+x}Sn$ (x = 0, 0.25, 0.5, 0.75 and 1.0) RQ alloys.

Temperature-dependent magnetization M(T), for Ni_2MnSn, is presented in Fig. 4.2

(a). It displays a ferromagnetic behavior below $T_C \sim 340$ K in agreement with literature reports.[24] Similar measurements on other RQ alloys with higher Mn content suggests, the T_C systematically increases with increasing Mn substitution (see Table. 4.1). The T_C could not be determined for compositions with $x \geq 0.5$ as it was well above 390 K. Isothermal magnetisation (M(H)) was recorded by first cooling the sample from room temperature to 3 K in zero applied field and then recording the magnetization as the field was varied in the interval ±7 T. Hysteresis loops with low coercive fields presented in Fig. 4.2 (b) highlight the low-temperature ferromagnetic character of these alloys.[24] Values of the net magnetic moment are depicted in the inset of Fig. 4.2 (b). were estimated from the M(H) curves by linearly extrapolating the magnetization value at H = 7 T to meet the magnetization axis at H = 0 T. Up to $x = 0.5$, the magnetic moment remains almost invariant at about 4.0 $\mu_B/f.u.$ and then decreases to 1.93 $\mu_B/f.u.$ in x= 0.75 and again increases to about 2.8 $\mu_B/f.u.$ in $x = 1.0$ alloy. The sudden change in observed values of magnetic moment hints towards a change in magnetic order for $x \geq 0.75$ alloys.

Table 4.1: Initial and EDX compositions, lattice parameters determined from Rietveld refinements of the XRD patterns, and T_C determined from the temperature-dependent magnetization measurements of the quenched $Ni_{2-x}Mn_{1+x}Sn$ alloys.

Alloy	EDX Composition	Lattice parameters (Å)	T_C (K)
Ni_2MnSn	$Ni_{1.92}Mn_{0.99}Sn_{1.09}$	6.0499	340
$Ni_{1.75}Mn_{1.25}Sn$	$Ni_{1.74}Mn_{1.22}Sn_{1.04}$	6.0505	358
$Ni_{1.5}Mn_{1.5}Sn$	$Ni_{1.63}Mn_{1.53}Sn_{0.85}$	6.0618	> 390
$Ni_{1.25}Mn_{1.75}Sn$	$Ni_{1.39}Mn_{1.74}Sn_{0.86}$	6.0803	> 390
$NiMn_2Sn$	$Ni_{1.13}Mn_{2.00}Sn_{0.87}$	6.1027	> 390

Fig. 4.3 presents a comparison of the temperature dependence of resistivity (ρ(T)) recorded during warming cycles for the RQ series of alloys. While the overall metallic

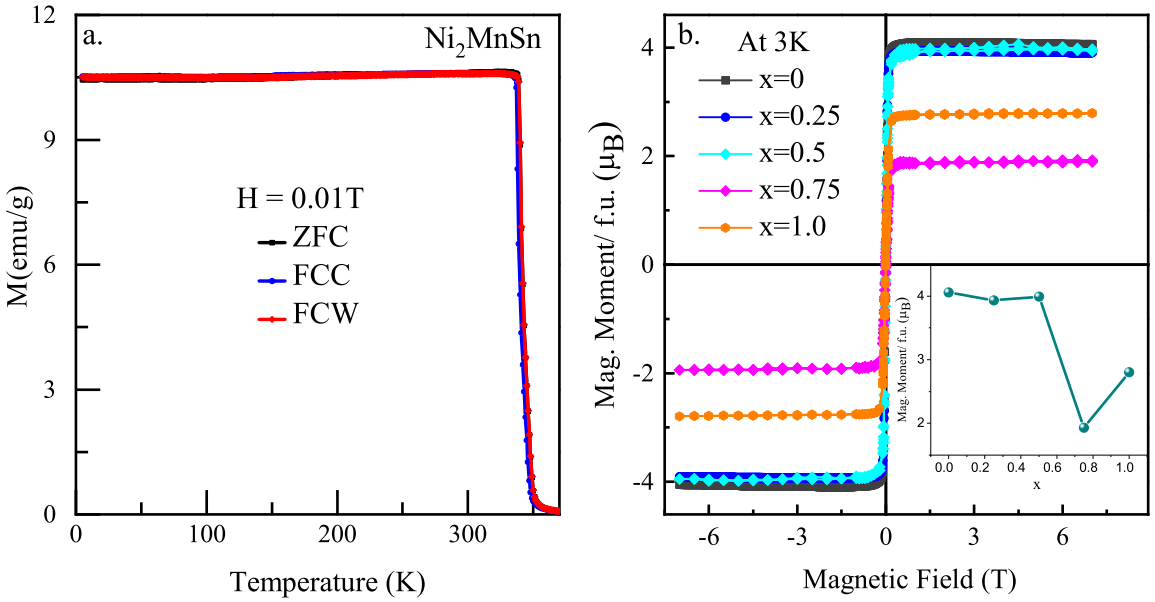

Figure 4.2: a. Temperature-dependent magnetization curves recorded for Ni_2MnSn in H = 0.01 T during ZFC, FCC, and FCW cycles. b. Isothermal magnetization curves recorded for the $Ni_{2-x}Mn_{1+x}Sn$ (x = 0, 0.25, 0.5, 0.75 and 1.0) RQ series of alloys at T = 3 K in H = $\pm$7T.

behaviour expected for non-martensitic alloys is preserved for all concentrations up to $x \leq 0.75$, increasing magnitudes of resistivity reflect corresponding changes in the band structure brought about by the replacement of Ni by Mn in the $L2_1$ structure. For $x = 1.0$, the rapidly quenched $NiMn_2Sn$ alloy exhibits a negative temperature coefficient of resistance across the entire temperature range. The negative $d\rho/dT$ can be ascribed to thermally activated hopping of the conduction electrons trapped in the localized impurity states.[25] The impurity states could arise from the formation of structural defects, due to Mn substitution.

To comprehend the magnetic and transport properties of the RQ alloys, a detailed study of the local structure of the constituent atoms is carried out by analysing RT and

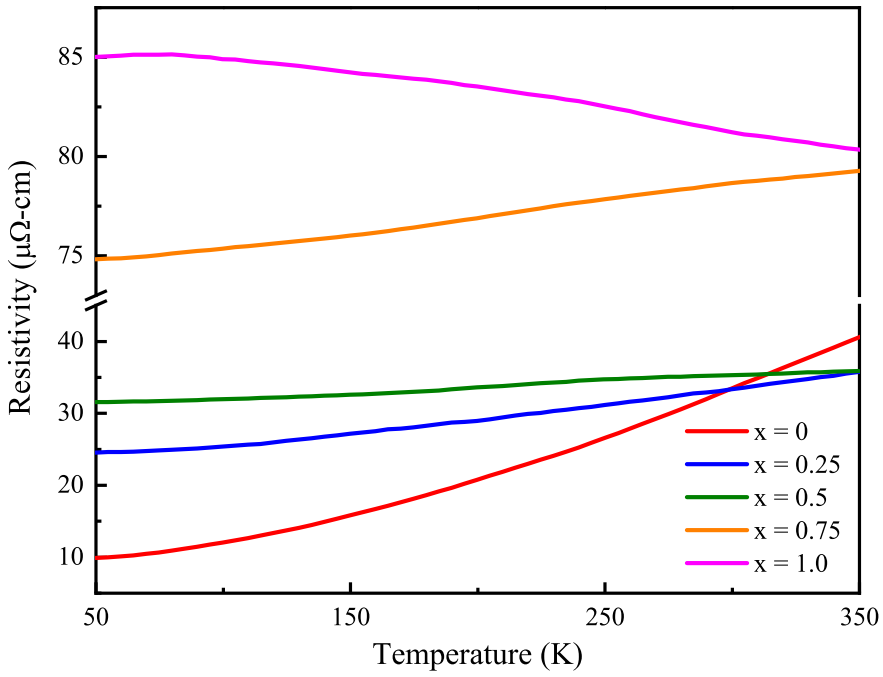

Figure 4.3: Temperature dependent resistivity curves recorded for the $Ni_{2-x}Mn_{1+x}Sn$ RQ series of alloys.

LT EXAFS data recorded at Ni, Mn, and Sn K edges in $Ni_{2-x}Mn_{1+x}Sn$. EXAFS signals at the three K edges were fitted simultaneously in the k range of 3.0 Å^{-1} to 12.0 Å^{-1} and in the R range of 1.0 Å to 3.0 Å. The magnitude of the Fourier transformed (FT) EXAFS data ($|\chi(R)|$) in the $R = 1$ Å to 3.5 Å range for three selected alloys, ($x = 0$, 0.75 and 1.0) are presented in Fig. 4.4.

In Ni_2MnSn with $L2_1$ structure, Ni is surrounded by 4 Mn and 4 Sn atoms in its first coordination shell at about 2.6 Å. Six Ni atoms at $\sim$ 3.0 Å complete the second shell. On the other hand, Mn and Sn atoms have 8 Ni atoms as their nearest neighbor and 6 Sn or 6 Mn atoms contribute as the second near neighbors respectively. Therefore, a simultaneous fitting of all three, Mn, Ni, and Sn EXAFS together results in only four

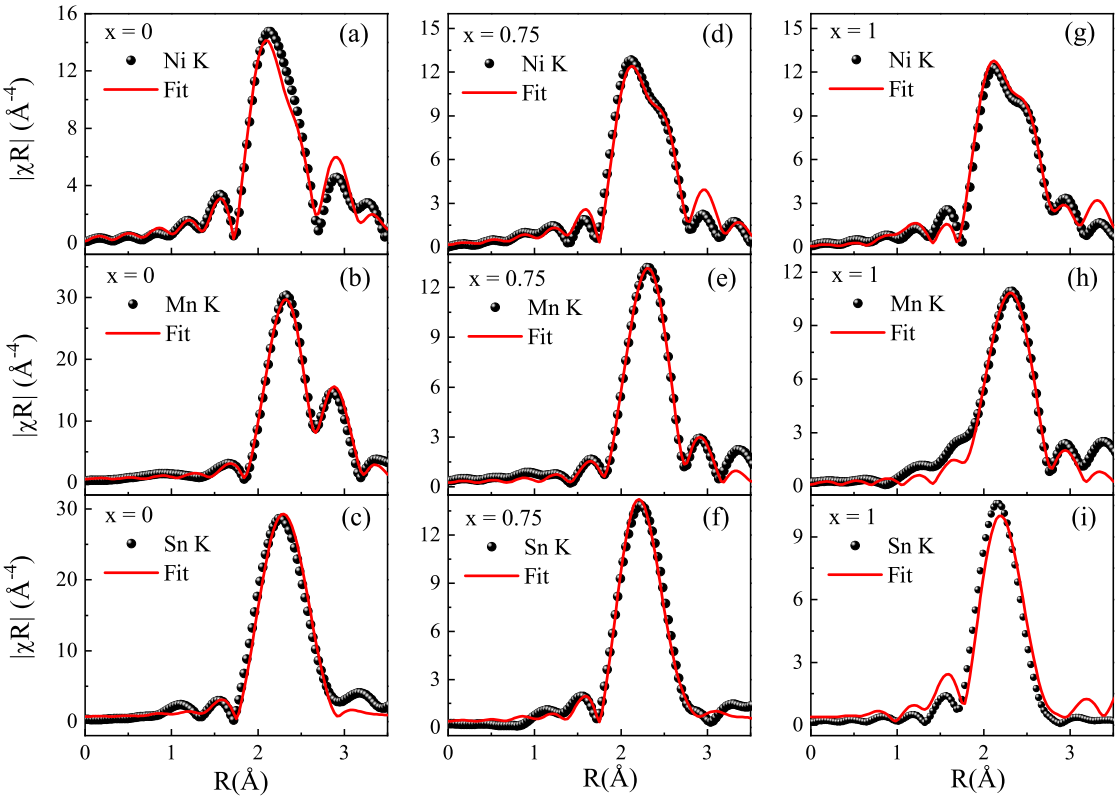

Figure 4.4: Fourier transform magnitudes of the k^3 weighted EXAFS at the Ni, Mn, and Sn edges along with corresponding best fits in RQ $Ni_{2-x}Mn_{1+x}Sn$ alloys for $x = 0$ (a-c), $x = 0.75$ (d-f) and $x = 1.0$ (g-i)

Table 4.2: Values of bond distances (R) and mean square disorder in bond distances (σ^2) obtained by simultaneous fitting of Ni, Mn and Sn EXAFS in $Ni_{2-x}Mn_{1+x}Sn$ series of RQ alloys, recorded at 100 K. Figures in parentheses designate uncertainty in the ending digits.

Bond	Ni_2MnSn		$Ni_{1.75}Mn_{1.25}Sn$		$Ni_{1.5}Mn_{1.5}Sn$		$Ni_{1.25}Mn_{1.75}Sn$		Mn_2NiSn	
	R(Å)	σ^2(Å^2)	R (Å)	σ^2(Å^2)	R(Å)	σ^2(Å^2)	R (Å)	σ^2(Å^2)	R (Å)	σ^2(Å^2)
Ni-Sn	2.612(1)	0.0030(2)	2.617(3)	0.0031(2)	2.617(6)	0.0040(5)	2.617(4)	0.003(1)	2.612(8)	0.004(1)
MnX-Sn	—	—					2.751(16)	0.008(3)	2.758(17)	0.006(2)
Ni-MnY	2.612(1)	0.005(1)	2.594(3)	0.0048(3)	2.601(8)	2.601(8)	2.610(6)	0.005(1)	2.596(10)	0.006(1)
MnX-MnY	—	—					2.861(56)	0.028(11)	2.818(45)	0.024(11)
MnX-Ni/MnX	—	—	3.005(6)	0.012(1)	2.898(21)	0.0024(3)				
Ni-Ni	3.016(1)	0.010(1)			3.008(21)	0.016(3)	3.004(19)	0.015(4)	3.022(57)	0.021(9)
MnY-Sn	3.016(1)	0.006(2)	2.995(16)	0.0012(2)	2.963(20)	2.963(20)	2.954(17)	0.013(2)	2.943(27)	0.015(4)

Ni-Mn_Y, Ni-Sn, Sn-Mn_Y, and Ni-Ni direct scattering correlations instead of seven when these edges are fitted independently. A fitting model employing the structural constraints of the $L2_1$ symmetry with change in bond distance (δR) and mean square disorder in the bond distance (σ^2) as variable parameters were conceived. In all the fittings, the coordination numbers were kept fixed to their model values. A similar approach was successfully implemented for fitting the EXAFS data in $Ni_{2+x}Mn_{1-x}Ga$ alloys.[26] The resulting good fit obtained in the R range of 1 Å to 3 Å, at 100 K is depicted in Fig. 4.4 (a), and the structural parameters obtained from the fittings are tabulated in Table 4.2. The introduction of Mn in place of Ni to realise in $Ni_{2-x}Mn_{1+x}Sn$ gives rise to additional three scattering correlations viz, Mn_X-Mn_Y, Mn_X-Sn, and Mn_X-Ni/Mn_X.

In the case of the $x = 0.25$ alloy, the contributions of Mn_X cannot be correctly isolated due to the lower sensitivity of x-rays in distinguishing between Ni (Z = 28) and Mn (Z = 25) as scatterers at the X sites. However, the $L2_1$ structural model without the constraints and with individual correlations varying independently resulted in a fairly good fit to the LT EXAFS data at all three edges. Extending this approach to $x = 0.5$ alloy did not result in a good fit and the correlations due to Mn_X atom had to be introduced sequentially. For $x = 0.5$ an Mn-Mn correlation at 2.89 Å was needed to describe the experimental Mn EXAFS well. The observed distance of this correlation is close to the expected Mn_X-Ni/Mn_X distance of 3.0 Å and hence we refer to the new Mn-Mn distance as Mn_X-Ni/Mn_X. With a further increase in the value of x to 0.75 and 1.0, another correlation, Mn-Sn had to be introduced to get a good fit to Mn and Sn K-edge EXAFS. However, the

best-fitted bond distance of about 2.75 Å was much larger than the expected Mn_X-Sn bond length of $\sim$ 2.6 Å. The Heusler structure of $Ni_{2-x}Mn_{1+x}Sn$ supports only two Mn-Sn bonds, Mn_X-Sn at $\sim$2.6 Å and Mn_Y-Sn at about 3.0 Å. The Mn_Y-Sn bond distance is correctly obtained from the fitting and therefore this additional Mn-Sn distance is ascribed to an elongated Mn_X-Sn bond. Further, the bond length of Mn_X-Ni/Mn_X correlation progressively decreases from 2.9 Å in $x = 0.5$ to 2.8 Å in $x = 1.0$. A similar decrease is also observed in Mn_Y-Sn bond distance as well. The Mn_Y-Sn correlation should have a distance of $a/2$ $\approx$3.025 Å(a is the lattice parameter). These two, Mn_X-Sn and Mn_X-Ni/Mn_X, misfit bond distances indicate a growing local structural disorder around Mn and Sn atoms in $Ni_{2-x}Mn_{1+x}Sn$ alloys. All the near neighbor distances are listed in Table 4.2 and the fits to the Mn, Ni, and Sn EXAFS data in $x = 0.75$ and 1.0 can be respectively seen in Figs. 4.4 (d – f) and in Figs. 4.4 (g – i).

A comparison of crystal structures of several alloys containing Mn and Sn suggests that the observed Mn-Sn bond distance is very close to the bond distances reported in Mn_3Sn type hexagonal $D0_{19}$ structure. Mn_3Sn type environment is possible in such $Ni_{2-x}Mn_{1+x}Sn$ with an antisite disorder among the Mn and Sn sublattices of the Heusler alloy. To check the possibility of such a disorder, the magnitudes of FT of EXAFS as the Mn, Ni, and Sn K edges are compared in Fig. 4.5. Little or no variation of FT amplitudes observed for Ni K edge (Fig. 4.5 (a)) suggests very little change in the local structural environment of Ni with Mn substitution in Ni_2MnSn. On the other hand, a systematic decrease in scattering amplitudes with increasing Mn concentration was observed for the

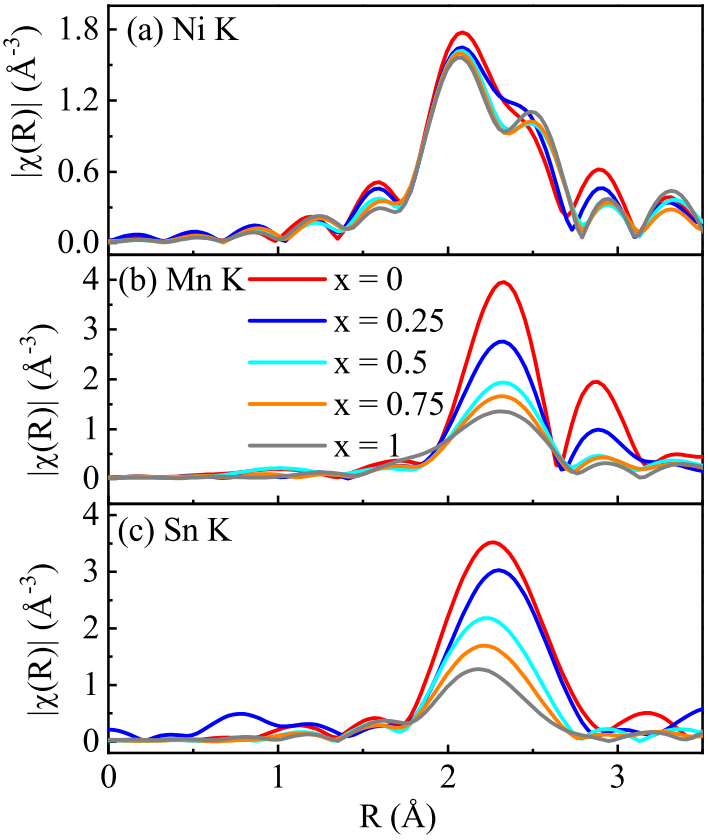

Figure 4.5: A comparison of FT magnitudes of EXAFS data at (a) Ni,(b) Mn, and (c) Sn K edges in $Ni_{2-x}Mn_{1+x}Sn$ RQ alloys.

Mn and Sn K edges in Figs. 4.5 (b) and (c). indicates the presence of disorder around the Mn and Sn atoms. Such structural defects are responsible for phase separation and the phenomenon of shell ferromagnetism in the $Ni_2Mn_{2-x}In_x$ alloys.[27] Upon temper annealing, these alloys phase separate into proportionate amounts of Heusler ($Ni_{50}Mn_{25}In_{25}$) and $L1_0$ ($Ni_{50}Mn_{50}$) phases.[28] On similar lines, the $Ni_{2-x}Mn_{1+x}Sn$ alloys can segregate into Ni_2MnSn and Mn_3Sn type phases. Segregation of Mn_3Sn type defects in $Ni_{2-x}Mn_{1+x}Sn$ alloys would require the presence of $B2$ type antisite disorder in them. Using Webster's

approach,[29] an attempt was made to calculate the possible $B2$ type disorder in all as prepared compositions of $Ni_{2-x}Mn_{1+x}Sn$ alloys. A maximum of 11% of $B2$ disorder was obtained in $NiMn_2Sn$ and it progressively decreased to negligible value in $Ni_{1.75}Mn_{1.25}Sn$.

To explore the possibility of phase separation in Mn-rich $Ni_{2-x}Mn_{1+x}Sn$ alloys, the compositions, $x = 0.75$ and 1.0 were temper annealed and investigated for their structure, magnetic and transport properties. Rietveld refined x-ray diffraction patterns recorded for the two temper annealed alloys ($x = 0.75$ and 1.0) are presented in Fig. 4.6. The diffraction pattern of $x = 1.0$ TA alloy consists of two phases, a major $L2_1$ ($\sim 93\%$) and a minor ($\sim 7\%$) Mn_3Sn type hexagonal phase (Space group: $P6_3/mmc$). The $x = 0.75$ however, presents itself as a single-phase alloy with cubic $L2_1$ Heusler structure. Studies on $Ni_{50}Mn_{50-x}Z_x$ have shown that the extent of phase separation depends on the time of annealing.[30] Further, lower the defect concentration, more annealing time is required for phase separation. Therefore, in the annealing time used here, the alloy with a larger concentration of structural defects ($NiMn_2Sn$) exhibits two crystallographic phases while $Ni_{1.25}Mn_{1.75}Sn$ presents a single-phase structure.

The magnetic and transport properties of these temper annealed alloys do show considerable changes in comparison to their RQ counterparts. The magnetic isotherms recorded at 3 K in a field of $\pm$7T for the two alloy compositions are presented in Fig. 4.7 (a). While the net magnetic moment in the phase-separated Mn_2NiSn alloy increases marginally to 2.83 μ_B/f.u., the magnetic moment in $Ni_{1.25}Mn_{1.75}Sn$ TA alloy displays a significant increase from 1.93 μ_B/f.u. in RQ alloy to 3.31 μ_B/f.u. in TA alloy. Further, the resistivity

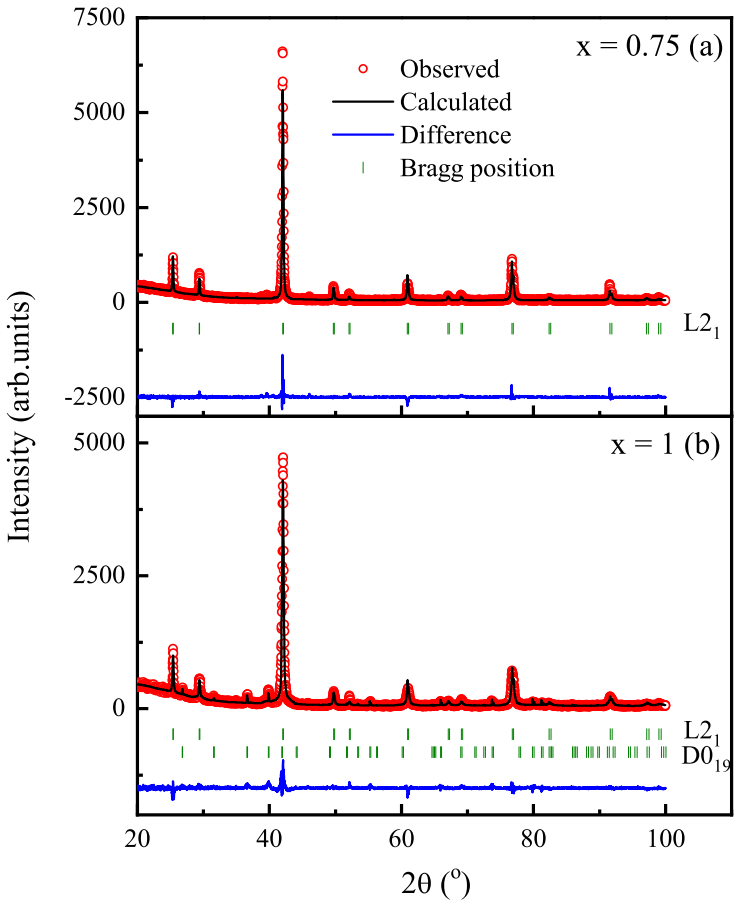

Figure 4.6: Rietveld refined XRD patterns for (a) $Ni_{1.25}Mn_{1.75}Sn$ and (b) $NiMn_2Sn$ TA alloys

as a function of temperature in Fig. 4.7 (b) exhibits a decrease in magnitude for both the TA alloys as compared to the corresponding RQ alloys and the temperature coefficient of resistance changes sign from negative to positive in $NiMn_2Sn$ TA alloy.

Recent EXAFS studies on temper annealed $Ni_2Mn_{2-x}In_x$ alloys have shown that complete phase separation is present at least at the local structural level even if the alloy presents a single-phase structure in XRD.[27] Therefore, to check the extent of phase separation and the changes in the local structural environment due to temper annealing, the

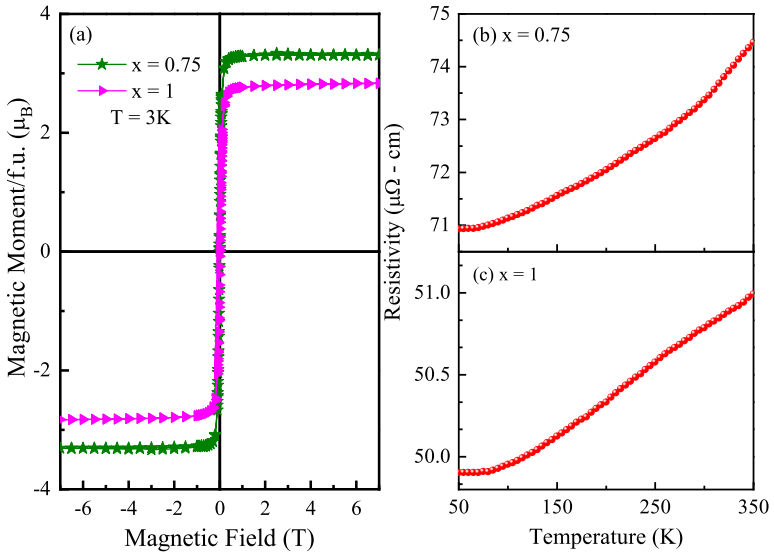

Figure 4.7: (a) Magnetic isotherms at 3 K in ±7T, (b) Temperature dependent resistivity for $Ni_{1.25}Mn_{1.75}Sn$ and $NiMn_2Sn$ TA alloys.

LT EXAFS data recorded at the Mn, Ni, and Sn K edges in $Ni_{1.25}Mn_{1.75}Sn$ and $NiMn_2Sn$ TA alloys are compared with the respective EXAFS data recorded in the RQ alloys (see Fig. 4.8). The comparison shows clear deviations in the FT magnitude of Mn and Sn EXAFS in $x = 1.0$ while subtle deviations are also noted for x= 0.75 alloys. In both the alloys, the Ni local structure remains relatively unaffected due to temper annealing, thus giving weight to the possibility of phase separation of these Mn-rich $Ni_{2-x}Mn_{1+x}Sn$ TA alloys into Ni_2MnSn type Heusler and Mn_3Sn type $D0_{19}$ phases.

To further confirm the phase separation of the TA alloys, EXAFS data at all three edges were fitted to a phase-separated model consisting of near neighbor correlations from Ni_2MnSn and Mn_3Sn structures. The resulting good fits are depicted in Fig. 4.9 and the corresponding best-fit parameters are summarised in Table. 4.3. The fitted percentage phase fractions in the TA alloys indicate a complete phase separation of the two TA alloy

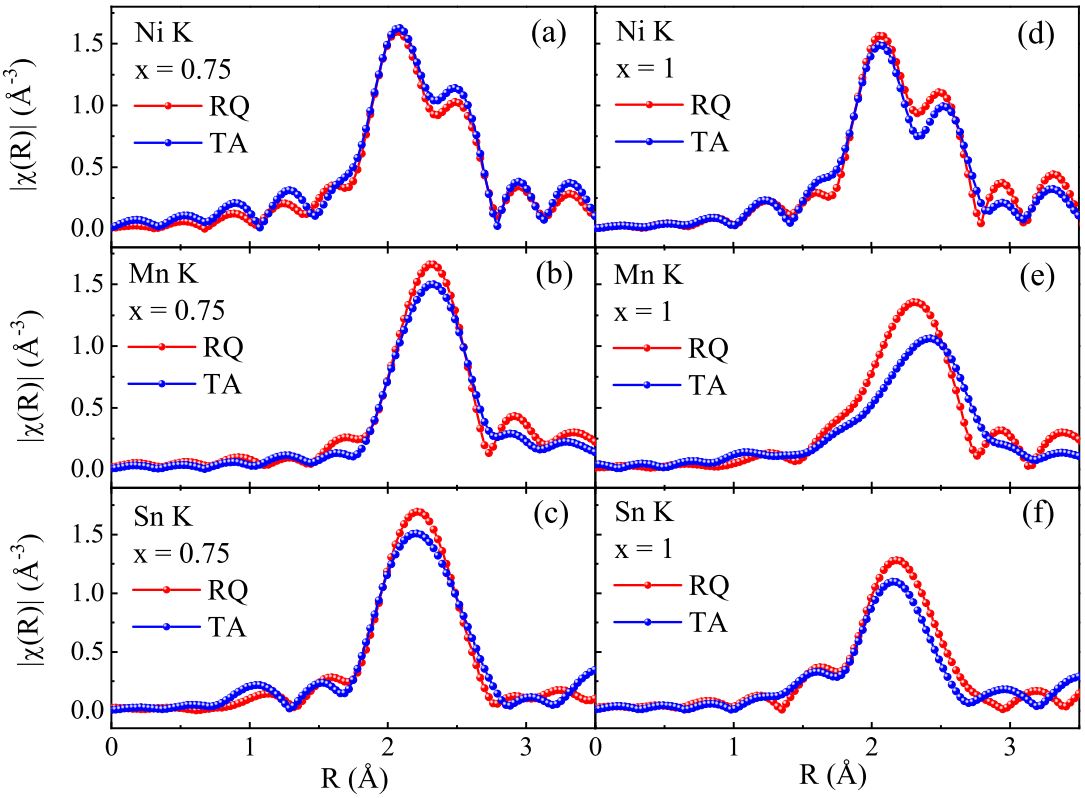

Figure 4.8: A comparison of FT magnitude of the Ni, Mn, and Sn EXAFS in RQ and TA $Ni_{1.25}Mn_{1.75}Sn$ and $NiMn_2Sn$ alloys.

compositions into $L2_1$ and $D0_{19}$ phases. However, the two Mn-Mn and Mn-Sn correlations of the hexagonal phase could not be individually fitted in $Ni_{1.25}Mn_{1.75}Sn$. They were combined and considered as one Mn-Mn and one Mn-Sn correlation. In $NiMn_2Sn$, the two Mn-Mn and two Mn-Sn correlations were fitted individually as can be seen in Table 4.3.

The phase-separated model was also applied to the two RQ alloy compositions with x = 0.75 and 1.0. Similar good fits were obtained for both the alloys but the phase fractions of the two phases were different. In the case of $Ni_{1.25}Mn_{1.75}Sn$ the fractions of the $L2_1$

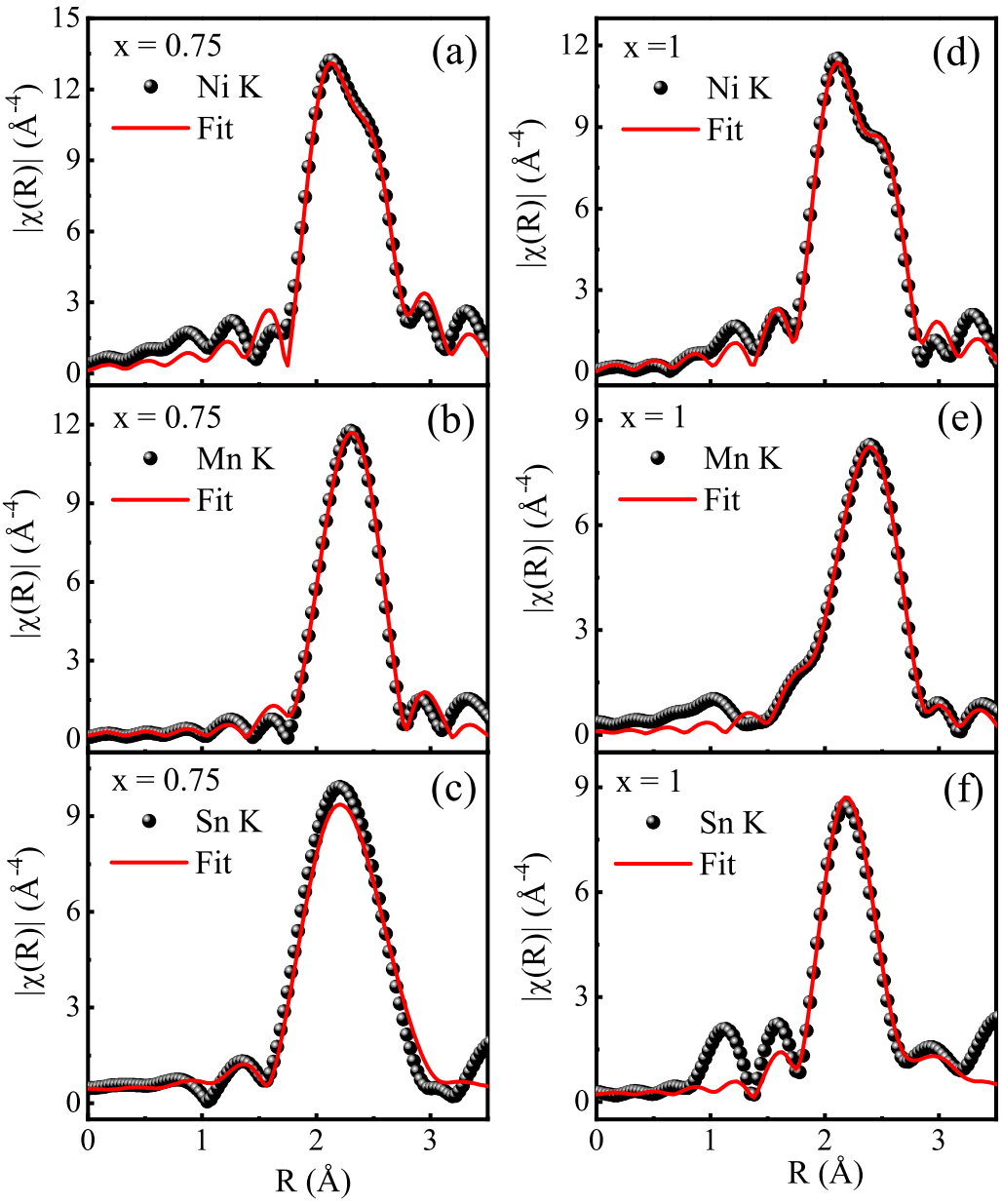

Figure 4.9: FT magnitude of k^3 weighted EXAFS at Ni, Mn, and Sn K edges and the corresponding best fits in $Ni_{2+x}Mn_{1-x}Sn$ (x = 0.75, 1) TA alloys.

and $D0_{19}$ phases respectively were $65 \pm 4\%$ and $35 \pm 4\%$ and in $NiMn_2Sn$ the percentage fractions of the cubic and hexagonal phases were obtained to be $73 \pm 16\%$ and $27 \pm 16\%$ respectively. This observation of phase separation at the local structural level confirms the

Table 4.3: Bond distances (R) and mean square disorder in the bond distance (σ^2) obtained by simultaneous fitting of Ni, Mn and Sn EXAFS recorded at 100 K in $Ni_{2+x}Mn_{1-x}Sn$ (x = 0.75, 1) TA alloys. Figures in parentheses designate uncertainty in the ending digits.

Bond	$Ni_{1.25}Mn_{1.75}Sn$			Mn_2NiSn		
	Phase Fraction %	R (Å)	σ^2(Å^2)	Phase fraction %	R (Å)	σ^2(Å^2)
Ni-Sn	0.63(5)	2.616(4)	0.004(1)	0.50(4)	2.615(5)	0.006(1)
Ni-Mn		2.592(6)	0.006(1)		2.580(5)	0.006(1)
Ni-Ni		3.026(26)	0.021(4)		3.021(15)	0.021(4)
Mn-Sn		3.045(40)	0.009(3)		2.994(19)	0.004(1)
Mn-Mn	0.37(5)	3.140(27)	0.010(4)	0.50(4)	2.723(7)	0.005(1)
Mn-Mn					2.901(17)	0.007(2)
Mn-Sn		2.770(19)	0.011(3)		2.725(12)	0.004(1)
Mn-Sn					3.102(32)	0.011(4)

formation of a defect phase within the overall $L2_1$ symmetry. The near neighbour Mn-Mn and Mn-Sn bond distances in Mn_3Sn are much longer than the Mn-Mn and Mn-Sn bond distances in the $L2_1$ phase. Therefore, the formation of such elongated bonds within the $L2_1$ symmetry should exert pressure on other near neighbour distances. Indeed such a contraction of Mn_X-Ni/Mn_X and Mn_Y-Sn bonds is observed in $Ni_{2-x}Mn_{1+x}Sn$ RQ alloys with $x \geq 0.5$.

The formation of the structural defects and the eventual phase separation on temper annealing also explains the observed magnetic and transport properties. The high value of resistance and the negative temperature coefficient of resistance in rapidly quenched $NiMn_2Sn$ is a result of the scattering of charge carriers by the structural defects. Temper annealing leads to an overall decrease in resistance and a change in character in the case of $NiMn_2Sn$. This can be ascribed to the metallic nature of the two phases formed upon temper annealing. Similarly, the increasing fraction of ferromagnetic Ni_2MnSn type

Heusler component from 50% in $NiMn_2Sn$ to 63% in $Ni_{1.25}Mn_{1.75}Sn$ gives an explanation to the rise in the magnetic moment from 2.83 μ_B/f.u. to 3.31 μ_B/f.u.

4.3 Conclusion

In conclusion, the Mn substitution in $Ni_{2-x}Mn_{1+x}Sn$ leads to the formation of Mn_3Sn type structural defects. These defects are initiated by an antisite disorder between Sn occupying the Z sublattice and Mn at the Y sublattice. These structural defects segregate and phase separate upon temper annealing. Defect concentration seems to increase with the increase in Mn substitution at the X site and thus this substituted Mn could be the precursor for Y-Z antisite disorder. The structural defects also explain the observed magnetic and transport properties.

References

[1] T. Graf, C. Felser, and S. S. P. Parkin. *Progress in Solid State Chemistry*, 39(1):1–50, 2011.

[2] C. Felser, G. H. Fecher, and B. Balke. *Angewandte Chemie International Edition*, 46(5):668–699, 2007.

[3] L. Wollmann, S. Chadov, J. Kübler, and C. Felser. *Physical Review B*, 90(21):214420, 2014.

[4] L. Wollmann, S. Chadov, J. Kübler, and C. Felser. *Physical Review B*, 92(6):064417, 2015.

[5] G. D. Liu, J. L. Chen, Z. H. Liu, X. F. Dai, G. H. Wu, B. Zhang, and X. X. Zhang. *Applied Physics Letters*, 87(26):262504, 2005.

[6] S. Kadri, S. Labidi, R. Masrour, A. Jabar, M. Labidi, and M. Ellouze. *Phase Transitions*, 92(8):699–706, 2019.

[7] C. Jiang, M. Venkatesan, and J. M. D Coey. *Solid State Communications*, 118(10):513–516, 2001.

[8] S. Ouardi, G. H. Fecher, C. Felser, and J. Kübler. *Physical Review Letters*, 110(10):100401, 2013.

[9] B. Giri, A. I. Mallick, C. Singh, P. V. P. Madduri, F. Damay, A. Alam, and A. K. Nayak. *Physical Review B*, 102(6):014449, 2020.

[10] Y. Li, B. Ding, X. Wang, H. Zhang, W. Wang, and Z. Liu. *Applied Physics Letters*, 113(6):062406, 2018.

[11] A. K. Nayak, M. Nicklas, S. Chadov, C. Shekhar, Y. Skourski, J. Winterlik, and C. Felser. *Physical Review Letters*, 110(12):127204, 2013.

[12] O. Meshcheriakova, S. Chadov, A. K. Nayak, U. K. Rößler, J. Kübler, G. André, A. A. Tsirlin, J. Kiss, S. Hausdorf, A. Kalache, et al. *Physical Review Letters*, 113(8):087203, 2014.

[13] A. K. Nayak, V. Kumar, T. Ma, P. Werner, E. Pippel, R. Sahoo, F. Damay, U. K. Rößler, C. Felser, and S. S. P. Parkin. *Nature*, 548:561–566, 2017.

[14] J. Jena, R. Stinshoff, R. Saha, A. K. Srivastava, T. Ma, H. Deniz, P. Werner, C. Felser, and S. S. P. Parkin. *Nano Letters*, 20(1):59–65, 2020.

[15] V. Alijani, J. Winterlik, G. H. Fecher, and C. Felser. *Applied Physics Letters*, 99(22):222510, 2011.

[16] T. Gasi, A. K. Nayak, J. Winterlik, V. Ksenofontov, P. Adler, M. Nicklas, and C. Felser. *Applied Physics Letters*, 102(20):202402, 2013.

[17] H. Luo, G. Liu, Z. Feng, Y. Li, Li Ma, G. Wu, X. Zhu, C. Jiang, and H. Xu. *Journal of Magnetism and Magnetic Materials*, 321(24):4063–4066, 2009.

[18] Y. N. Duan, X. X. Fan, A. Kutluk, X. J. Du, Z. W. Zhang, and Y. L. Song. *Journal of Magnetism and Magnetic Materials*, 386:102–106, 2015.

[19] Y. Chieda, T. Kanomata, K. Fukushima, K. Matsubayashi, Y. Uwatoko, R. Kainuma, K. Oikawa, K. Ishida, K. Obara, and T. Shishido. *Journal of Alloys and Compounds*, 486:51–54, 2009.

[20] S. Paul and S. Ghosh. *Journal of Applied Physics*, 110(6):063523, 2011.

[21] Y. Khatri, R. Skomski, W. Zhang, S. R. Valloppilly, D. J. Sellmyer, and A. Kashyap. *AIP Advances*, 11(1):015109, 2021.

[22] S. Paul, A. Kundu, B. Sanyal, and S. Ghosh. *Journal of Applied Physics*, 116(13):133903, 2014.

[23] S. Paul and S. Ghosh. *Journal of Physics: Condensed Matter*, 23:206003, 05 2011.

[24] M. Nazmunnahar, T. Ryba, J. J. del Val, M. Ipatov, J. Gonzalez, V. Hašková, P. Szabó, P. Samuely, J. Kravcak, Z. Vargova, and R. Varga. *Journal of Magnetism and Magnetic Materials*, 386:98–101, 2015.

[25] W. Y. Zhang, R. Skomski, S. R. Valloppilly, Y. Khatri, A. Kashyap, and D. J. Sellmyer. *Journal of Magnetism and Magnetic Materials*, 537:168157, 2021.

[26] P. A. Bhobe, K. R. Priolkar, and P. R. Sarode. *Physical Review B*, 74(8):224425, 2006.

[27] R. Nevgi, E. T. Dias, and K. R. Priolkar. *Physical Review B*, 104(10):054101, 2021.

[28] A. Çakir, M. Acet, and M. Farle. *Scientific Reports*, 6:1–5, 2016.

[29] J. W. Peter. *Contemporary Physics*, 10(6):559–577, 1969.

[30] L. Dincklage, F. Scheibel, A. Çakir, M. Farle, and M. Acet. *AIP Advances*, 8(2), 2018.

Chapter 5

Ni induced ferromagnetism in Mn_3Ga.

5.1 Introduction

Complete replacement of Ni in Ni_2MnGa results in Mn_3Ga. We have shown in Chapter 3 that antisite disorder results in the segregation of Mn_3Ga-type defects in $Ni_{2-x}Mn_{1+x}Ga$. These structural defects play an important role in the resulting martensitic properties of these Mn-rich alloys. For instance, we could show that the higher martensitic transformation temperature of Mn_2NiGa, despite its lower e/a ratio, is due to composition variation and defect segregation resulting in Ni-rich Ni-Mn-Ga and Mn_3Ga. An increase of Mn content beyond 1 gives rise to multiphase compounds until $Ni_{0.25}Mn_{2.75}Ga$. In this chapter, we discuss the structural and magnetic properties of $Mn_{3-x}Ni_xGa$ alloys with (x = 0 and 0.25).

Mn_3Ga crystallizes in two stable structures, the tetragonal $D0_{22}$ and the hexagonal $D0_{19}$. While the $D0_{22}$ phase of Mn_3Ga is ferrimagnetic, Mn_3Ga in the $D0_{19}$ phase orders antiferromagnetically.[1–3] Apart from these two stable structures, Mn_3Ga can also be prepared into a metastable disordered Cu_3Au-type structure with a nearly zero moment

antiferromagnetic ground state.[4] Further, it has been anticipated as a completely compensated half-metallic ferrimagnet with a cubic DO_3-type Heusler structure but so far not realized experimentally.[5,6]

Antiferromagnetic materials with characteristic features like high-speed spin dynamics, low susceptibility towards stray magnetic fields, greater packing density, etc, have opened up a new area of research called antiferromagnetic spintronics.[7–10] Magnetic tunnel junctions, spin valves, and spin transfer torque applications demand antiferromagnets with large magnetocrystalline anisotropy, zero magnetic moment, high magnetic ordering temperatures, stable crystal structure, low Gilbert damping, and ultrafast long-lived spin precession properties.[11–15] Though the disordered Cu_3Au-type cubic phase of Mn_3Ga is not known to exhibit any profound spintronics applications. However, the atomic site disorder in the cubic Mn_3Ga can be effectively used to realize novel magnetic phases with unique coupling via elemental substitution or through unique methods of sample preparation.[16,17]

Conventionally, the magnetic field is used to alter the orientation of magnetic spins in a ferromagnet and carry the information. However, this is not easily possible in an antiferromagnet. Therefore, alternative methods need to be used to manipulate the magnetic spin order in antiferromagnetic materials. Several studies have attempted to control spin ordering in antiferromagnets via magnetic, electrical, strain, and optical manipulation.[18,19]

An antiferromagnet with weak ferromagnetism can be used in spintronics applications

such as, in memory devices.[20,21] Further, weak ferromagnetism in an antiferromagnet is proved beneficial for controlling the large Hall signals.[22,23] Given the fact that Mn_2NiGa and Ni_2MnGa exhibit ferromagnetism, substituting Mn by Ni in Mn_3Ga can be used as a tool to tune the antiferromagnetic spin order in cubic Mn_3Ga. This is also in accordance with the Slater-Pauling rule as the substitution of Ni in Mn_3Ga will increase the electron count. It may be noted that Mn_3Ga has an electron count of 24 which, as per the Slater-Pauling rule corresponds to zero magnetic moment.

5.2 Results

The crystal structure of Mn_3Ga ($x = 0$) and $Ni_{0.25}Mn_{2.75}Ga$ ($x = 0.25$) annealed at 850°C (referred to as high temperature annealed or HTA alloys) was examined using x-ray diffraction patterns recorded at room temperature and are depicted in Fig. 5.1. The diffraction peaks are broad and can be indexed to a single disordered Cu_3Au-type cubic crystal structure. No other secondary reflections were found within the detection limits.

The disordered Cu_3Au-type structure has Mn and Ga occupying the 4a Wyckoff sites in $Fm\bar{3}m$ space group in a 75:25 ratio. All the Bragg peaks were indexed based on $Fm\bar{3}m$ symmetry and the lattice constant was calculated using the formula, $n\lambda = 2dsin\theta$. The calculated values of the lattice constant for individual Bragg reflections are reported in Table 5.1. The lattice constant for Mn_3Ga was found to be 3.79±1 Å which is in close agreement with that reported for Mn_3Ga melt-spun ribbons.[4] In the case of $Ni_{0.25}Mn_{2.75}Ga$, the lattice constant increased marginally to 3.80±2 Å .

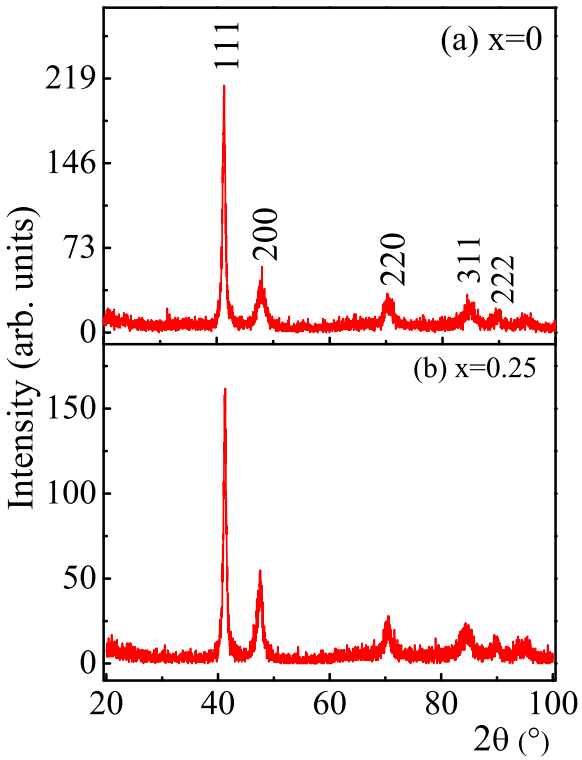

Figure 5.1: (a) and (b) XRD patterns for HTA $Mn_{3-x}Ni_xGa$ $x = 0$ and $x = 0.25$ alloys respectively.

Table 5.1: The estimated inter-planar distance 'd' and the lattice parameter 'a' for Mn_3Ga and $Ni_{0.25}Mn_{2.75}Ga$ alloys.

h k l	Mn_3Ga			$Ni_{0.25}Mn_{2.75}Ga$		
	Peak position $2\theta(^\circ)$	d (Å)	a (Å)	Peak position $2\theta(^\circ)$	d (Å)	a (Å)
1 1 1	41.30	2.19	3.79	41.23	2.19	3.79
2 0 0	47.89	1.90	3.80	47.54	1.91	3.83
2 2 0	70.43	1.34	3.78	70.41	1.34	3.78
3 1 1	84.74	1.14	3.79	84.47	1.15	3.80
2 2 2	90.09	1.09	3.77	89.68	1.09	3.79

Fig. 5.2 (a) displays the magnetization measurement as a function temperature for Mn_3Ga and $Ni_{0.25}Mn_{2.75}Ga$. During this measurement, the sample was initially cooled to 5 K in the absence of an external magnetic field. At 5 K, the field of 100 Oe was applied, and the data was recorded during warming (ZFC), subsequently while cooling (FCC), and

then while second warming (FCW). The magnetization of Mn_3Ga showcased a low value with a weak dependence on temperature and a small thermal irreversibility between the ZFC and FCC curves. The HTA Mn_3Ga is known to transform from antiferromagnetic to paramagnetic phase at 420 K. In addition, it also undergoes two distinct coupled structural and magnetic transitions at the temperatures of 600 K and 800 K.[4] All these transitions are well above the measured range of temperatures and hence are not visible in Fig.5.2 (a). On the other hand, the magnetization of $Ni_{0.25}Mn_{2.75}Ga$ showed a strong dependence on the temperature in addition to a visible increase in the magnetic moment as compared to Mn_3Ga. The magnetic ordering temperature of this alloy, too is above 390 K. Another important feature to be noted is the large irreversibility between ZFC and FCC magnetization curves. The ZFC curve displays a broad peak centered at about 170 K. These signatures usually represent the presence of competing magnetic interactions often leading to a magnetic glassy ground state. A visible Hysteresis in the FCC and FCW curves hints at a first-order transition. The possible implications of these observations are discussed later in the Chapter.

Fig. 5.2 (b) and (c) present isothermal magnetization curves for Mn_3Ga and $Ni_{0.25}Mn_{2.75}Ga$ alloys respectively. The antiferromagnetic spin alignment of HTA Mn_3Ga is confirmed from the linear, nearly zero hysteretic, and low magnitude magnetization loop (Fig. 5.2 (b)). However, on Ni doping (Fig. 5.2 (c)) though the alloy exhibits a linear non-saturating hysteresis curve, a small but distinct hysteresis is noted. Further, the magnetic moment also increases more than twice in comparison to Mn_3Ga, thus indi-

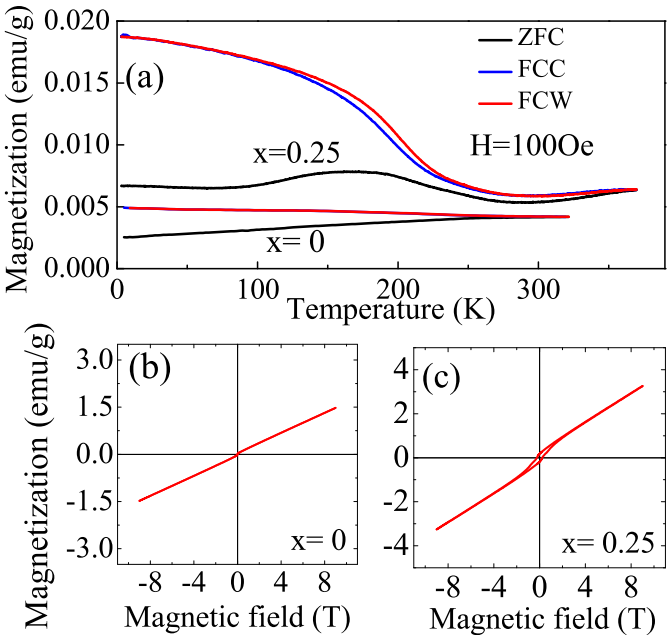

Figure 5.2: (a) Magnetization measurement as a function of temperature for $Mn_{3-x}Ni_xGa$ with $x = 0$ and 0.25 alloys in the applied field of 100 Oe. (b) and (c) Isothermal magnetization measurement for HTA $Mn_{3-x}Ni_xGa$ with $x = 0$ and $x = 0.25$ at T = 5 K in H = $\pm$9T field respectively.

cating the presence of ferromagnetic interactions. Extrapolating the magnetization curve from H = 9T gives a non-zero magnetization of 0.33 emu/g at 0 T. The increased moment value on Ni substitution in Mn_3Ga can be assigned to the increase in the number of electron count. However, the structural similarity of the two alloys and nearly constant lattice parameters fails to provide any direct explanation for the observed ferromagnetic interactions in this Ni-substituted Mn_3Ga alloy.

As the magnetic interactions in these alloys are dependent on structural interactions, the local environment of Ni, Mn, and Ga metal atoms in the HTA Mn_3Ga and $Ni_{0.25}Mn_{2.75}Ga$ were investigated using EXAFS spectroscopy. EXAFS recorded at 100 K at both Mn K edge and Ga K edge were fitted simultaneously in the R range of 1 Å to 3 Å and k range of 3 Å^{-1} to 12 Å^{-1} to a disordered Cu_3Au-type crystal structural model.

The scattering paths for the proposed model were formulated by taking into consideration the fact that every Mn/Ga absorber atom always encounters the (75 at% of Mn + 25 at% of Ga) atoms. The coordination number for each path was kept fixed to its value obtained for the proposed crystal structure. The fitting procedure resulted in good fits with reliable fitting parameters as can be seen from Fig. 5.3 and Table 5.2 respectively.

Next, the Mn and Ga K-edge EXAFS data for HTA $Ni_{0.25}Mn_{2.75}Ga$ were also fitted simultaneously by employing a similar approach as above. However, the procedure did not result in a good fit. Good fits to the Mn and Ga EXAFS could be obtained only after relaxing the constraint of equal Mn-Mn, Mn-Ga, and Ga-Ga bond distances. These fits to the FT magnitudes at Mn and Ga K edge are presented in Figs. 5.3 (c) and (d). Table 5.2 provides a listing of nearest neighbour and next nearest neighbour bond distances and their mean square disorder for $Ni_{0.25}Mn_{2.75}Ga$. As can be seen from the tabulated values, the nearest neighbour Ga-Ga and the next nearest Ga-Mn distance are distinctly smaller than the model values of those of corresponding bond distances in Mn_3Ga. The smaller Ga bond distances appear to be compensated by larger Mn-Mn bond distances.

Next, the Ni K edge data for HTA $Ni_{0.25}Mn_{2.75}Ga$ was fitted to the same structural model used for the simultaneous fitting of its Mn and Ga K edges. However, the model did not fit the data well. It should be noted that the substituted Ni in disordered Mn_3Ga can replace either by Mn or Ga; thus, both Mn and Ga can be the nearest neighbour. So the magnitude of FT of Ni EXAFS should be similar to Mn and Ga EXAFS. Comparing the FT magnitudes of EXAFS of Mn and Ga with Ni shown in Fig. 5.4, illustrates that

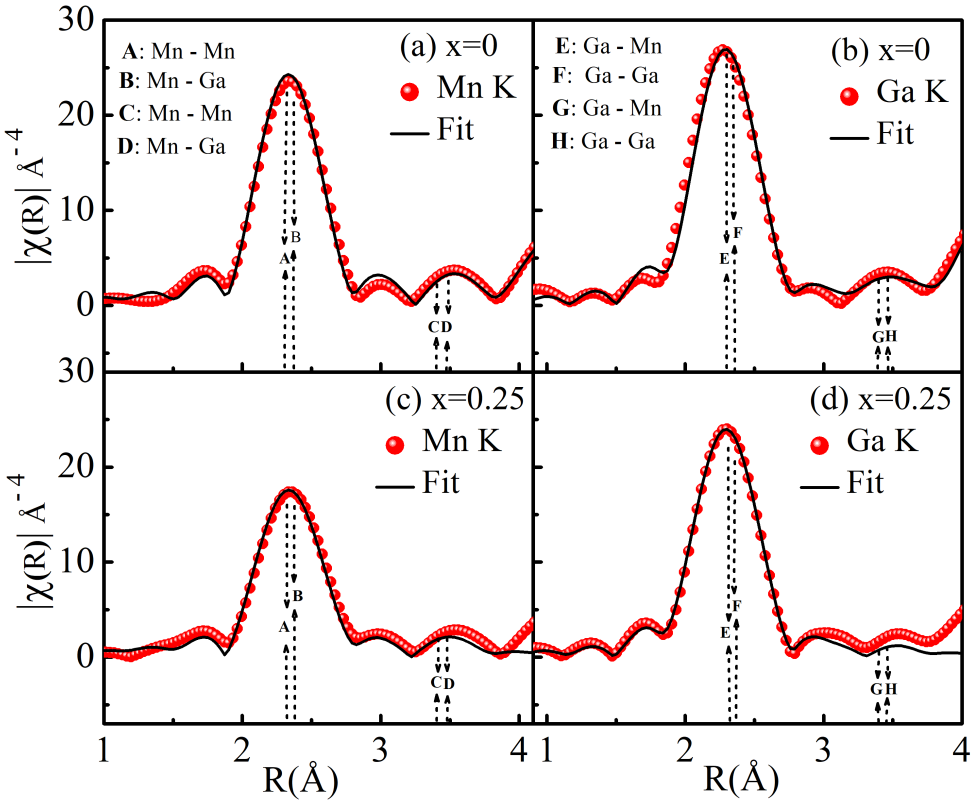

Figure 5.3: Best fits for Fourier transform magnitudes of k^3 weighted EXAFS at the Mn and Ga K edges in HTA $Mn_{3-x}Ni_xGa$ ($x = 0$ and 0.25). The plots are not corrected for phase shifts introduced by the absorber and the scatterer, and hence the peak appears at a lower R-value in the figure.

Table 5.2: Estimated bond distances (R) and thermal mean square distortion in bond distances (σ^2) values deduced from the concurrent fitting of Mn and Ga K edge EXAFS for HTA Mn_3Ga and $Ni_{0.25}Mn_{2.75}Ga$ alloys recorded at 100 K. Numbers in parentheses delegate the uncertainty in the end digits of the tabulated values.

Bond Type	R_{eff}(Å)	R(Å)	σ^2(Å^2)	R(Å)	σ^2(Å^2)
		x =0		x =0.25	
		Mn K EXAFS			
Mn-Mn	2.67	2.639(6)	0.008(1)	2.657(9)	0.002(1)
Mn-Ga	2.67	2.639(6)	0.002(1)	2.656(5)	0.006(1)
Mn-Mn	3.78	3.731(9)	0.015(6)	3.740(41)	0.007(5)
Mn-Ga	3.78	3.731(9)	0.006(6)	3.619(28)	0.015(4)
		Ga K EXAFS			
Ga-Ga	2.67	2.639(6)	0.006(4)	2.523(212)	0.031(29)
Ga-Mn	2.67	2.639(6)	0.007(2)	2.656(5)	0.004(2)
Ga-Ga	3.78	3.731(9)	0.011(38)	3.767(26)	0.006(1)
Ga-Mn	3.78	3.731(9)	0.015(21)	3.619(28)	0.015(4)

the peak in Ni EXAFS is ~ 0.04 Å lower than that in Mn, whereas ~ 0.02 Å higher than that in Ga EXAFS. This indicates a substantial change in the local environment of Ni as compared to Mn or Ga. Besides, the lower values of Ni-Mn/Ga bond distance compare well with the Heulser structure of Ni_2MnGa.[24] Therefore, the Ni EXAFS was modeled by including nearest neighbour correlations belonging to cubic disordered Cu_3Au structure (identified with subscript C) and those belonging to the Heusler $L2_1$ structure (identified with subscript H). This model resulted in a very good fit hinting at the formation of structural defects around Ni atoms in $Ni_{0.25}Mn_{2.75}Ga$. The resultant fit to the Ni EXAFS data is presented in Fig. 5.5, and the parameters obtained are listed in Table 5.3.

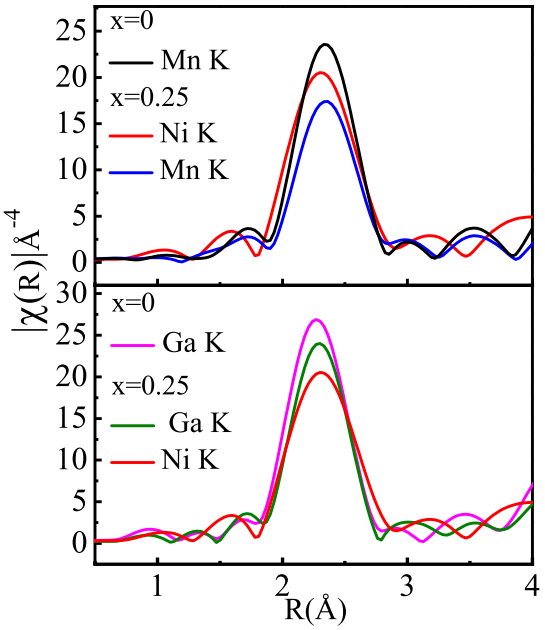

Figure 5.4: Comparison between Fourier transform magnitudes of k^3 weighted Mn and Ni EXAFS for HTA Mn_3Ga and $Ni_{0.25}Mn_{2.75}Ga$.

Segregation of structural defect is known to induce phase separation upon temper annealing.[16,25,26] Such phase separation is observed in several families of Mn-rich alloys

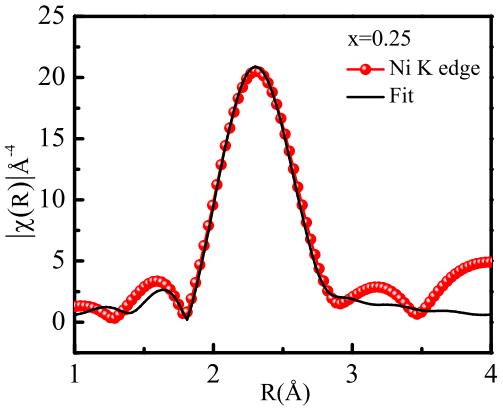

Figure 5.5: Best fits for the Fourier transformed magnitudes of k^3 weighted Ni K EXAFS for $Ni_{0.25}Mn_{2.75}Ga$.

like $Ni_2Mn_{2-x}Z_x$,[25] Mn_2NiSn[16] and Mn_2NiGa.[27] Mn_3Ga is known to undergo a structural transformation from a disordered cubic phase to a tetragonal $D0_{22}$ phase on annealing at the temperature of about 400°C, where the two cubic antiferromagnetic cells with a random distribution of Mn and Ga atoms get transforms into single tetragonal ferrimagnetic unit cell.[1] It is therefore interesting to see if a low-temperature annealing of cubic $Ni_{0.25}Mn_{2.75}Ga$ will lead to a structural phase transition or a phase separation or both.

Table 5.3: Obtained value of bond distances (R) and mean square disorder in bond distances (σ^2) for Ni edge EXAFS data fitting at 100 K. Figures in parentheses designate uncertainty in the ending digits.

Bond Type	R_{eff}(Å)	R (Å)	σ^2(Å^2)
		x=0.25	
Ni K EXAFS			
Ni_C-Mn	2.67	2.644(15)	0.005(3)
Ni_C-Ga	2.67	2.644(15)	0.005(3)
Ni_H-Ga	2.55	2.471(427)	0.019(34)
Ni_H-Mn	2.55	2.471(427)	0.019(34)

Accordingly, the HTA Mn_3Ga and $Ni_{0.25}Mn_{2.75}Ga$ alloys were annealed at 400°C (referred to as low-temperature annealed or LTA alloys) followed by furnace cooling and

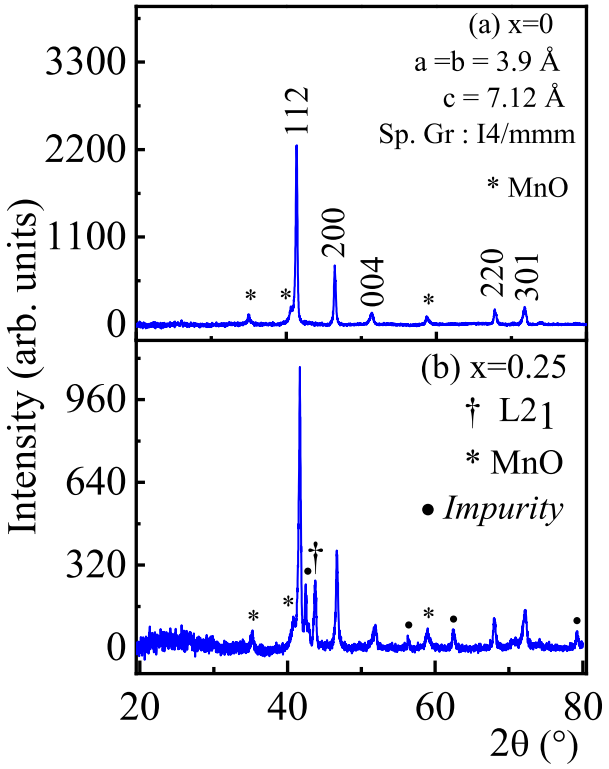

Figure 5.6: XRD patterns for LTA (a) Mn_3Ga and (b) $Ni_{0.25}Mn_{2.75}Ga$.

were then characterized for their structural and magnetic properties. Fig. 5.6 depicts the recorded XRD patterns for LTA Mn_3Ga and $Ni_{0.25}Mn_{2.75}Ga$ at room temperature. From the recorded patterns it is observed that the annealing of HTA Mn_3Ga had completely transformed its disordered Cu_3Au-type cubic structure to $D0_{22}$ tetragonal with space group $I4/mmm$. The Le Bail fitting analysis of its XRD pattern has confirmed its lattice parameters to be a = b = 3.90 Å and c = 7.11 Å which is in accordance with the ones outlined in literature.[1,28] On the other hand, the 400°C annealing of $Ni_{0.25}Mn_{2.75}Ga$ have resulted in a phase transformation from cubic to $D0_{22}$ tetragonal phase along with additional impurity phases. The additional phases consist of a Heusler phase, MnO, and a minor impurity phase. The obtained parameters for tetragonal $D0_{22}$ phase of

$Ni_{0.25}Mn_{2.75}Ga$ are a = b = 3.89 Å and c = 7.05 Å.

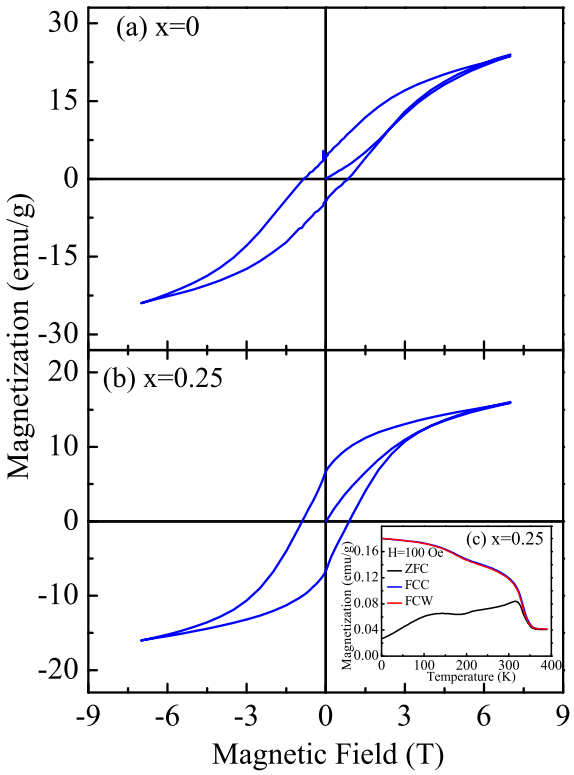

Figure 5.7: (a) and (b) Isothermal magnetization for LTA $Mn_{3-x}Ni_xGa$ with $x = 0$ and $x = 0.25$ alloys respectively, at T = 5 K in H = ±7T field. (c) Temperature-dependent magnetization for LTA $Ni_{0.25}Mn_{2.75}Ga$ in H = 100 Oe applied field during ZFC, FCC, and FCW cycles.

The magnetic isotherms for LTA Mn_3Ga and $Ni_{0.25}Mn_{2.75}Ga$ recorded at 5 K in the field of ±7T are displayed in Fig. 5.7 (a) and (b) respectively. The isotherm for LTA Mn_3Ga displays the non-saturating hysteresis loop with a coercivity of 8.5 KOe, indicating its hard magnetic nature. The LTA $Ni_{0.25}Mn_{2.75}Ga$ displays a high saturation magnetic moment in addition to the broad hysteresis loop of 8.81 KOe which is comparable to that of Mn_3Ga. The elevated saturation magnetization of the hysteresis loop of LTA $Ni_{0.25}Mn_{2.75}Ga$ as compared to LTA Mn_3Ga can be due to the combined outcome of the co-existing ferromagnetic Ni-rich Heusler phase and the ferrimagnetic state of tetrago-

nal Mn_3Ga LTA $Ni_{0.25}Mn_{2.75}Ga$. Besides, the presence of the $L2_1$ Heusler phase in LTA $Ni_{0.25}Mn_{2.75}Ga$ becomes obvious from its temperature-dependent magnetization measurement recorded in a magnetic field 100 Oe shown in the inset of Fig. 5.7. The curves show an abrupt decline in magnetization at around T $\sim$ 350 K which coincides with the ferromagnetic ordering temperature of Ni-Mn-Ga Heusler alloys. It should be noted that this temperature is much lower than the ordering temperature T_C= 730 K proposed for tetragonal $D0_{22}$ Mn_3Ga phase.[1]

5.3 Discussion

The HTA Mn_3Ga is an antiferromagnet that crystallizes into a disordered Cu_3Au-type cubic structure.[4] The substitution of Ni in Mn_3Ga leads to an increase in the magnetic moment and weak ferromagnetism. The EXAFS studies on $Ni_{0.25}Mn_{2.75}Ga$ have spotted structural distortions in the local environment of its constituent atoms which are identified to be mainly because of the locally formed Ni-rich $L2_1$ Heusler defects within the Mn_3Ga-type lattice. Further, the first order transition observed T $\sim$ 200 K and the weak ferromagnetism seen in HTA $Ni_{0.25}Mn_{2.75}Ga$ affirms the formation of ferromagnetic Ni_2MnGa type defects in the antiferromagnetic lattice of Mn_3Ga.[29] The low-temperature annealing of this alloy confirms the formation Ni-Mn-Ga Heusler-like entities in $Ni_{0.25}Mn_{2.75}Ga$.

Such phase-separated magnetic systems can exhibit interesting properties due to the strong interaction between the two magnetic phases.[30–33] One such example is $Mn_{3-x}Ni_xGaC$ which phase separates into Mn_3GaC antiperovskite phase and Ni_2MnGa

Heusler phase. The interaction between the two phases leads to an arrest of the ferromagnetic state of Mn_3GaC.[34] To check if such interaction also exists between the locally segregated ferromagnetic Heusler entity and the major antiferromagnetic phase, we performed ZFC and FC isothermal magnetization measurements at 300 K. The FC measurements were performed by cooling the sample in a 5 T magnetic field. These results are plotted in Fig. 5.8.

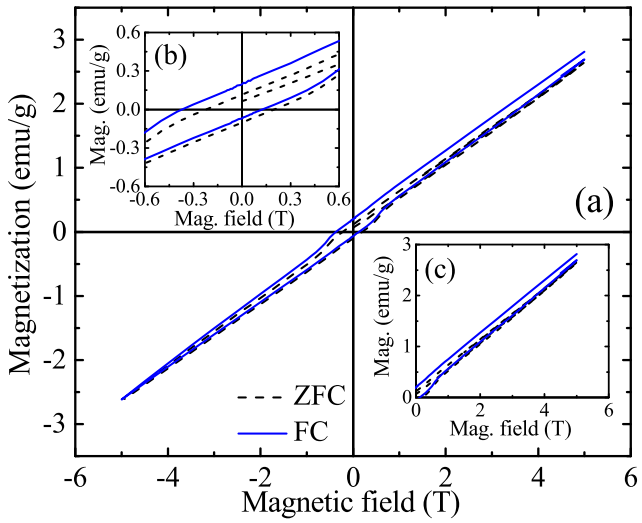

Figure 5.8: (a) Zero field cooled and Field cooled hysteresis loop measured at 300 K in HTA $Ni_{0.25}Mn_{2.75}Ga$. Inset (b) and (c) show exchange bias and open hysteresis loop formed in HTA $Ni_{0.25}Mn_{2.75}Ga$ respectively.

Two differences between the FC and ZFC loops can be noticed immediately. The FC loop is shifted to the left, indicating the presence of an exchange bias (see Fig. 5.8 (b)) and secondly, the magnetization value does not return back to the starting value of the hysteresis loop, symbolizing a kinetic arrest of the ferromagnetic phase (see Fig. 5.8 (c)). Usually, in such cases, the arrested ferromagnetic state belongs to the major

phase. However, Mn_3Ga is not known to show any ferromagnetic interactions in the cubic phase. Hence, the ferromagnetic interactions seen in M(T) or M(H) of $Ni_{0.25}Mn_{2.75}Ga$ are not just from the defect phase but also from the major phase. The changes in the local structure of Mn and Ga drive these ferromagnetic interactions which are arrested during field-cooled measurements.

5.4 Conclusion

In conclusion, Ni-doped Mn_3Ga displays the presence of ferromagnetic interactions as a result of local structural distortions induced by Ni. The weak ferromagnetism in HTA $Ni_{0.25}Mn_{2.75}Ga$ emerges from the locally formed Ni_2MnGa-type Heusler inclusion within the antiferromagnetic Mn_3Ga-type lattice. The ferromagnetic defect phase and the antiferromagnetic major phase interact with each other in such a way as to induce ferromagnetic interactions in the cubic antiferromagnetic phase leading to the observation of the kinetic arrest and the exchange bias.

References

[1] B. Balke, G. H. Fecher, J. Winterlik, and C Felser. *Applied Physics Letters*, 90(15):152504, 2007.

[2] H. Niida, T. Hori, and Y. Nakagawa. *Journal de Physique Colloques*, 49(C8):C8–173–C8–174, 1988.

[3] H. Niida, T. Hori, H. Onodera, Y. Yamaguchi, and Y. Nakagawa. *Journal of Applied Physics*, 79(8):5946–5948, 1996.

[4] P. Kharel, Y. Huh, N. Al-Aqtash, V. R. Shah, R. F. Sabirianov, R. Skomski, and D. J. Sellmyer. *Journal of Physics: Condensed Matter*, 26(12):126001, 2014.

[5] H. C. Kandpal, G. H. Fecher, and C. Felser. *Journal of Physics D: Applied Physics*, 40(6):1507–1523, 2007.

[6] S. Wurmehl, H. C. Kandpal, G. H. Fecher, and C. Felser. *Journal of Physics: Condensed Matter*, 18(27):6171–6181, 2006.

[7] S. Fukami, V. O. Lorenz, and O. Gomonay. *Journal of Applied Physics*, 128(7):070401, 2020.

[8] V. Baltz, A. Manchon, M. Tsoi, T. Moriyama, T. Ono, and Y. Tserkovnyak. *Reviews of Modern Physics*, 90(57):015005, 2018.

[9] Z. Liu, Z. Feng, H. Yan, X. Wang, X. Zhou, P. Qin, H. Guo, R. Yu, and C. Jiang. *Advanced Electronic Materials*, 5(7):1900176, 2019.

[10] H. Yan, Z. Feng, P. Qin, X. Zhou, H. Guo, X. Wang, H. Chen, X. Zhang, H. Wu, and C. Jiang. *Advanced Materials*, 32(12):1905603, 2020.

[11] H. Kurt, K. Rode, H. Tokuc, P. Stamenov, M. Venkatesan, and J. M. D. Coey. *Applied Physics Letters*, 101(23):232402, 2012.

[12] Hyun-Woo Bang, Woosuk Yoo, Youngha Choi, Chun-Yeol You, Jung-Il Hong, Janez Dolinšek, and Myung-Hwa Jung. *Current Applied Physics*, 16(1):63–67, 2016.

[13] Won Seok Yun, Gi-Beom Cha, In Gee Kim, S H Rhim, and Soon Cheol Hong. *Journal of Physics Condensed Matter*, 24:416003, 2012.

[14] M. Stamenova, P. Stamenov, F. Mahfouzi, Q. Sun, N. Kioussis, and S. Sanvito. *Physical Review B*, 103, 03 2021.

[15] G. D. Fuchs, N. C. Emley, I. N. Krivorotov, P. M. Braganca, E. M. Ryan, S. I. Kiselev, J. C. Sankey, D. C. Ralph, R. A. Buhrman, and J. A. Katine. *Applied Physics Letters*, 85(7):1205–1207, 2004.

[16] S. V. Malik, E. T. Dias, A. K. Nigam, and K. R. Priolkar. *Journal of Physics D: Applied Physics*, 55(16):165002, 2022.

[17] S. Itigi, S. Matteppanavar, S. Rayaprol, and B. Angadi. *Physica B: Condensed Matter*, 561, 03 2019.

[18] C. Song, Y. You, X. Chen, X. Zhou, Y. Wang, and F. Pan. *Nanotechnology*, 29(11):112001, 2018.

[19] K. Wang, V. Bheemarasetty, J. Duan, S. Zhou, and G. Xiao. Perspectives on antiferromagnetic spintronics. 2022.

[20] R. M. White, R. J. Nemanich, and C. Herring. *Physical Review B*, 25(3):1822, 1982.

[21] T. H. Kim, P. Grünberg, S. H. Han, and B. Cho. *Scientific Reports*, 6(1):1–8, 2016.

[22] S. Nakatsuji, N. Kiyohara, and T. Higo. *Nature*, 527(7577):212–215, 2015.

[23] J. Yan, X. Luo, H. Y. Lv, Y. Sun, P. Tong, W. J. Lu, X. B. Zhu, W. H. Song, and Y. P. Sun. *Applied Physics Letters*, 115(10):102404, 2019.

[24] P. A. Bhobe, K. R. Priolkar, and P. R. Sarode. *Physical Review B*, 74(8):224425, 2006.

[25] A. Cakir, M. Acet, and M. Farle. *Scientific Reports*, 6:28931, 2016.

[26] A. Cakir, M. Acet, U. Wiedwald, T. Krenke, and M. Farle. *Acta Materialia*, 127:117–123, 2017.

[27] S. V. Malik, E. T. Dias, V. Srihari, P. D. Babu, and K. R. Priolkar. *Intermetallics*, 148:107613, 2022.

[28] J. Winterlik, B. Balke, G. H. Fecher, C. Felser, M. C. M. Alves, F. Bernardi, and J. Morais. *Physical Review B*, 77(5):054406, 2008.

[29] P. J. Webster. *Contemporary Physics*, 10(6):559–577, 1969.

[30] M. K. Chattopadhyay, S. B. Roy, and P. Chaddah. *Physical Review B*, 72(18):180401, 2005.

[31] S. B. Roy, M. K. Chattopadhyay, M. A. Manekar, K. J. S. Sokhey, and P. Chaddah. *Bulletin of Materials Science*, 29:623–631, 2006.

[32] R. Kainuma, W. Ito, R. Y. Umetsu, K. Oikawa, and K. Ishida. *Applied Physics Letters*, 93(9):091906, 2008.

[33] A. K. Nayak, M. Nicklas, S. Chadov, P. Khuntia, C. Shekhar, A. Kalache, M. Baenitz, Y. Skourski, V. K. Guduru, and A. Puri. *Nature Materials*, 14(7):679–684, 2015.

[34] Ö. Çakır, M. Acet, M. Farle, E. Dias, and K. Priolkar. *Journal of Magnetism and Magnetic Materials*, 390:96–99, 2015.

Chapter 6

Effect of Ni substitution on the magnetic and electronic ground state of Mn_3Sn.

6.1 Introduction

The antiferromagnetic Mn_3Sn is one of the widely studied topological Weyl semimetals for its excellent spintronic and topological characteristics.[1,2] Recently, the experimental community has reported a large anomalous Hall effect in this system, originating at its non-vanishing Weyl nodes in the k-space. To date, substantial theoretical work has been accomplished to understand the role of its fundamental magnetic structure in determining its band structure topology. These theoretical studies have perceived an eventuality of the acute interplay between its crystal and magnetic structure symmetries that can lead to the unfolding of its variety of topological phases via Berry phase curvature depiction. Additionally, the spacing between the Weyl nodes and their emergence in k-space, which is responsible for time-reversal symmetry breaking, is primarily dependent on the underlying crystal or/and magnetic spin structure.[3–11] Thus, the subtle manipulations of these aspects can make its Weyl nodes move in the Brillouin zone or can make them vanish.

Ultimately, it leads to manipulating its Hall signal strength and sometimes may even lead to a crossover from anomalous Hall effect to the topological Hall effect.[12–14] Thus, adjusting the positioning of Weyl nodes in Mn_3Sn by modifying its magnetic spin texture grants a promising way to modify its Hall contribution.[15]

Crafting the magnetic spin structure of interest in Mn_3Sn can be challenging since it is critically dependent on the subtle balancing between various interactions such as Dzyaloshinskii-Moriya, Heisenberg exchange, and the magnetocrystalline anisotropy.[16–18] Several studies have suggested various external perturbations that can control the dynamical equilibrium of Mn_3Sn spin structure such as magnetic field,[1] temperature,[2] pressure,[12,19] residual strain,[20] elemental substitution (impurity doping),[21] structural defects, chemical disorder, etc. These parameters have the ability to set the Mn_3Sn system into a novel magnetic spin state with novel dynamical equilibria. Besides these external parameters, its magnetic order is also known to be sensitively dependent on its accurate elemental composition (i.e., the Mn to Sn ratio)[1,2,22] and/or sample preparation procedure.[23–26] Thus, these findings exemplify the guiding parameters to manipulate and control the type of magnetic spin structure in Mn_3Sn.

One of the distinct outcomes of the application of an external magnetic field in Mn_3Sn is its weak ferromagnetism, which results from the subtle breaking of its triangular spin state symmetry, which leads to the emergence of an weak magnetic moment.[1,27] Although this delicate symmetry breaking does not affect its transport properties drastically, it does cause a disturbance in the band structure; for instance, one can expect a moderate

alteration of the mirror image of the Weyl nodes from its original location.[1,27]

The above discussion highlights a connectedness of the topology of Mn_3Sn with its crystal or/and magnetic spin structure. Besides, it also showcases one of the significant features of its inverse triangular spin structure, the parasitic weak ferromagnetism. These studies point towards the fact that the Mn-Mn distance in Mn_3Sn can be substantially changed through suitable controllable parameters, which can substantially change its pristine magnetic ground and its parasitic weak ferromagnetism.[1,28] Motivated by this literature overview, the current study focuses on tuning the antiferromagnetic ground state of Mn_3Sn at room temperature via suitable elemental substitution. We propose to prepare the $Mn_{3-x}Ni_xSn$ polycrystalline samples with ($x = 0$ and 0.25), using the arc melting technique and to investigate the evolution of their magnetic, transport, and the magneto-transport properties.

6.2 Results

The chemical composition for $Mn_{3-x}Ni_xSn$ with $x = 0$, and 0.25 was found to be $Mn_{3.18}Sn_{0.82}$ and $Ni_{0.28}Mn_{2.87}Sn_{0.85}$ respectively. These compositions were estimated by averaging the elemental fractions of the constituent elements over 3 points on the sample and over a sample area of 200 μm^2. The final attained compositions were close to the nominal. However, they had an excess of Mn. The excess of Mn was deliberately added to the alloys at the time of their preparation to avoid contamination with Mn_2Sn impurity.[25]

Fig. 6.1 (a) and (b) represents the powder XRD patterns recorded for Mn_3Sn and

$Ni_{0.25}Mn_{2.75}Sn$ respectively at room temperature. The Rietveld refinement of the XRD pattern of Mn_3Sn have established it to be largely single phasic with Ni_3Sn-type $D0_{19}$ hexagonal crystal structure (Sp.Gr: $P6_3/mmc$). This analysis also notified the presence of less than 1% Mn_2Sn secondary impurity phase. Here, it should be noted that the finding of Mn_2Sn impurity phase along with Mn_3Sn major phase has been reported earlier.[29] On the other hand, the Ni substituted Mn_3Sn is found to be largely single phasic with $D0_{19}$ structure and no impression of the secondary phases. The best fit assigned cell parameters to the $D0_{19}$ phase of Mn_3Sn and $Ni_{0.25}Mn_{2.75}Sn$ are $a = 5.6835$ Å, $c = 4.5382$ Å and $a = 5.6445$ Å, $c = 4.5097$ Å respectively, agreeing well with the previous reported studies.[19,29] Additionally, the structural analysis has also identified the presence of preferred orientation along (002) crystallographic plane of $D0_{19}$ structure both in Mn_3Sn and $Ni_{0.25}Mn_{2.75}Sn$. This preferred orientation is confirmed by comparing the relative intensities of theoretically calculated and experimentally observed peaks of the primary (201) peak with that of the preferentially oriented (002) peak.[30] Preferred orientation along the (002) direction was also included in the Rietveld refinement, and the refined curves are shown in Fig. 6.1.

Fig. 6.2 (a) depicts the magnetization measurement as a function of temperature (M(T)) for Mn_3Sn in the applied magnetic field of 100 Oe in ZFC, FCC, and FCW modes. Below the $T_N \sim 420$ K, Mn_3Sn is reported to have a non-collinear, co-planar, inverse-triangular antiferromagnetic spin order featured by nearly ideal compensation of the Mn spins on a 2D kagome lattice.[21,31] It is known to undergo two distinct magnetic

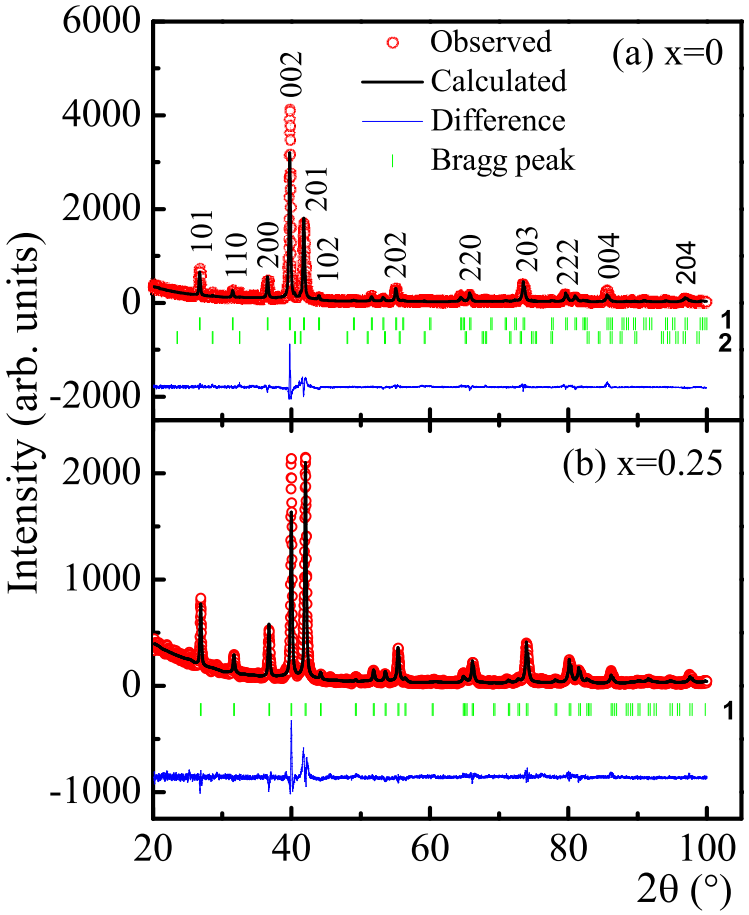

Figure 6.1: Powder x-ray diffraction profiles for (a) Mn_3Sn ($x = 0$) and (b) $Ni_{0.25}Mn_{2.75}Sn$ ($x = 0.25$) at room temperature. Structural phases recognized from Rietveld refinement analysis are specified by numerals, 1 - Mn_3Sn, 2 - Mn_2Sn.

transitions. First, from co-planar inverse-triangular spin structure as mentioned above to non co-planar helical spin structure at $T_t \sim 280$ K,[29] and then to spin glassy ferromagnetic spin structure at $T_g \sim 50$ K.[30] The M(T) represented in Fig 6.2 (a) displays both these transitions fairly well and manifests the eventuality of its reported magnetic transformations. Here, the first magnetic transition is observed at $T_t \sim 290$ K, identified from a noticeable drop in the ZFC, FCC, and FCW magnetization curves.[2,21,29,32] Following the drop at T_t, magnetization shows an increase with further decreasing temperature.

This is attributed to the stabilization of the helical spin structure. Following the rise in magnetization, the ZFC and the FC curves bifurcate which is speculated to be the onset of the spin-glassy state of the alloy.[31,33] Below 100 K, irreversibility between ZFC and FCC curves is observed due to the fully developed spin-glassy ferromagnetic state.[34]

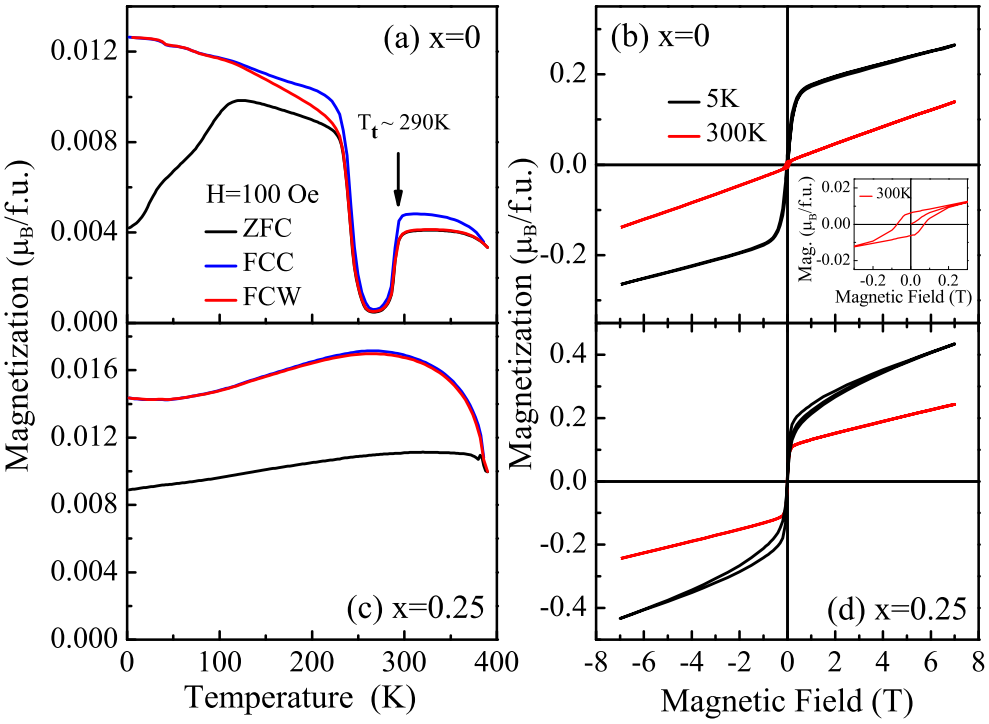

Figure 6.2: Magnetic property measurements for Mn_3Sn ($x = 0$) and $Ni_{0.25}Mn_{2.75}Sn$ ($x = 0.25$). (a) and (c) The magnetization measurement as a function of temperature at the applied field of 100 Oe in ZFC, FCC, and FCW modes. (b) and (d) Isothermal magnetization measurement at 300 K and 5 K.

Further, the magnetic nature of Mn_3Sn became apparent from its isothermal magnetization measurements (M(H)) recorded at 300 K and 5 K which are displayed in Fig. 6.2 (b). The M(H) loop for Mn_3Sn at 300 K illustrates a linear behavior with small but clear hysteresis at very low applied magnetic fields, confirming the existence of weak ferromagnetic interactions.[26,31,35] However, at 5 K, the alloy displays a non-linear loop with

higher saturation magnetization compared to that at 300 K. The observed weak ferromagnetism at 300 K is known to be parasitic to the triangular Mn spin structure laying on the Kagome lattice network.[18,26,31] It is a consequence of both the off-stoichiometric elemental composition of the alloy and the slight distortion in the Mn spin arrangement on the equilateral triangle towards their easy axis.

Fig. 6.2 (c) illustrates the recorded temperature-dependent magnetization for $Ni_{0.25}Mn_{2.75}Sn$. The substitution of Ni in Mn_3Sn seems to have modified its magnetic spin texture, as apparent from its increased magnetic moment compared to that in Mn_3Sn. Also, this substitution has led to either the vanishing of T_t transition or pushing it to a higher temperature greater than 390 K. These observed magnetic modifications become further evident from the isothermal magnetization measurement performed at 300 K and 5 K displayed in Fig. 6.2 (d). A non-linear nature of the M(H) loops at both temperatures, accompanied by an increase in magnetization especially at 300 K, distinctly points to the presence of ferromagnetic interactions in the alloy.

To probe the transport and the magneto-transport properties of Mn_3Sn and $Ni_{0.25}Mn_{2.75}Sn$, the resistivity and the Hall resistivity as a function of temperature were measured. Mn_3Sn shows an increase in resistivity with increasing temperature depicting metallic behavior, as illustrated in Fig. 6.3 (a). A small change in slope of the measured resistivity at $T_t \sim 290$ K depicts the magnetic T_t transition.[29] On the other hand, $Ni_{0.25}Mn_{2.75}Sn$ shows a small decrease in the resistivity with increasing temperature illustrated in Fig. 6.3 (c), akin to semiconductor-like. Any material can be called

a metal only if it possesses a finite value of resistance at zero temperature obtained by extrapolating its recorded resistivity trend to zero temperature. This is also true in the situation where the resistance decreases as the temperature increases.[36] Additionally, there are metals that are found to exhibit semiconductor-like resistivity much similar to our $Ni_{0.25}Mn_{2.75}Sn$.[37,38] Also, it should be noted that the recorded values of resistivities for both Mn_3Sn and $Ni_{0.25}Mn_{2.75}Sn$ at room temperature are of the same order of magnitude and much lower than the Mott-Ioffe-Regel limit of 308 $\mu\Omega$-cm for such systems.[14,39]

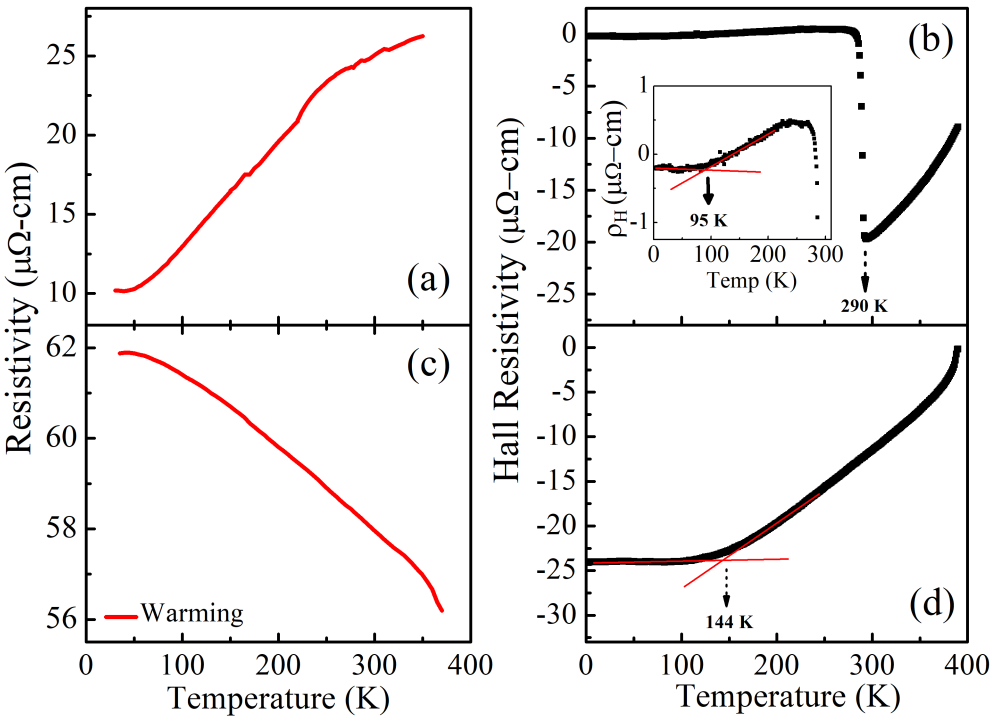

Figure 6.3: Transport and magneto-transport property measurements for Mn_3Sn ($x = 0$) and $Ni_{0.25}Mn_{2.75}Sn$ ($x = 0.25$). (a) and (c) Temperature-dependent resistivity measurement. (b) and (d) Temperature-dependent Hall resistivity measurement.

Fig. 6.3 (b) displays the Hall resistivity measurement as a function of temperature for Mn_3Sn. The recorded Hall resistivity shows an initial decrease with decreasing tempera-

ture, followed by a sudden increase at $T_t \sim 290$ K, and then saturates to a small value down to 5 K. The sudden change in the Hall resistivity ~ 290 K illustrates the first-order transition, consistent with the magnetic T_t transition. At low temperatures, the change in the slope of Hall resistivity ~ 95 K is identified as the transformation temperature to the spin glassy state.[9] It is interesting to note that the observed value of Hall resistivity for our polycrystalline Mn_3Sn, at T_t transition, is higher than those observed for single crystals.[2,21] On the other hand, $Ni_{0.25}Mn_{2.75}Sn$ shows a continuous decrease in Hall resistivity with decreasing temperature. At higher temperatures, no inconsistency is observed in the measured Hall resistivity curve. However, at low temperatures, a subtle change in the slope at ~ 144 K is seen which is suspected to be due to the reorientation of its spin alignment.[9,21] Also, such a continuous variation in Hall resistivity is fairly collateral with its M(T) behavior.

In Mn_3Sn, the anomalous Hall effect originates from its intrinsic non-zero Berry curvature at the Weyl nodes.[1] To have a close look at the contrasting behavior of Hall resistivity of $Ni_{0.25}Mn_{2.75}Sn$ as compared to pristine Mn_3Sn across T_t transition we compare the hysteresis in Hall resistivity (ρ_H(H)) and the magnetization (M(H)) at few temperatures between 350 K and 250 K.

The observed behavior of ρ_H(H) and M(H) at 350 K, 325 K, 300 K, 275 K, and 250 K across T_t transition for our polycrystalline Mn_3Sn illustrated in Fig. 6.4 is in good agreement with the earlier single crystal study.[2] The isothermal magnetization curves measured at 350 K, 325 K, and 300 K display distinct hysteresis in magnetization in the

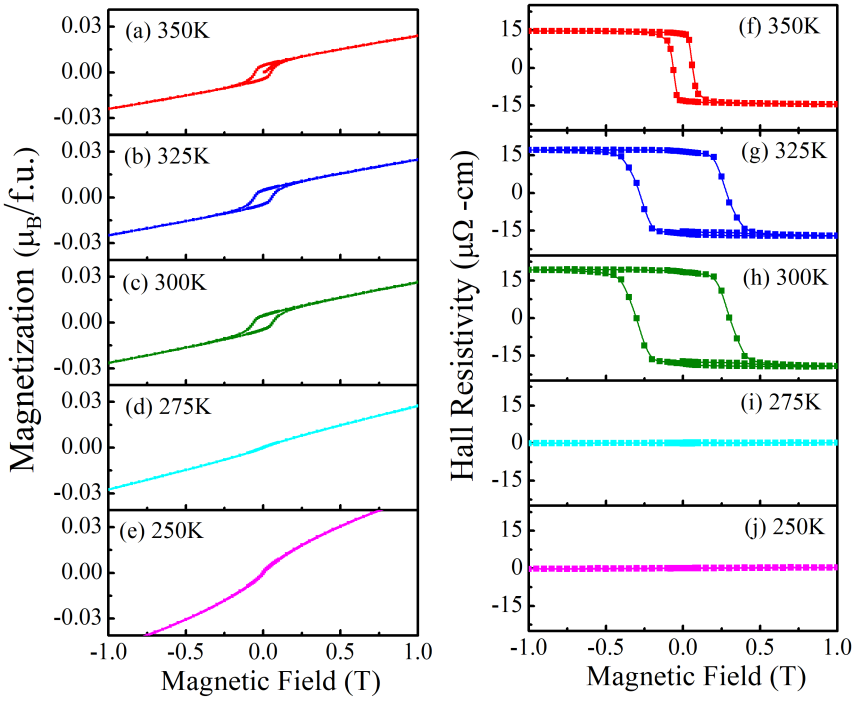

Figure 6.4: Isothermal magnetization and Hall resistivity measurements for Mn_3Sn at 350 K, 325 K, 300 K, 275 K, and 250 K.

low-field region. This hysteresis almost completely disappears at 275 K and 250 K ($T < T_t$) even though the magnetization curves display a small non-linearity. Similar behaviour is noted for ρ_H(H) with clear irreversibility and finite Hall resistivity at zero magnetic field is seen at all temperatures above T_t and their disappearance below this transition temperature.

The M(H) and ρ_H(H) for $Ni_{0.25}Mn_{2.75}Sn$ recorded at exactly the same temperatures are shown in Fig. 6.5. The M(H) loops are non-linear with negligible coercivity and appreciable retentivity at all temperatures. A similar behaviour is reproduced by ρ_H(H) displaying a significant hysteresis and large Hall resistivity at zero magnetic field. The

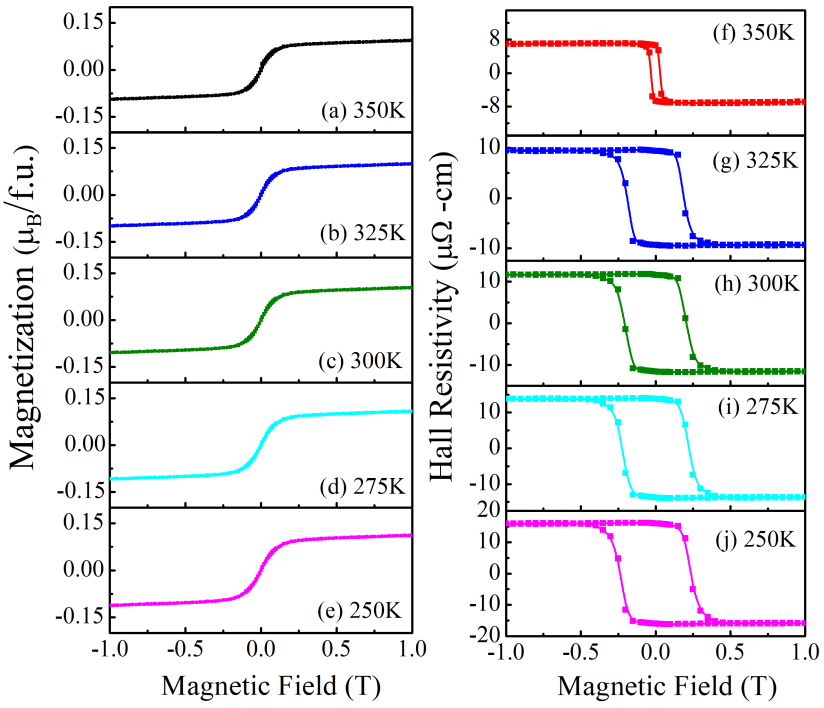

Figure 6.5: Isothermal magnetization and Hall resistivity measurements for $Ni_{0.25}Mn_{2.75}Sn$ at 350 K, 325 K, 300 K, 275 K, and 250 K.

observation of Hall hysteresis down to 250 K is quite surprising considering the absence of T_t below 250 K in $Ni_{0.25}Mn_{2.75}Sn$.

To trace the thermal evolution of the magnetic ground states both in Mn_3Sn and $Ni_{0.25}Mn_{2.75}Sn$, neutron diffraction (ND) patterns were recorded at various temperatures between 300 K to 3 K. First, the recorded ND data was visually inspected. Fig. 6.6 presents a comparative plot of the ND patterns recorded at 300 K, 290 K, 280 K, and 270 K across T_t transition. Such a comparative data plotting showed a clear evolution of magnetic reflection identified at $\sim 21^\circ$ below T_t (marked using a red arrow). This peak progression depicts the magnetic transformation from co-planar, inverse-triangular

spin structure (at 300 K) to non-coplanar helical spin structure (at 280 K) across T_t transition.[34]

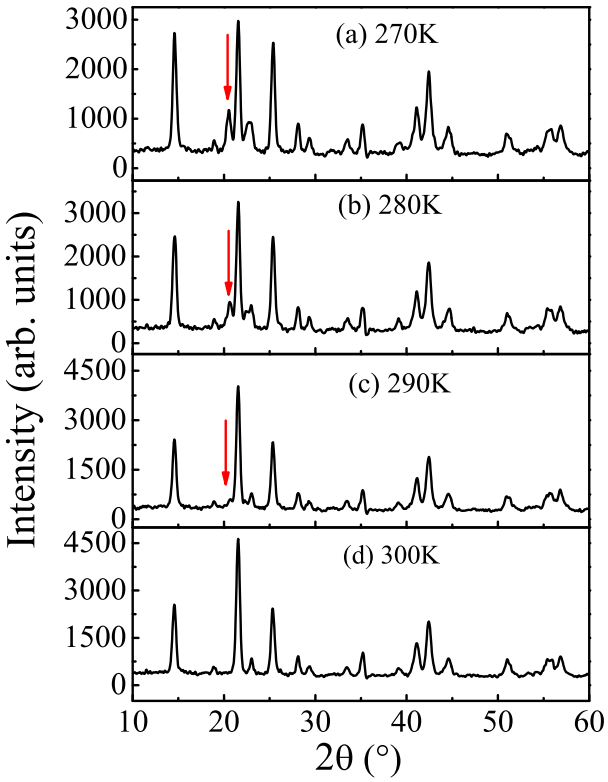

Figure 6.6: Neutron diffraction patterns recorded at 300 K, 290 K, 280 K, and 270 K for Mn_3Sn across T_t transition.

To confirm this further, the Rietveld refinement of ND data at 300 K was carried out using Fullprof suite. Here, while the crystal structure was refined using hexagonal $D0_{19}$ structure, the co-planar inverse-triangular spin structure (Sp.Gr: Cmc′m′) with the wave vector k = (0, 0, 0) and a negative vector (anti-chiral) spin chirality was used for refining the magnetic structure.[23,29,40,41] The Rietveld analysis of the 300 K data confirmed its structure as proposed above. The obtained magnetic spin structure is shown in Fig. 6.7.

Further, taking a clue from the previous literature reports on the magnetic structure

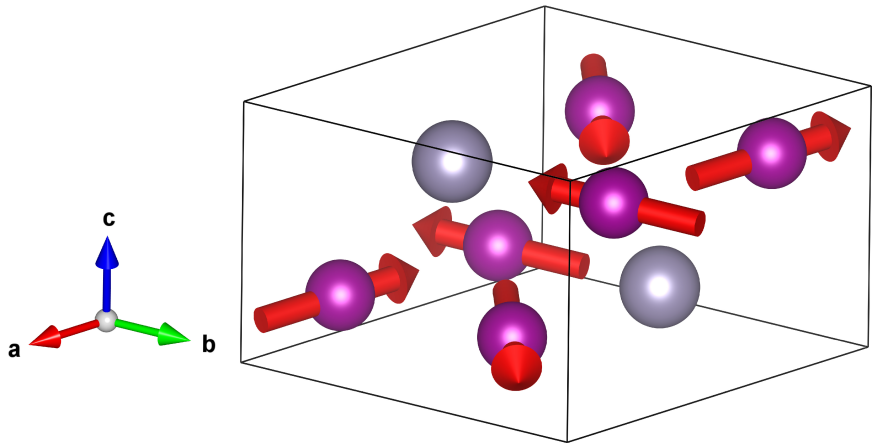

Figure 6.7: Magnetic structure of Mn_3Sn obtained from the Rietveld refinement of ND data at 300 K.

of Mn_3Sn,[29] the 290 K data was Le Bail fitted to a non-coplanar helical spin structure with $P6_322.1'(00g)$-$h00s$ magnetic superspace group, having a modulation vector of q = (0, 0, 1/10) using Jana 2020 software. This model represents a spin density wave that defines the amplitude and the phase of the Mn moments that frequently changes.[29] The transverse component residing in the xy-plane is helical, whereas the component lying about the z-axis direction is a spin-density wave. Figs. 6.8 (a) and (b) illustrates the Le Bail fitting of ND patterns of Mn_3Sn at 50 K and 220 K respectively.

Fig. 6.9 plots the thermal evolution of magnetic modulation wave vectors obtained from the ND fitting analysis and the magnetization as a function of temperature for Mn_3Sn. Based on the type of vector obtained from the ND fitting analysis, the magnetism in Mn_3Sn can be approximately categorized into four sections. Above 290 K, it has a single k = (0, 0, 0) vector. Between 290 K and 240 K there are two vectors, q_1 and q_2. The values of q_1 and q_2 were estimated to be (0.125±1) and (0.092±1). Further, the values of

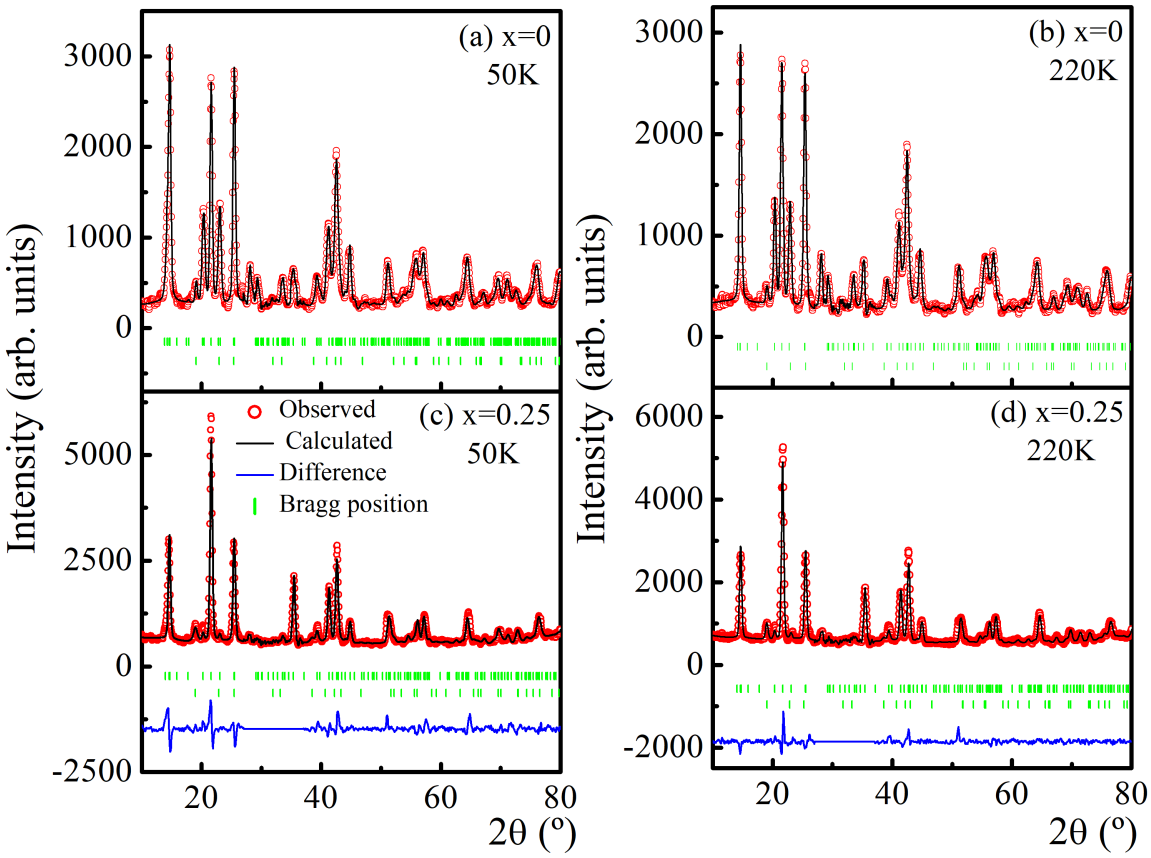

Figure 6.8: Refined neutron diffraction patterns at 220 K and 50 K using non-coplanar helical magnetic structural.

q_1 and q_2 between 230 K and 200 K become equal with $q_1 = q_2 = (0.113\pm1)$, and finally, between 175 K and 3 K, q_1 and q_2 acquire values of (0.124 ± 1) and (0.097 ± 1) respectively. Our findings of the modulation vectors are in accordance with the literature[29]

For $Ni_{0.25}Mn_{2.75}Sn$, the entire ND data was visually compared with the known magnetic structures of Mn_3Sn.[13,29,31] This comparison indicated the presence of a non-coplanar helical spin structure in $Ni_{0.25}Mn_{2.75}Sn$ at all temperatures below room temperature. Thus, the ND data of $Ni_{0.25}Mn_{2.75}Sn$ were Rietveld refined using the non-coplanar

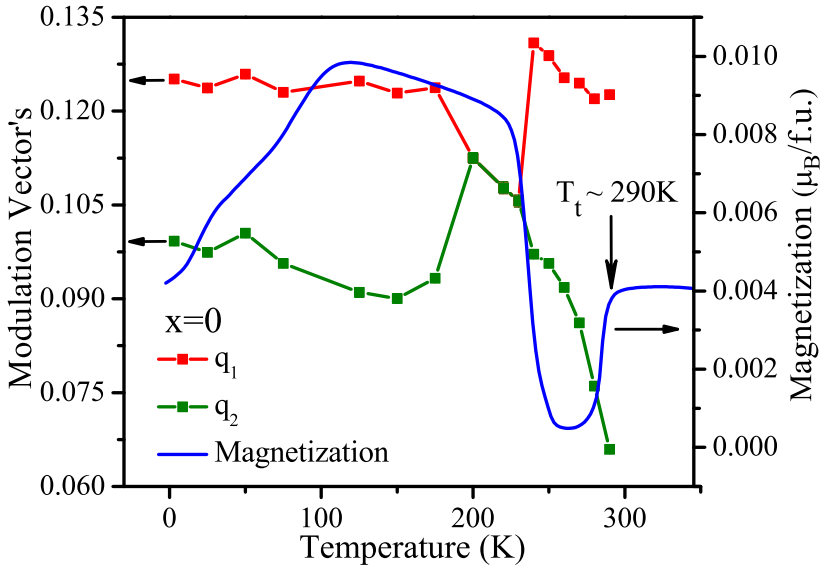

Figure 6.9: The thermal evolution of magnetic modulation wave vector and the magnetization as a function of temperature for Mn_3Sn.

helical spin structure having a $P6_322.1'(00g)$-$h00s$ magnetic superspace group with (0, 0, 1/10) modulation vector, by employing Jana 2020 software. The refinement confirmed the magnetic structure as proposed over the entire temperature range with a single magnetic modulation vector q = (0.117±6). Figs. 6.8 (c) and (d) respectively illustrates the refined ND patterns for $Ni_{0.25}Mn_{2.75}Sn$ at 50 K and 220 K. Fig. 6.10 displays the refined magnetic superstructure of $Ni_{0.25}Mn_{2.75}Sn$ with ten unit cells at 220 K. Fig. 6.11 puts forward the thermal evolution of magnetic modulation wave vectors obtained from the ND refinement analysis and the magnetization as a function of temperature for $Ni_{0.25}Mn_{2.75}Sn$.

The alteration of in-plane Mn-Mn distances of Mn_3Sn is known to modify its magnetic spin alignment.[19] Thus, probing the local structure of Mn_3Sn and $Ni_{0.25}Mn_{2.75}Sn$ can turn out crucial in understanding the peculiarities observed in their magnetic structures.

To investigate the local structure of Mn_3Sn and $Ni_{0.25}Mn_{2.75}Sn$, we performed EXAFS

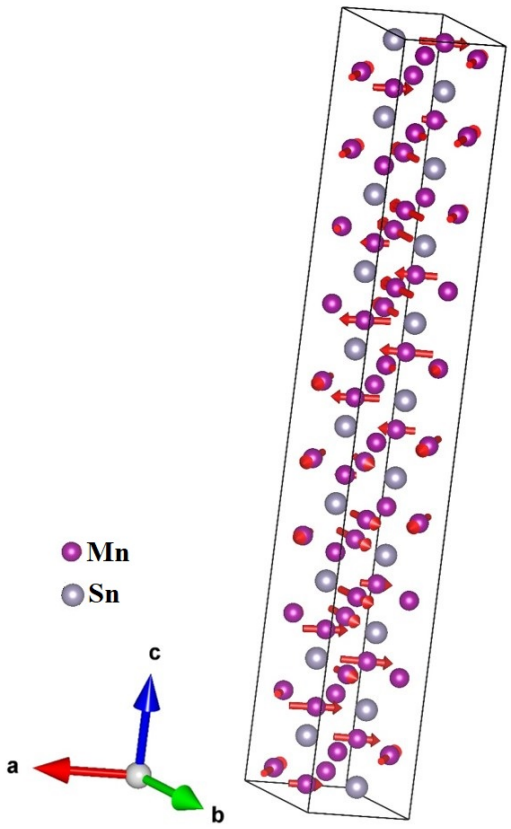

Figure 6.10: Refined magnetic superstructure of $Ni_{0.25}Mn_{2.75}Sn$ with ten unit cells at 220 K.

measurements at Mn and Ni K edges at 100 K and 300 K. The recorded Mn K and Ni K edges were fitted to the structural models based on their respective crystal structures in the k range of 3 $Å^{-1}$ to 14 $Å^{-1}$ and the R range of 1 Å to 3 Å. In a Kagome lattice plane of Mn_3Sn, two equilateral triangles are joined together by a single Mn atom. Thus, every Mn has four more Mn as the nearest neighbors in the xy-plane. Further, the neighboring Kagome xy-planes are stacked together along the c-axis. These xy-planes are arranged systematically with a lattice offset existing within the xy-plane. Such a lattice offset appears because of the presence of slight innate distortions in the Kagome lattice as a

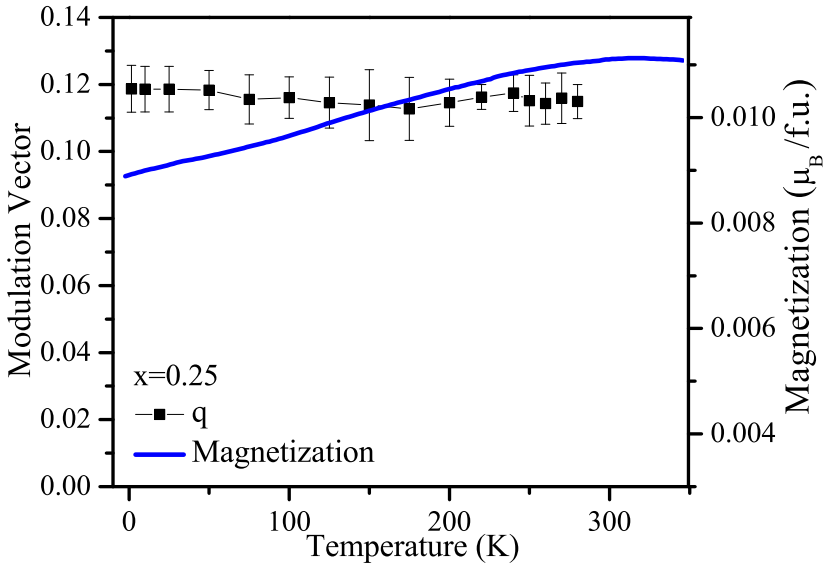

Figure 6.11: The thermal evolution magnetic modulation wave vector and the magnetization as a function of temperature for $Ni_{0.25}Mn_{2.75}Sn$.

consequence of the expansion of one triangle and shrinking of another, which are situated adjacent to each other.[1,42] These lattice distortions result from the breathing-type nature of these kagome lattices.

Fundamentally, in Mn_3X-type systems, an ideal Kagome lattice plane in its star-like shape has all six triangles of the same bond length ($d_1 = d_2 = 2.83$ Å) (see Fig. 6.12 (a)). Thus, an Mn atom is coordinated to four Mn atoms within the xy-plane at $d_1 = d_2$. Such Kagome lattice planes are stacked along the c-axis (see Fig. 6.12 (b)), resulting in 4 more Mn neighbours at 2.79 Å and 2 Sn neighbours respectively at 2.79 Å and 2.83 Å. As a result of the first-order transition at T_t, the Mn atoms in the Kagome plane slightly move from their position resulting in distortion of the neighbouring equilateral triangles ($d_1 \neq d_2$). This is also known as the breathing type Kagome lattice. As a result of this distortion, the local structure of Mn gets altered, and the 4 equal in plane Mn-Mn bonds

change to 2 long (d_1 = 2.92 Å) and 2 short (d_2 = 2.76 Å) distances.

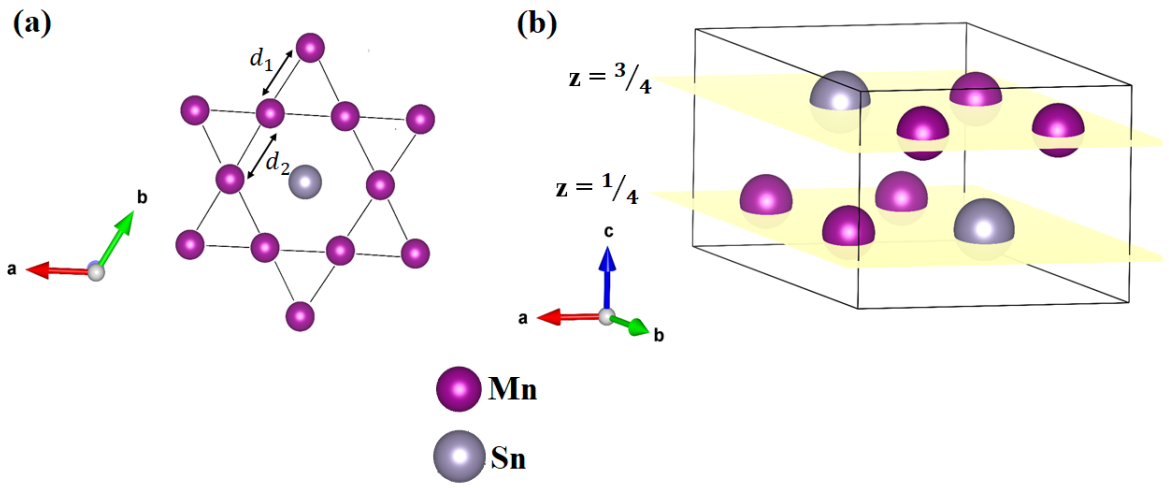

Figure 6.12: (a) Kagome lattice in xy plane. Here d_1 and d_2 denote the bond lengths of two neighboring triangles. (b) Unit cell of Mn_3Sn.

EXAFS at the Mn K edge in Mn_3Sn recorded at 300 K could be very well described by the ideal Kagome lattice model. The parameters obtained from this fitting are tabulated in Table 6.1 and the fitted curves for Mn EXAFS is displayed in Fig. 6.13 (c). A careful examination of bond distances reveals a shorter, out-of-plane, Mn-Mn bond distance (Mn-Mn $\parallel$ z = 2.64 Å instead of the expected 2.79 Å). This could be due to the presence of the Mn_2Sn impurity phase. At 100 K, which is below T_t, the ideal Kagome lattice model was incapable of providing a good fit with acceptable parameters and hence the distorted Kagome lattice model was employed. The fits obtained are presented in Fig. 6.13 (a) and the Mn-Mn and Mn-Sn bond distances are shown in Table 6.1. For $Ni_{0.25}Mn_{2.75}Sn$, the EXAFS data could only be described by the distorted Kagome lattice model at 100 K and 300 K as can be seen from the resultant fits in Fig. 6.13 (b) and (d) and the values of bond distances are available in Table 6.1.

The same model was also employed for the fitting of the Ni K edge of $Ni_{0.25}Mn_{2.75}S$ at 100 K, though the obtained fit was reasonably good (see Fig. 6.14), the obtained bond distances were different from the expected values deciphered from the crystal structure. In particular, a considerably shorter Ni-Sn bond distance was obtained pointing towards the existence of a local structural distortion around Ni.

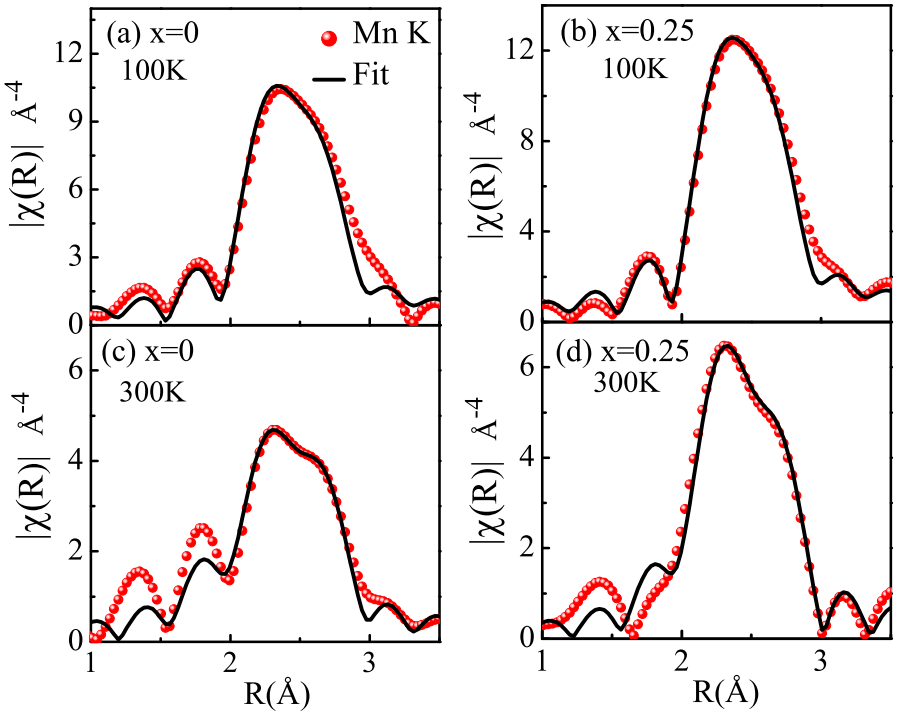

Figure 6.13: Best fit and k^3 weighted Fourier transform magnitude for the $\chi(k)$ spectra obtained at Mn K edge for Mn_3Sn and $Ni_{0.25}Mn_{2.75}Sn$.

In Chapter 4 of this thesis, we have shown that Mn_2NiSn-type alloys tend to decompose into Ni_2MnSn-type Heusler phase and $D0_{19}$ Mn_3Sn-type hexagonal phase upon temper annealing.[43] The shorter Ni-Sn bond distance obtained in $Ni_{0.25}Mn_{2.75}Sn$ could be a result of the segregation of Heulser-type structural defect. In an $L2_1$ Heusler phase of Ni-Mn-Sn,

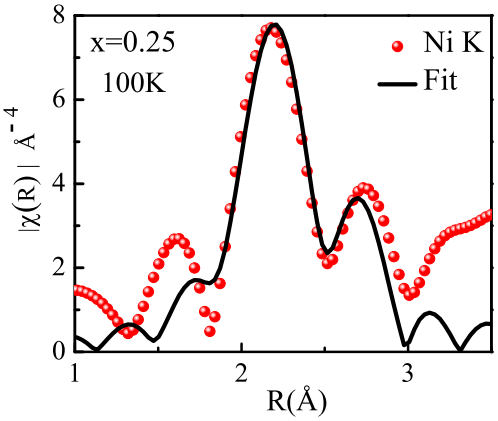

Figure 6.14: Best fit and k^3 weighted Fourier transform magnitude for the $\chi(k)$ spectra obtained at Ni K edge for $Ni_{0.25}Mn_{2.75}Sn$.

Table 6.1: Bond length (R) and mean square distortion in bond lengths (σ^2) obtained from Mn edge EXAFS fitting of $Mn_{3-x}Ni_xSn$ x = 0 and 0.25 alloys, recorded at 100 K and 300 K. Figures specified in the parenthesis denote the uncertainty in the ending digit. Here C.N. refers to the coordination number.

Mn_3Sn				$Ni_{0.25}Mn_{2.75}Sn$			
Bond	C.N	R (Å)	σ^2 (Å^2)	Bond	C.N	R (Å)	σ^2 (Å^2)
T=300 K							
Mn-Mn ∥ z	4	2.646(22)	0.011(5)	Mn-Mn ∥ z	4	2.678(15)	0.010(2)
Mn-Mn ⊥ z	4	2.812(21)	0.007(4)	Mn-Mn ⊥ z	2	2.928(7)	0.004(2)
Mn-Sn	2	2.784(13)	0.007(2)	Mn-Mn ⊥ z	2	2.755(7)	0.004(2)
Mn-Sn	2	2.827(13)	0.007(2)	Mn-Sn	4	2.835(7)	0.009(1)
T=100 K							
Mn-Mn ∥ z	4	2.696 (16)	0.008(1)	Mn-Mn ∥ z	4	2.688(13)	0.006(1)
Mn-Mn ⊥ z	2	2.925(8)	0.005(1)	Mn-Mn ⊥ z	2	2.931(7)	0.0006(10)
Mn-Mn ⊥ z	2	2.758(8)	0.001(1)	Mn-Mn ⊥ z	2	2.753(7)	0.0006(10)
Mn-Sn	4	2.834(10)	0.001(1)	Mn-Sn	4	2.834(10)	0.005(1)

the nearest Ni-Sn distance is about 2.6 Å.

To explore this possibility of the existence of Heusler-like local environments in $Ni_{0.25}Mn_{2.75}Sn$, we prepared $Ni_{0.5}Mn_{2.5}Sn$ and characterized it for structural and magnetic properties. The chemical composition of $Ni_{0.5}Mn_{2.5}Sn$ was found to be $Ni_{0.47}Mn_{2.52}Sn_{1.01}$. The recorded XRD pattern and the measured M(T), M(H) curves for this alloy are dis-

Table 6.2: Bond length (R) and mean square distortion in bond lengths (σ^2) obtained from Ni edge EXAFS fitting of $Ni_{0.25}Mn_{2.75}Sn$ alloy, recorded at 100 K. Figures specified in the square brackets denote the uncertainty in the ending digit.

$Ni_{0.25}Mn_{2.75}Sn$			
T=100 K			
Bond	C.N	R(Å)	σ^2 (Å^2)
Ni-Mn ∥ z	4	2.665(17)	0.006(2)
Ni-Mn ⊥ z	2	2.908(57)	0.006(4)
Ni-Mn ⊥ z	2	2.779(43)	0.006(5)
Ni-Sn	4	2.740(25)	0.013(5)

played in Fig. 6.15.

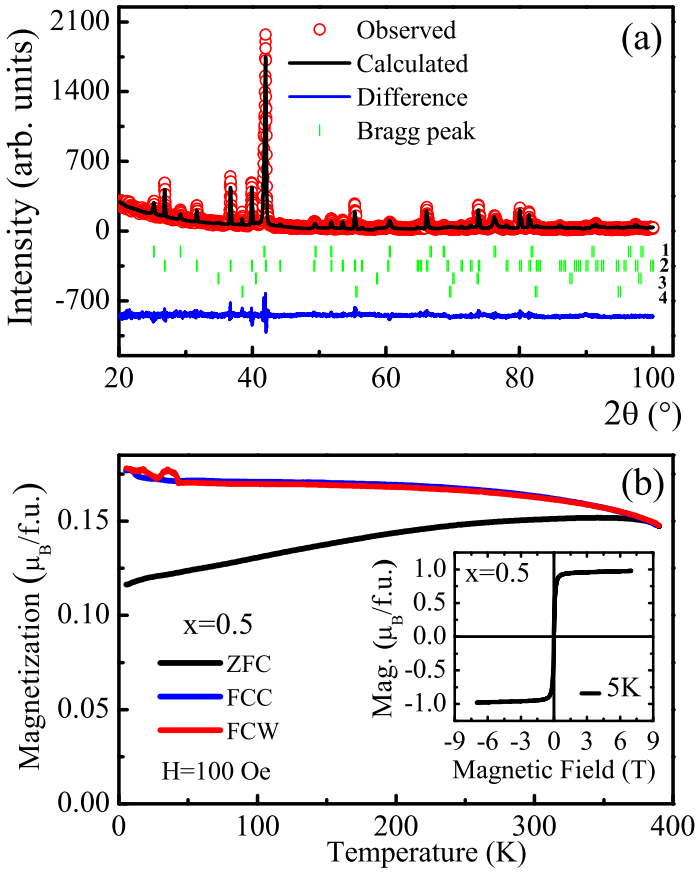

Figure 6.15: (a) The powder x-ray diffraction pattern recorded for $Ni_{0.5}Mn_{2.5}Sn$ at room temperature. Structural phases recognized from Rietveld refinement analysis are specified by numerals, 1 - $L2_1$ Heusler, 2 - $D0_{19}$ Hexagonal, 3 - Sn, and 4 - MnO. (b) Temperature-dependent magnetization measurement for $Ni_{0.5}Mn_{2.5}Sn$. Inset shows the field-dependent isothermal magnetization measurement at 5 K.

The Rietveld refinement of the x-ray diffraction pattern for $Ni_{0.5}Mn_{2.5}Sn$ showed the presence of two distinct major phases identified as $L2_1$ and $D0_{19}$ in addition to the Sn and MnO impurities. The magnetization curves measured in a field of 100 Oe also revealed a ferromagnetic alloy with an ordering temperature $T_C > 390$ K. Though the magnetic moment per formula unit is low compared to Ni_2MnSn, it is about an order of magnitude higher than that in Mn_3Sn. This ferromagnetic signal is due to the presence of $L2_1$ Heusler phase. This observation lends weight to the formation of Heusler-like defects, especially around Ni in $Ni_{0.25}Mn_{2.75}Sn$.

6.3 Discussion

The present study has perceived a significant impact of Ni substitution on structural (local), magnetic, transport, and magneto-transport properties of Mn_3Sn. Predominantly, this substitution has observed the modifications such as the vanishing of T_t transition over the range from 390 K to 1.5 K, a surge in the magnetic moment, semiconductor-like resistivity as a function of temperature, continuous Hall resistivity signal as a function temperature in the range from 390 K to 1.5 K, and a complete switching of magnetic ground state structure to non-coplanar helical at all temperatures from 280 K to 3 K.

Essentially, Mn_3Sn is an itinerant Kagome antiferromagnet. Here the Mn atoms get organized in a star-like shape that anticipates the lattice frustration. At room temperature, as a result of these frustrations, the Mn moments residing on these Kagome lattices get arranged into a non-collinear, 120° triangular spin structure. In our course of the

investigation, we have successfully been able to reproduce the reported structural, magnetic, transport, and magneto-transport properties in our prepared Mn_3Sn. It is observed to undergo a spin reorientation transition from the co-planar inverse-triangular spin order to the non-coplanar helical spin order at $T_t \sim 290$ K. Generally, above its T_t, the insignificant Kagome lattice deformations and the off-stoichiometric elemental composition, leads to the emergence of weak ferromagnetism in the system.[22,26] However, below T_t, this weak ferromagnetism vanishes completely due to the disintegration of its residual moment.[2]

An antiferromagnet with zero magnetization should not show an anomalous Hall effect, usually shown by the ferromagnets and known to escalate with their magnetization. However, the antiferromagnetic Mn_3Sn exhibits the aforementioned effect, which is found to emerge as a consequence of its chiral spin structure, which breaks the time-reversal symmetry and leads to the unfolding of Berry curvature in k-space.[7,10,27,44,45] These observations have realized the anomalous Hall signal to be very sensitive to the subtle alignment of its magnetic spins. The vanishing of this signal below T_t temperature points towards the fact that the magnetic spin structure has successfully averaged out its Hall signal to insignificant but finite value.[9]

The ND data refinement analysis for our Mn_3Sn is in alignment with the reported, wherein, above T_t, the magnetic structure is found to be co-planar inverse triangular antiferromagnetic with k = (0, 0, 0) wave vector.[1] Whereas, below T_t, it is found to be non-coplanar helical, modulating along the z-axis.[31,46] In Mn_3Sn, the magnetic ordering

wave vector k = (0, 0, 0) is known to break an essential magnetic symmetry that enables the appearance of the significant anomalous Hall signal above T_t.[29,47] Below T_t, when the magnetic structure transforms to a non-coplanar helical and the symmetry that is broken already above T_t, now gets satisfied below T_t. So the presence of this magnetic structure makes the anomalous Hall effect due to Berry phase curvature vanish. The reported Monte Carlo simulations and the ab initio calculations for Mn_3Sn do not observe Weyl nodes in the electronic band structures of its modulated magnetic spin structure.[11] Besides, these events have also been noticed experimentally, where the helical antiferromagnetic state is found to preserve the symmetry that leads to the disappearance of k-space Berry curvature below T_t.[30]

The substitution of Ni in Mn_3Sn leads to the disappearance of the spin-reorientation T_t transition and an appreciable increase in its magnetic moment. The ND analysis for $Ni_{0.25}Mn_{2.75}Sn$ established its magnetic structure to be non-coplanar helical at all temperatures from 280 K to 3 K. Based on these observations; the anomalous Hall signal was not expected in $Ni_{0.25}Mn_{2.75}Sn$. Interestingly, the alloy displays the anomalous Hall effect. Strengthened ferromagnetism in $Ni_{0.25}Mn_{2.75}Sn$ could be held responsible for the non-zero Hall resistivity in this alloy. However, previous studies on chiral antiferromagnets like Mn_3Ge and Mn_3Sn have observed that the weak ferromagnetism does not contribute towards its anomalous Hall effect and only governs the chirality of their magnetic spin structure.[2,48] Hence, the observed Hall resistivity in $Ni_{0.25}Mn_{2.75}Sn$ appears to come from the Berry phase curvature in k-space.

The substitution of Ni in place of Mn is speculated to affect the spacing between the Weyl nodes, which can explain the semiconductor-like resistivity exhibited by $Ni_{0.25}Mn_{2.75}Sn$. Fig. 6.16 illustrates the normalized resistance that shows a -ln(T) rise from room temperature to the temperature of $T_K \sim 232$ K, followed by a rise with moderate rate and finally at low temperatures extend to a value of almost saturation. Here, the measured conductance represented by $G_{measured}$ is categorised into two sections as $G_{plateau}$ and $G_{insulator}$, where the $G_{insulator}$ is given by $G_{insulator} = G_a \exp \frac{-\Delta}{k_B T}$.[49,50] Here, Δ refers to a gap between the Weyl cones. Inset of Fig. 6.16 gives a plot of $G_{measured}$ - $G_{plateau}$ against 1/T in the range from 300 K to 232 K. The gap estimated from this plot is $\sim$ 2.01 meV.

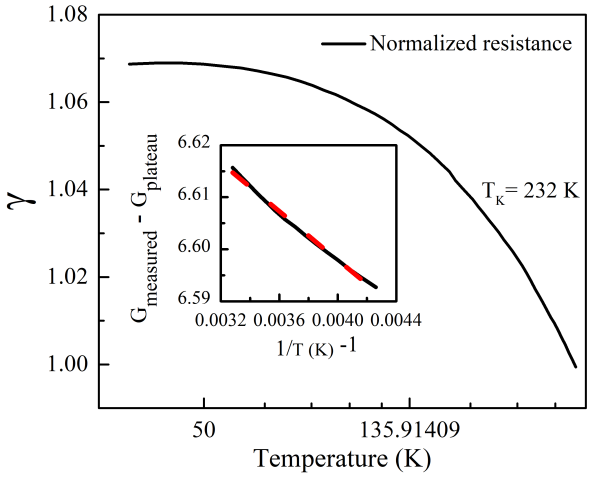

Figure 6.16: Temperature dependent normalized resistance 'γ'. Inset shows the plot of $G_{measured}$ - $G_{plateau}$ as a function of 1/T with a linear fit shown by the red dotted line.

Thus, it appears that the Fermi surface of Mn_3Sn with gapless Weyl cones gets converted to a gapped one upon Ni substitution. The main reason for this change is the local

structural distortion observed around Ni atoms. This structural distortion disturbs the Kagome lattice arrangement resulting in the tilting of the spins towards the easy local axis while forming the helix structure.

6.4 Conclusions

In conclusion, the substitution of Ni in Mn_3Sn significantly impacts the structural, magnetic, transport, and magneto-transport properties of Mn_3Sn. Firstly, the magnetic ground state in the Ni-doped alloy is non-coplanar helical at all temperatures studied here. Further, despite the helical magnetic order and relatively stronger ferromagnetism compared to Mn_3Sn, the Hall resistivity signal does not diminish. This can be attributed to the changes in the Berry phase curvature in the k-space resulting in the formation of gapped Weyl nodes at the Fermi surface. The changes in the Berry phase curvature occur due to structural distortions around the Ni atoms that disturb the Kagome lattice structure resulting in tilting of spins along the easy axis.

References

[1] S. Nakatsuji, N. Kiyohara, and T. Higo. *Nature*, 527(7577):212–215, 2015.

[2] J. Yan, X. Luo, H. Y. Lv, Y. Sun, P. Tong, W. J. Lu, X. B. Zhu, W. H. Song, and Y. P. Sun. *Applied Physics Letters*, 115(10):102404, 2019.

[3] A. A. Zyuzin and A. A. Burkov. *Physical Review B*, 86(8):115133, 2012.

[4] Kai-Yu Yang, Yuan-Ming Lu, and Ying Ran. *Physical Review B*, 84(11):075129, 2011.

[5] Y. Taguchi, Y. Oohara, H. Yoshizawa, N. Nagaosa, and Y. Tokura. *Science*, 291(5513):2573–2576, 2001.

[6] Y. Machida, S. Nakatsuji, S. Onoda, T. Tayama, and T. Sakakibara. *Nature*, 463(7278):210–213, 2010.

[7] H. Chen, Q. Niu, and A. H. MacDonald. *Physical Review Letters*, 112(5):017205, 2014.

[8] J. Kubler and C. Felser. *Europhysics Letters*, 120(4):47002, 2018.

[9] N. H. Sung, F. Ronning, J. D. Thompson, and E. D. Bauer. *Applied Physics Letters*, 112(13):132406, 2018.

[10] Hao Yang, Yan Sun, Yang Zhang, Wu-Jun Shi, Stuart S P Parkin, and Binghai Yan. *New Journal of Physics*, 19(1):015008, 2017.

[11] P. Park, J. Oh, K. Uhlířová, J. Jackson, A. Deák, L. Szunyogh, K. H. Lee, H. Cho, H. L. Kim, Helen C. Walker, et al. *npj Quantum Materials*, 3(1):63, 2018.

[12] C. Singh, V. Singh, G. Pradhan, V. Srihari, H. K. Poswal, R. Nath, A. K Nandy, and A. K. Nayak. *Physical Review Research*, 2(4):043366, 2020.

[13] C. Singh, S. k. Jamaluddin, A. K. Nandy, M. Tokunaga, M. Avdeev, and A. K. Nayak. *arXiv preprint arXiv:2211.12722*, 2022.

[14] Z. H. Liu, Q. Q. Zhang, Y. J. Zhang, H. G. Zhang, X. Q. Ma, and E. K. Liu. *Journal of Physics: Condensed Matter*, 33(11):115803, 2020.

[15] H. Tsai, T. Higo, K. Kondou, T. Nomoto, A. Sakai, A. Kobayashi, T. Nakano, K. Yakushiji, R. Arita, S. Miwa, et al. *Nature*, 580(7805):608–613, 2020.

[16] S. Tomiyoshi and Y. Yamaguchi. *Journal of the Physical Society of Japan*, 51(8):2478–2486, 1982.

[17] J. Liu and L. Balents. *Physical Review Letters*, 119(8):087202, 2017.

[18] L. M. Sandratskii and J. Kübler. *Physical Review Letters*, 76(0):4963–4966, 1996.

[19] G. Lingannan, A. Singh, B. Joseph, S. Singh, and S. Arumugam. *Physica Status Solidi (RRL) - Rapid Research Letters*, 15(4):2000605, 2021.

[20] J. J. Deng, M. Y. Zhao, Y. Wang, X. Wu, X. T. Niu, L. Ma, D. W. Zhao, C. M. Zhen, and D. L. Hou. *Journal of Physics D: Applied Physics*, 55(27):275001, 2022.

[21] A. Low, S. Ghosh, S. Changdar, S. Routh, S. Purwar, and S. Thirupathaiah. *Physical Review B*, 106(10):144429, 2022.

[22] S. Nakatsuji, T. Higo, M. Ikhlas, T. Tomita, and Z. Tian. *Philosophical Magazine*, 97(30):2815–2827, 2017.

[23] G. J. Zimmer and E. Krén. *AIP Conference Proceedings*, 10(1):1379–1383, 1973.

[24] E. Krén, J. Paitz, G. Zimmer, and É. Zsoldos. *Physica B+ C*, 80(1-4):226–230, 1975.

[25] Muhammad Ikhlas, Takahiro Tomita, Takashi Koretsune, Michi-To Suzuki, Daisuke Nishio-Hamane, Ryotaro Arita, Yoshichika Otani, and Satoru Nakatsuji. *Nature Physics*, 13(11):1085–1090, 2017.

[26] T. Nagamiya, S. Tomiyoshi, and Y. Yamaguchi. *Solid State Communications*, 42(5):385–388, 1982.

[27] Delin Zhang, Binghai Yan, Shu-Chun Wu, Jurgen Kubler, Guido Kreiner, Stuart S. P. Parkin, and Claudia Felser. *Journal of Physics: Condensed Matter*, 25(20):206006, 2013.

[28] A. Markou, J. M. Taylor, A. Kalache, P. Werner, S. S. P. Parkin, and C. Felser. *Physical Review Materials*, 2(5):051001, 2018.

[29] X. Wang. *Single crystal growth and neutron scattering studies of novel quantum materials*. 2021.

[30] P. K. Rout, P. V. P. Madduri, S. K. Manna, and A. K. Nayak. *Physical Review B*, 99(7):094430, 2019.

[31] P. J. Brown, V. Nunez, F. Tasset, J. B. Forsyth, and P. Radhakrishna. *Journal of Physics:Condensed Matter*, 2(47):9409, 1990.

[32] T. F. Duan, W. J. Ren, W. L. Liu, S. J. Li, W. Liu, and Z. D. Zhang. *Applied Physics Letters*, 107(8):082403, 2015.

[33] S. Tomiyoshi, S. Abe, Y. Yamaguchi, H. Yamauchi, and H. Yamamoto. *Journal of Magnetism and Magnetic Materials*, 54-57:1001–1002, 1986.

[34] W. J. Feng, D. Li, W. J. Ren, Y. B. Li, W. F. Li, J. Li, Y. Q. Zhang, and Z. D. Zhang. *Physical Review B*, 73(5):205105, 2006.

[35] J. Sticht, K. H. Höck, and J. Kubler. *Journal of Physics: Condensed Matter*, 1(43):8155, 1989.

[36] P. M. Vora, P. Gopu, M. Rosario-Canales, C. R. Pérez, Y. Gogotsi, J. J. Santiago-Avilés, and J. M. Kikkawa. *Physical Review B*, 84(15):155114, 2011.

[37] T. Ghosh, S. Agarwal, and P. K. Mukhopadhyay. *Journal of Magnetism and Magnetic Materials*, 418:260–264, 2016.

[38] I. Gavrikov, M. Seredina, M. Zheleznyy, I. Shchetinin, D. Karpenkov, A. Bogach, R. Chatterjee, and V. Khovaylo. *Journal of Magnetism and Magnetic Materials*, 478:55–58, 2019.

[39] N. E. Hussey, K. Takenaka, and H. Takagi. *Philosophical Magazine*, 84(27):2847–2864, 2004.

[40] J. R. Soh, F. de Juan, N. Qureshi, H. Jacobsen, H. Y. Wang, Y. F. Guo, and A. T. Boothroyd. *Physical Review B*, 101(14):140411, 2020.

[41] Y. Chen, J. Gaudet, S. Dasgupta, G. G. Marcus, J. Lin, T. Chen, T. Tomita, M. Ikhlas, Y. Zhao, W. C. Chen, et al. *Physical Review B*, 102(5):054403, 2020.

[42] Hung-Hsiang Yang, Chi-Cheng Lee, Yasuo Yoshida, Muhammad Ikhlas, Takahiro Tomita, Agustinus Nugroho, Taisuke Ozaki, Satoru Nakatsuji, and Yukio Hasegawa. *Scientific Reports*, 9(1):1–7, 2019.

[43] S. V. Malik, E. T. Dias, A. K. Nigam, and K. R. Priolkar. *Journal of Physics D: Applied Physics*, 55(16):165002, 2022.

[44] N. Nagaosa, J. Sinova, S. Onoda, A. H. MacDonald, and N. P. Ong. *Reviews of Modern Physics*, 82(0):1539–1592, 2010.

[45] A. K. Nayak, J. E. Fischer, Y. Sun, B. Yan, J. Karel, A. C. Komarek, C. Shekhar, N. Kumar, W. Schnelle, J. Kubler, C. Felser, and S. S. P. Parkin. *Science Advances*, 2(4):e1501870, 2016.

[46] J. W. Cable, N. Wakabayashi, and P. Radhakrishna. *Solid State Communications*, 88(2):161–166, 1993.

[47] K. Kuroda, T. Tomita, M. T. Suzuki, C. Bareille, A. A. Nugroho, P. Goswami, M. Ochi, M. Ikhlas, M. Nakayama, S. Akebi, et al. *Nature Materials*, 16(11):1090–1095, 2017.

[48] A. K. Nayak, J. E. Fischer, Y. Sun, B. Yan, J. Karel, A. C. Komarek, C. Shekhar, N. Kumar, W. Schnelle, J. Kübler, et al. *Science Advances*, 2(4):e1501870, 2016.

[49] D. Khadka, T. R. Thapaliya, S. Hurtado Parra, X. Han, J. Wen, R. F. Need, P. Khanal, W. Wang, J. Zang, J. M. Kikkawa, et al. *Science Advances*, 6(35):eabc1977, 2020.

[50] S. Wolgast, Ç. Kurdak, K. Sun, J. W. Allen, D. J. Kim, and Z. Fisk. *Physical Review B*, 88(18):180405, 2013.

Chapter 7

Summary and Future Work

7.1 Summary

The main aim of this thesis is to understand the effect of antisite disorder and structural distortions on the structural (crystal, local, and magnetic), magnetic, transport, and magneto-transport properties of Mn-rich Heusler alloys. To accomplish these objectives we prepared a series of $Ni_{2-x}Mn_{1+x}Ga$ and $Ni_{2-x}Mn_{1+x}Sn$ with ($0 \leq x \leq 2$) alloys by arc melting technique. Different heat treatments were chosen to understand the structural stability, site occupancy, and their effect on the properties of these alloys.

Firstly, we attempted to understand higher T_M in Mn_2NiGa despite its lower e/a ratio than Ni_2MnGa. EXAFS studies at the Ni, Mn, and Ga K edges in $Ni_{2-x}Mn_{1+x}Ga$ with (x = 0, 0.25, 0.5, 0.75, and 1.0) indicated the existence of longer Mn-Ga and Mn-Mn bond distances in Mn-rich alloys, which compared well with the bond distances in the various structural phases of Mn_3Ga. The existence of these phases as impurities in $Ni_{2-x}Mn_{1+x}Ga$ ($x = 0.75$ and 1.0) was then confirmed by refining the synchrotron x-ray diffraction data. Such segregation of Mn_3Ga-type impurity phases was shown to occur due to an antisite disorder between the Y and Z sub-lattices of the X_2YZ Heusler structure. Thus, the phase

separation of Mn_2NiGa into Ni-rich Heulser phase and impurity Mn_3Ga type phase results in higher martensitic transformation temperature.

Further, the structural stability of isostructural Mn_2NiSn was also tested. Like Mn_2NiGa, Mn_2NiSn also crystallizes into the $L2_1$ structure but does not display a martensitic transformation, though predicted theoretically. A discrepancy also exists in the experimentally measured and theoretically calculated magnetic moments. A wide variation from 0.7 μ_B/f.u. to 3.25 μ_B/f.u. is noted in the theoretically calculated values against 2.95 μ_B/f.u., measured experimentally. To understand the structural interactions responsible for such magnetic properties, a series of $Ni_{2-x}Mn_{1+x}Sn$ with (x = 0, 0.25, 0.5, 0.75, and 1.0) alloys were studied. Further, some alloy compositions (x = 0.75 and 1.0) were subjected to additional temper annealing (TA) to test their structural stability. The temper-annealed alloys exhibited structural phase separation into a major $L2_1$ phase and a minor $D0_{19}$ hexagonal phase rendering the Mn-rich alloys metastable. Structural defects were also noted in the local structural environments of Mn and Sn in the quenched $Ni_{2-x}Mn_{1+x}Sn$ with (x = 0.75, and 1.0) alloys. These defects are facilitated by an antisite disorder between the Mn and Sn atoms occupying the Y and Z sub-lattices of X_2YZ structure. The presence of structural defects explains the observed magnetic and transport properties of these alloys.

Increasing Mn concentration in $NiMn_2Ga$/Mn_2NiGa gives rise to multiphase alloys until $Ni_{0.25}Mn_{2.75}Ga$ at which a structural transformation occurs to disordered face-centred cubic (Cu_3Au-type) structure. The multiphase nature of these compositions is an exten-

sion of impurity phase segregation observed in Mn_2NiGa. We investigated the structural and magnetic properties of two compositions, $Mn_{3-y}Ni_yGa$ with ($y = 0$ and 0.25) alloys. Mn_3Ga in its cubic phase is antiferromagnetic, that transforms to a ferrimagnetic $D0_{22}$-type tetragonal phase when annealed at a lower temperature of 400°C. On the other hand, $Ni_{0.25}Mn_{2.75}Ga$ in its cubic phase exhibits weak ferromagnetism. The EXAFS study on $Ni_{0.25}Mn_{2.75}Ga$ spotted structural distortions in the local environment of its constituent atoms which are identified to be mainly because of the locally formed Ni-rich $L2_1$ Heusler defects within the Mn_3Ga-type lattice. Further, the first order like magnetic transition observed at T $\sim$ 200 K and the weak ferromagnetism seen in cubic $Ni_{0.25}Mn_{2.75}Ga$ affirms the formation of ferromagnetic Ni_2MnGa-type defects in the antiferromagnetic lattice of Mn_3Ga. Low-temperature annealing confirms the formation Ni-Mn-Ga Heusler-like entities in $Ni_{0.25}Mn_{2.75}Ga$. The ferromagnetic defect phase and the antiferromagnetic major phase interact with each other leading to the observation of the kinetic arrest and the exchange bias.

A similar increase in Mn concentration in $Ni_{2-x}Mn_{1+x}Sn$ results in biphasic alloys for $1 < x < 1.75$. The two compositions $Ni_{0.25}Mn_{2.75}Sn$ and Mn_3Sn crystallize into the $D0_{19}$ structure. These were explored for their structural (crystal and local), magnetic, transport, and magneto-transport properties. Mn_3Sn is a well-known itinerant Kagome antiferromagnet with a $T_N \sim 420$ K. At room temperature, it displays non-collinear antiferromagnetic ordering with 120° inverse-triangular spin structure. The triangular coplanar magnetic order undergoes a spin reorientation and transforms into a helical non-

coplanar magnetic structure with a finite net magnetization along the c-axis at a transition temperature $T_t \sim 290$ K. Above T_t, the 120° inverse-triangular antiferromagnetic spin structure of Mn_3Sn results in a large anomalous Hall effect. However, below T_t, the large anomalous Hall signal vanishes. The substitution of Ni in Mn_3Sn remarkably impacts its properties. Firstly, the magnetic ground state in the Ni-doped alloy transforms to non-coplanar helical at all temperatures studied here. Further, despite the helical magnetic order and relatively stronger ferromagnetism compared to Mn_3Sn, the Hall resistivity signal does not diminish. This can be attributed to the changes in the Berry phase curvature in the k-space resulting in the formation of gapped Weyl nodes at the Fermi surface. The changes in the Berry phase curvature occur due to structural distortions around the Ni atoms that disturb the Kagome lattice structure resulting in tilting of spins along the easy axis.

7.2 Future work

• During the course of the research, the phenomenon of phase separation has been observed in the proposed concentration lines Ni-Mn-Ga/Sn, especially in Mn-rich Mn_2NiGa and Mn_2NiSn alloys, thus questioning their phase stability. Observing the phenomenon of phase separation in such Mn-rich alloys has opened up a new prospect to observe the same in known and novel Mn_2YZ systems.

• To investigate the implication of antisite disorder in martensitic transformation in already known and newer systems.

• To study the exact path from the formation of local structural defect to the segregation into an impurity phase, for instance, from $L2_1$ to $D0_{19}/D0_{22}$ structure is yet to be explored.

List of Publications:

1. S. V. Malik, E. T. Dias, A. K. Nigam, and K. R. Priolkar, J. Phys. D Appl. Phys. 55, 165002, (2022).

2. S. V. Malik and E. T. Dias and V. Srihari and P. D. Babu and K. R. Priolkar, Intermetallics 148,107613 (2022).

3. Ni induced ferromagnetism in Mn_3Ga.: S. V. Malik, E. T. Dias, and K. R. Priolkar (In progress).

4. Exploring the structural, magnetic, and electronic properties in $Ni_{2-x}Mn_{1+x}Sn$ (x= 2 and 1.75).: S. V. Malik, E. T. Dias, A. Das and K. R. Priolkar (In progress).

Conference Presentations and Participation:

1. Participated in 'Indo - Italian three-day workshop on Elettra synchrotron' at IISc-Bangalore, 2018.

2. Presented a poster at the 'Indo - Portuguese two-day workshop on Material Science' at Goa University, 2019.

3. Presented a poster on 'Novel magnetic ground states in Ni-doped Mn_3Sn' in the symposium on 'Recent Trends in Condensed Matter Physics and Material Science', held from 12^{th} – 13^{th} March 2020, at Goa University.

4. Presented poster on 'Antisite disorder and defect phase segregation and its role in magnetic properties of Mn_2NiSn' at IEEE International Magnetics Virtual Conference, 'INTERMAG 21' held from 26^{th} - 30^{th} April 2021.

5. Presented Oral and Poster on 'Ni induces ferromagnetism in Mn_3Ga' in the 65^{th} DAE Solid state Physics Symposium, organized by BARC, BRNS, and DAE held at Bhabha Atomic Research Centre, Mumbai, during 15^{th} - 19^{th} December 2021.

6. Presented poster in the International Conference on Advanced Materials: Properties and Applications, at Goa University, Goa, India during 20^{th} - 24^{th} February 2023.